Studies on the sensitivity of multi-PMT optical modules to supernova neutrinos in the South Pole ice

Master Thesis

presented at
Westfälische Wilhelms-Universität Münster, Institut für Kernphysik

in partial fulfilment of the requirements for the degree of

Master of Science, Westfälische Wilhelms-Universität Münster
Máster Interuniversitario en Física Nuclear, Universidad de Sevilla

By: **Cristian Jesús Lozano Mariscal**

Supervisor and first examiner: Prof. Dr. Alexander Kappes
Westfälische Wilhelms-Universität Münster
Second examiner: Prof. Dr. José Manuel Quesada Molina
Universidad de Sevilla

Münster, January 2017

Contents

1 Preface

Neutrinos are one of the fundamental particles which make up the universe and they are also one of the least understood. The study of neutrinos is one of the most exciting fields for physicist in the last decades. It was in 1930 when the neutrino was for the first time postulated by Wolfgang Pauli. In those days it was thought that neutrinos were massless and that experiments would never be able to detect them. *"I have done a terrible thing; I have postulated a particle that can not be detected"* is a famous quote of W. Pauli about the neutrino. More than 80 years later, physicist have learned a lot from this amazing particle, and its detection has already been achieved. Nevertheless, there are still many questions about the neutrino nature and their interactions, which makes neutrino physics a booming field.

Neutrinos are produced in different kind of events, covering from nuclear decays in e.g. nuclear reactors to atmospheric reactions, supernova (SN) burst neutrinos, SN relic neutrinos and more [1]. While most neutrino experiments have been designed to study its properties and the physics beyond the standard model, it has turned out that neutrinos are great messengers of galactic events. This fact is currently opening a new window in universe exploration. The role of neutrinos is specially important in the astonishing core-collapse supernova explosions, where most of the energy (around 99%!) of the explosion is carried out by neutrinos [2]. So far, the only detection of SN burst neutrinos have been made in 1987 from the famous SN 1987A [1, 3, 4]. This SN was clearly visible from The Earth, but approximately two to three hours before its visible light reached Earth, a burst of neutrinos was observed at three separate neutrino observatories.

There are several neutrino observatories around the world, with different sizes and characteristics. The energy spectra of cosmic neutrinos is very broad, where there are neutrinos with very low energy, whose signals in the detectors can be easily confused with background signals, as well as neutrinos with huge energies [5]. The study of neutrinos have revealed important results, like their non-zero mass; which has important repercussions in the standard model, or the neutrino oscillations; which solved the problem of the solar neutrino deficit [6]. The study of the neutrinos coming from core-collapse supernova can help to the understanding of the SN formation and explosion, since they come from the very inner core of the star. Understanding neutrinos could also shed light on major unanswered astrophysical questions, like the cause for the matter-antimatter asymmetry in the universe, which could help to understand the origin of the universe.

Among these neutrino observatories is *IceCube*. IceCube uses one cubic kilometer of South Pole ice as its sensitive volume, where several arrays of digital optical modules (usually refered as *DOMs*) are deployed looking for the results of neutrino interactions [7]. IceCube has already gotten interesting results, like the observation of a 2000 TeV event; the highest-energy neutrino interaction ever observed [8]. Right now, an upgrade of this observatory, *IceCube-Gen2*, is under development [9]. IceCube-Gen2 will take advantage of the advances in technology to build a bigger and more efficient detector with ~ 8 cubic kilometers of instrumented volume [10]. As the "eyes" of the detector, the DOMs play one of the most important roles in the operation of the detector, therefore

it is not surprising that new optical modules are being studied in order to install them in IceCube-Gen2. At the moment, several concepts are being developed, among them is the multi-PMT digital optical module (*mDOM*) [11]. The mDOM is designed with the motivation of several improvements over the old DOM with the caution of maintaining a similar price per module. The mDOM consists in a module with 24 small photomultipliers (*PMTs*), instead of one big photomultiplier as the current DOMs have, with the goals of having near uniform acceptance, increased photosensitive area, obtain better direction reconstruction and be able to suppress background rates by coincidences between different photomultipliers in the same module.

What determines the neutrino energy range in which IceCube is optimized are the distances between modules and its total covered volume. On the one hand, it is important to detect a neutrino in more than one module to be able to distinguish it from other particle sources. The smaller the neutrino energy is, the shorter is the path of its interaction in ice, and the other way around: a high energetic neutrino produces particles which propagate its interaction through large distances. For instance, a 10 PeV muon generated by a neutrino interaction would travel about 21 km before its energy drops to 10% of its initial energy, which makes the active volume for muon neutrino detection significantly larger than the instrumented volume in IceCube. The desired bigger volume for IceCube-Gen2 is planned with the goal of detecting these high energetic neutrinos, which reach Earth in a very low flux and therefore huge sensitive volumes are necessary to detect them at a considerable rate [9, 10].

Neutrinos from core-collapse supernova bursts have energies of about tens of MeVs. The resulting particles of SN neutrino interactions in ice are mainly electrons and positrons, which would travel about $\sim 10\,\text{cm}$ before they have lost their energy and stopped [12]. Because of this short path, the detection of these particles in more than one module is very unlike. At the moment, the way IceCube expects to detect a SN burst is by observing a collective rise in the rates of all photomultipliers on top of the dark noise. The implementation of mDOMs in IceCube-Gen2 can open a new vision for these low energetic events. Because of the 24 photomultipliers per module, it is much more probable that low energetic events are detected in more than one photomultiplier. The identification of individual events by coincidences can enable the detection of not only nearby supernovae but also to neutrinos coming from extra-galactic supernovae. Motivated by the potential of the mDOM for the detection of low energetic events, this work will study its sensitivity for the detection of MeV neutrinos coming from core-collapse supernovae.

2 Neutrinos from core-collapse supernovae

The development of core-collapse supernova explosions is not totally well understood yet, nevertheless, it is believed that neutrinos play a main role in these events. SN neutrinos are produced in the inner core of these stars, therefore their detection and study can reveal a detailed picture of the events that accompany the collapse of the core [13]. In this chapter, the core-collapse mechanism is studied, together with a model of its neutrino fluxes and the main SN neutrino interactions in ice.

2.1 Core-collapse supernova explosions

In this section, the mechanism of a type II SN explosion will be described. The SNe were first historically classified depending on the absorption lines of their spectra, where type I SNe do not show lines of hydrogen while type II SN do. The mechanism of a type I SNe, which are believed to be due the thermonuclear disruption of white dwarf explosion, is less well understood than type II ones [14].

Core collapse type II SN explosions are usually the last processes in the evolution of stars with masses greater than approximately 8 times the mass of The Sun [1]. The life of such stars proceeds through a well defined series of nuclear burnings, which is mainly: hydrogen $\rightarrow$ helium $\rightarrow$ carbon $\rightarrow$ neon $\rightarrow$ oxygen $\rightarrow$ silicon $\rightarrow$ iron [15], together with other nuclei that are also formed. While these nuclear reactions are occurring, the core of the star is getting hotter and denser under the continuous action of gravity. The interest for this work resides in the last step, when the star has become an iron core star, surrounded by concentric shells that are the relics from its previous burning phases. Iron is believed to be the last element that is produced by fusion in the core of these stars. The well known reason is that it is not energetically favorable to produce heavier nuclei than ^{56}Fe by fusions, nevertheless, as figure 2.1 shows, ^{62}Ni has the highest binding energy per nucleon. The reason why ^{56}Fe is usually mentioned as the most stable nuclei comes from astrophysicist. During the silicon phase of the core star evolution, gamma rays generated in the core have energy enough to produce photondesintegration of the nuclei. The competition between the fusions and the photodesintegration induced by γ_s produces the isotope ^{56}Ni more likely than ^{62}Ni [16]. ^{56}Ni decays via β^+ into ^{56}Co, which subsequently decays via β^+ into ^{56}Fe[1].

When such massive stars becomes a Fe-core star, a supernova explosion takes place, resulting in a neutron star or, if the mass of the star was big enough, in a black hole [13, 18]. To understand the relevance of neutrinos in this process, it is necessary to understand how the core-collapse supernova explosion develops.

[1]The statement that ^{56}Fe is the most tightly bound nucleus appeared in the field of astrophysics around 1960, and the idea spread into astrophysics literature. The difference in the mean binding energy per nucleon between the two nuclei is so small that it has almost no effect on stellar nucleosynthesis [16].

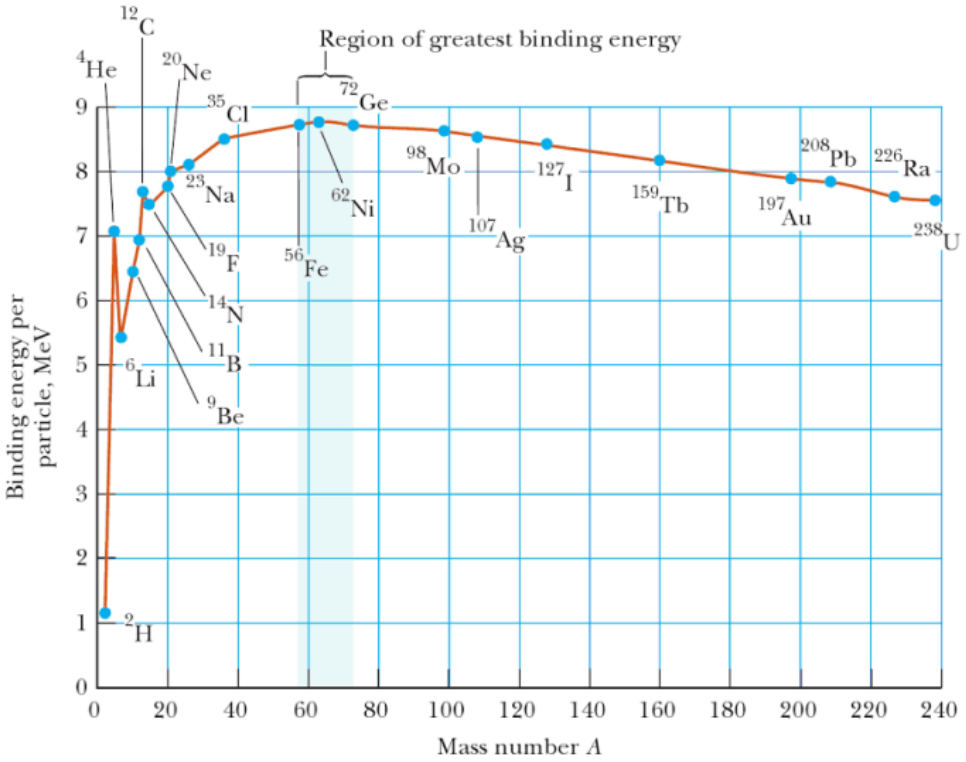

Figure 2.1: Binding energy per nucleon mass number for nuclei that lie along the line of stability. Taken from [17].

In a star, the huge pressure from its own gravitational force is counteracted with the photon pressure from the nuclear processes (mainly thermonuclear fusions) that take place in the core. The fusions make the core to have heavier nuclei as the star is getting older. Fusions release a significant amount of energy, which is used to counteract radiative losses. This stable state is called *hydrostatic equilibrium* [13]. While the nuclei in the core changes following the sequence described above, the core is getting compressed, since heavier nucleus need more energy for further fusions, and the amount of released energy decreases. In order to sustain the internal core pressure, the burning rate needs to increase.

The burning rate also increases as energy is being removed from the core by emitting neutrinos and antineutrinos, in a process named *the Urca Process*[1] [13, 19]. As the core becomes hotter and denser, electrons inside it has higher energies. When these electrons are energetic enough[2], they are able to undergo electron capture with the nuclei: $(N, Z) + e^- \rightarrow (N + 1, Z - 1) + \nu_e$. Usually, the produced nuclei are not in their ground states, and will likely decay via β^-: $(N + 1, Z - 1) \rightarrow (N, Z) + e^- + \bar{\nu}_e$, which produces an electron-antineutrino pair. Since the electron is produced inside the core, it usually has enough energy to produce electron capture. The Urca Process is repeated endlessly,

[1] During a conference in Urca, Brasil, physicists G. Gamow and M. Schoenberg were discussing about this topic while they were visiting the local casino, when they pointed out that the energy disappears in the nucleus of the supernova as quickly as the money disappeared at the roulette table [13].

[2] The threshold energy of electron capture depends on the nucleus itself, so it can not be claimed that electron capture starts in a core when electrons have certain energy. With the increase of electron energies, they are able to produce electron capture to heavier nucleus in the core and with higher probability, since cross section of electron capture increases with the electron energy. It is assumed that Urca Process starts with electron energies around 0.25 MeV [20].

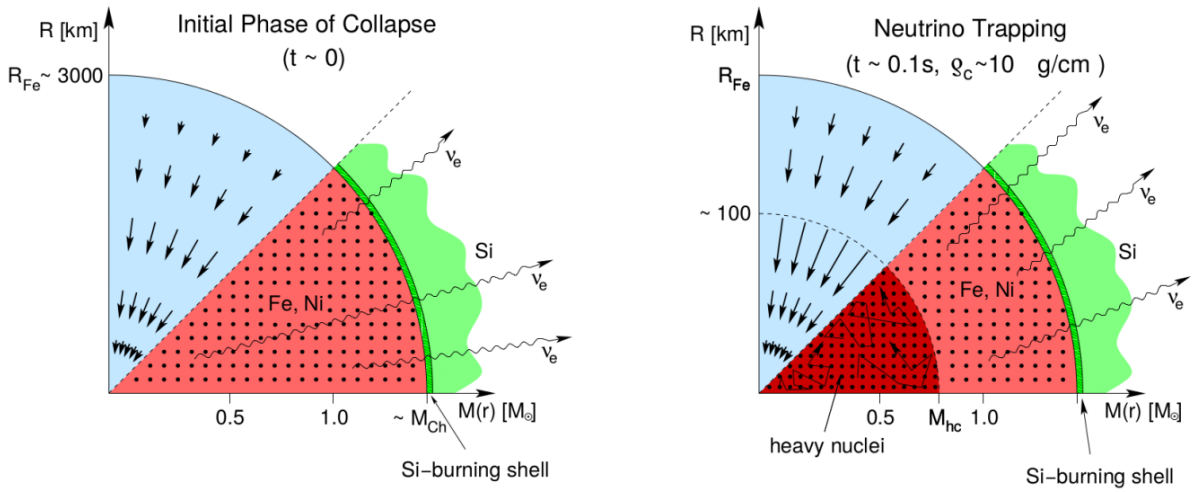

Figure 2.2: Initial phase of core-collapse (**left**) and neutrino trapping (**right**) of a supernova explosion. M_{Ch} stands for the Chandrasekhar mass and M_{hc} for the mass of the subsonically collapsing. Figures taken from [22].

while neutrinos and antineutrinos are slowly draining energy from the core, which further compresses the core.

As announced before, once the core contains mainly iron, thermonuclear fusions stop. Since the core is not producing energy against the gravitational pressure anymore, the core starts to implode; the supernova process has begun with the *core collapse*. Compression makes the core temperature increases above 5 billions Kelvins (0.5 MeV per particle) [13]. At this temperature, photons are able to dissociate iron into α particles and neutrons, and later into protons and neutrons via photodesintegration:

$$\gamma + {}^{56}Fe \rightarrow 13\alpha + 4n \tag{2.1}$$

$$\gamma + \alpha \rightarrow 2p + 2n. \tag{2.2}$$

Since the core is getting compressed, the density increases so much that a quantum state of electrons appears, called *degenerate electron gas*. Even if theoretically a degenerate Fermi gas assumes that the fermions do not interact with each other, this approach works well to study how the energy of the electrons inside the core rises up. The huge density inside the core lets electrons behave like a Fermi gas in which no two fermions can have the same quantum state. Since lower energies are filled first, additional electrons must have higher and higher energies. This boosts electron energies well above thermal energies and speeds up nuclear electron capture. Thus, in this Fermi, gas e^- reach energies above 2.25 MeV and electron capture over free unbound protons starts to appear [13, 21]:

$$p + e^- \rightarrow n + \nu_e. \tag{2.3}$$

If the core of the star is not massive enough, the pressure of the degenerate Fermi gas would stop the collapse, resulting in a white dwarf. The Chandrasekhar mass, $M_{\mathrm{Ch}} \sim 1.4\,\mathrm{M_{sun}}$, limits the mass of the core at which the degenerated electron gas can not stand

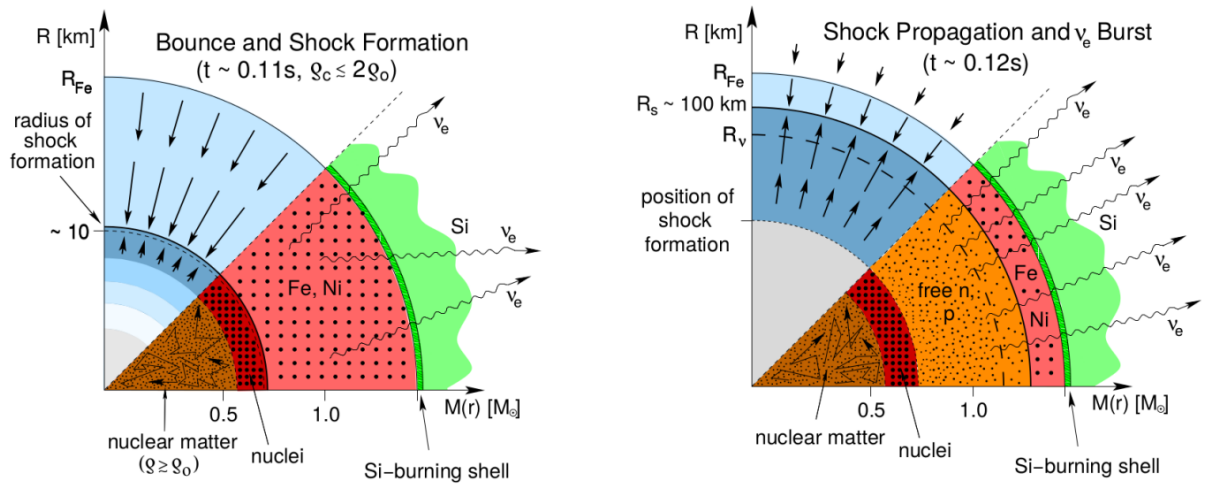

Figure 2.3: Core bounce and shock formation in (**left**), and shock propagation in (**right**) of a supernova explosion. R_ν stands for the radius of the neutrinosphere. Figures taken from [22].

the gravitational pressure. If the core exceed the Chandrasekhar limit, which is the general situation for stars heavier than 8-9 solar masses, the star keeps collapsing and the core density increasing [14]. This rise up the energy of the electrons and encounters between free protons and electrons become more and more likely. Thus, the rate of electron capture increases dramatically. This stage of the supernova process is called **neutronization**, since the result of the electron capture are neutrons and neutrinos. Also, as density increases, gravitational forces become stronger, which makes the collapse accelerate further and further. When density reaches a level of about $10^{14}\,\mathrm{g/cm^3}$, neutrinos start to be trapped in the core, because their diffusion time becomes larger than the collapse time due to elastic scattering via neutral current interactions of neutrinos off neutrons (and, to a lesser extent, protons). Therefore, a huge number of neutrinos from the neutronization are being produced inside the core and getting trapped there. A sketch of the core collapse and neutrino trapping is shown in Fig. 2.2.

When density is about $10^{14}\,\mathrm{g/cm^3}$, repulsive nuclear forces start to come into play. The feedback cycle continues until the core has a density of about $6 \cdot 10^{14}\,\mathrm{g/cm^3}$ (this is around 3 times the nucleon density!) [21]. At this density, the nuclear forces stop the core collapse in an abruptly way. It is remarkable that the core collapse takes only ~ 1 second since it starts until nuclear forces stop it, but material in the outer part of the star is still falling inward at around $6 \cdot 10^4\,\mathrm{km/s}$. At this point, since compression is not possible anymore, the core bounces in response to the increased nuclear matter pressure. This bounce drives a shock wave of dense matter at about $10^4\,\mathrm{km/s}$ into the outer core, which is still falling inward [13, 22]. This dynamic event is known as *core bounce*, and is shown in Fig. 2.3 left.

Within few milliseconds, the shock loses its energy and stops its rapid outward movement. The dense layer of material behind the shock front does not fall into the core again due the gravitational forces because it is supported by the high pressure of the degenerate Fermi gas. This results in a hot and dense layer of buoyant matter (also called quasi-static layer) behind the still slowly expanding shock front. The electrons remain trapped because their free path is much shorter than the radius of the proto-neutron star, but neutrinos takes

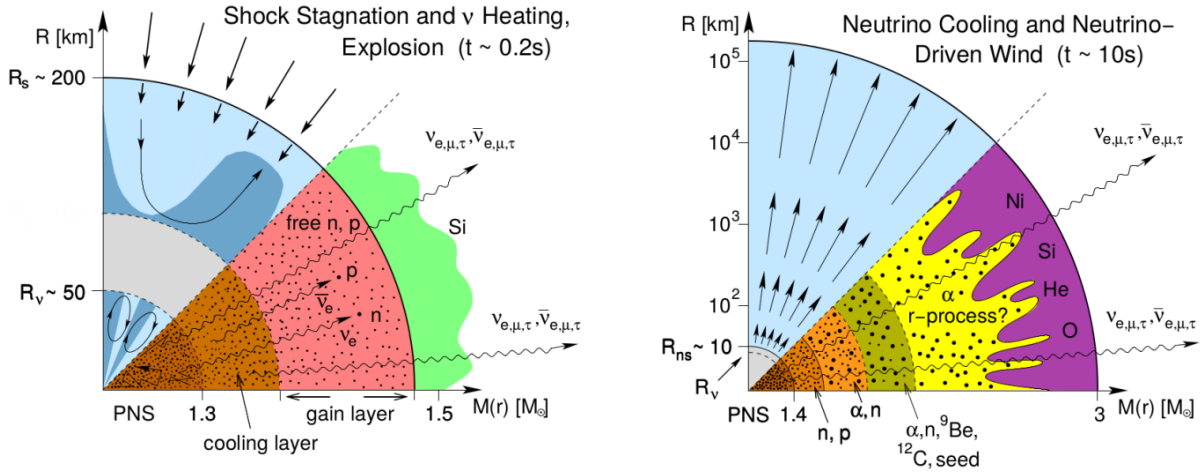

Figure 2.4: Explosion and last phase in a supernova process. R_s is the radius of the shock layer and R_{ns} is the radius of the neutron star. Figures taken from [22].

a fraction of a second to diffuse out from the inner core. These neutrinos will find the buoyant layer and deposit some of their energy in it, mainly by charged-current neutrino-antineutrino captures of free nucleons: $\nu_e + n \rightarrow e^- + p$ and $\nu_e + n \rightarrow e^- + p$. These are the neutrinos that were generated during the neutronization phase, and the large number of them emitted at this point can be seen in the neutrino fluxes as a peak denominated *neutronization peak*. This process is illustrated in Fig. 2.3 right.

The shock front gets hotter as it is getting energy from the neutrinos that are passing through it in what is called *the accretion phase*, producing its expansion and eventually the supernova explosion [13, 21, 22]. The accretion phase is illustrated in 2.4 left. It is remarkable how the weak interactions of neutrinos are the main creators of such a violent supernova explosion. At this point, simulations had failed over many years. Since stars seem to have spherical symmetry and computers were not powerful enough, simulations were made in a one-dimensional simplification, which led to some of them where the supernova did not explode. In fact, even if there is spherical symmetry, convective hydrodynamics come into play. Since there is a huge gradient of temperature between the inner core and the shock front, convection fluxes appear. Hot buoyant material can rise in one part of the star to be replaced by cooler material falling down in other regions. This hydrodynamic instabilities make the star explodes in forms of bubbles that have enough energy to escape, since there is less and less material in its path. The burst of neutrinos occurs within 10 seconds since the supernova process started. In Fig. 2.4 right the last phase of the supernova process is depicted. Afterwards, depending on the mass, the star will condense into a neutron star or into a black hole. In Fig. 2.5 the result of a computer simulation of neutrino-driven convection with the formed bubbles is shown.

Electromagnetic radiation produced in supernovas only escape from the star when they have been generated mainly in its most outward areas, so they cannot convey to us any information about the dense and deep region relevant for the explosion mechanics. Charged particles which are emitted are also mostly produced in the outer region, and, in addition, they are affected on their path to us due to cosmic magnetic fields. Thus,

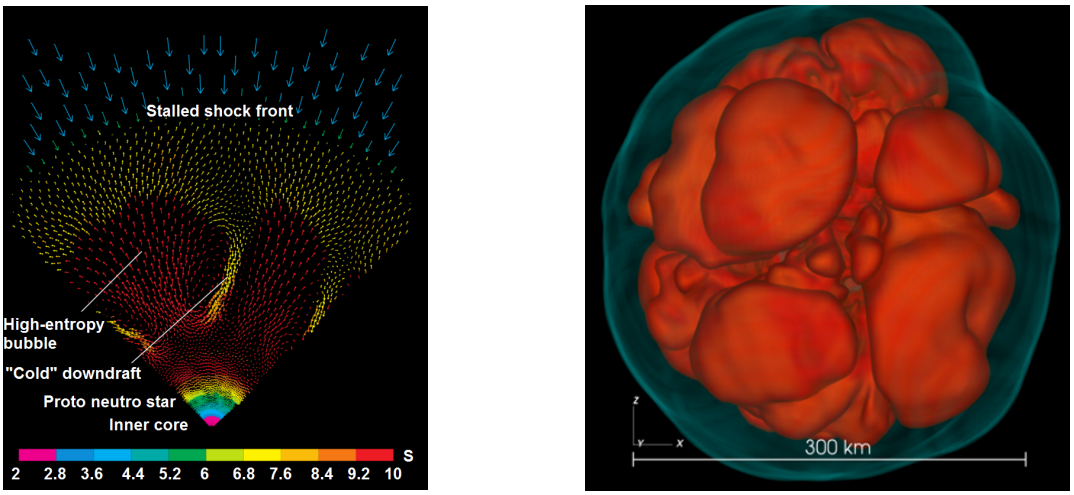

Figure 2.5: Left: Supernova simulation 50 ms after the bounce. Colors show the level of the entropy. Convection fluxes of bubbles and cold downdraft can be seen as changes in the entropy. Near the core, energetic neutrinos from the proto-neutron star are absorbed in the quasi static layer. High entropy bubbles are already rising and will transfer their energy to the stalled shock front, which at the end will make the explosion. Figure taken from [13]. **Right:** 3D simulation of 27 solar masses primary star. Surfaces of constant entropy are displayed in yellow and red; the SN shock is visible as a bluish, semitransparent envelope. Figure taken from [23].

the detection of a neutrino burst by neutrino telescopes is almost the only possibility to obtain direct information about the explosion mechanism [13, 24].

Neutrinos are emitted from supernovae in all flavours. The main reactions which produce neutrinos during the whole process are the electron capture and the β^+ decay, but also thermal neutrino-antineutrino production occurs, generating neutrinos of all flavours [14]:

$$e^+ + e^- \rightarrow \nu_{e,\mu,\tau} + \overline{\nu}_{e,\mu,\tau}. \tag{2.4}$$

Oscillation of neutrinos in their path from the supernova to Earth detectors also changes the neutrino flavour ratio depending on the model which is considered, i.e. normal hierarchy or inverse hierarchy. It is not the goal of this work to discuss about the effects of neutrino oscillation, thus in all the work a model of no oscillation will be used, therefore what reaches Earth will be the same neutrino flavour rate than the one is produced in the supernova.

2.2 SN neutrino interactions

Neutrinos coming from core-collapse supernovae can interact with the matter in different ways. Among them, this work will present results for two of them, which are the most important interactions of MeV neutrinos in ice [12]. These interactions cover 95.8% of the

expected signal by SN neutrinos in current Icecube [25].

2.2.1 Inverse Beta Decay (IBD)

For neutrino energies below $\sim 60\,\mathrm{MeV}$, the inverse beta decay (IBD),

$$\bar{\nu}_e + p \rightarrow n + e^+, \tag{2.5}$$

has the largest cross section of SN neutrino interactions in ice or water [12, 24]. In this charged current (CC) interaction, an antineutrino interacts with one of the protons of the medium to induce the IBD, creating a positron and a neutron. Usually the neutron stays in the nucleus while the positron is emitted, carrying out most of the energy of the antineutrino. The generated positron can produce Cherenkov light if it has been generated in a dielectric medium when its energy is big enough, which can be used in Cherenkov-based detectors to observe it. In section 3.1 it will be explained how these Cherenkov based detectors works.

It is straightforward to obtain that IBD has an energy threshold of about $\epsilon_\nu^{th} \sim 1.8\,\mathrm{MeV}$, below which IBD is not possible[1]. The total cross section of the process can be obtained as [26]:

$$\sigma = \frac{m_e G_F}{\pi}(1+\alpha^2)(1+\delta_{WM})\frac{(\epsilon_\nu - \Delta_{mn})p_e}{m_e^2}, \tag{2.6}$$

where m_e and p_e are the mass and momentum of the emitted positron, $G_F = 1.166 \cdot 10^{-5}\,\mathrm{GeV}^{-2}$ is the Fermi constant, $\alpha \sim 1.26$ is the axial-vector coupling constant, $\delta_{WM} \approx -0.0035 \cdot (\epsilon_\nu - \Delta_{mn}/2)\,\mathrm{MeV}^{-1}$ is the weak-magnetism correction and Δ_{mn} stands for the mass difference between neutron and proton, $\Delta_{mn} = m_n - m_p$. Notice that ν stands for electric antineutrino and the subindex e always refers to positron, but the notation has been simplified. This and the rest of the formulas of this section are given in natural units, where $h = c = 1$. The cross sections presented here are approximations to free nucleons, but they have accuracy enough to describe the interaction between $\overline{\nu}_e$ and a hydrogen nucleon from H_2O [12].

The angular cross section of this interaction has been parametrised in [24] in orders of $1/m_p$, and it has the form:

$$\left(\frac{d\sigma}{d\Omega}\right)^{(1)} = \frac{\sigma_0}{2\pi}\left[f^2 + 3\alpha^2 + (f^2-\alpha^2)v_e^{(1)}\cos\theta\right]E_e^{(1)}p_e^{(1)} - \frac{\sigma_0}{2}\left[\frac{\Gamma}{m_p}\right]E_e^{(0)}p_e^{(0)}, \tag{2.7}$$

where $\sigma_0 = G_F^2\cos^2\theta_c(1+\Delta_{inner}^R)$ with $\cos\theta_c \approx 0.974$ and $\Delta_{inner}^R \simeq 0.0024$, $f = 1$ is the vector coupling constant, E_e is the energy of the emitted positron, Γ is a parameter which

[1] In all these results, it is assumed that the proton is at rest.

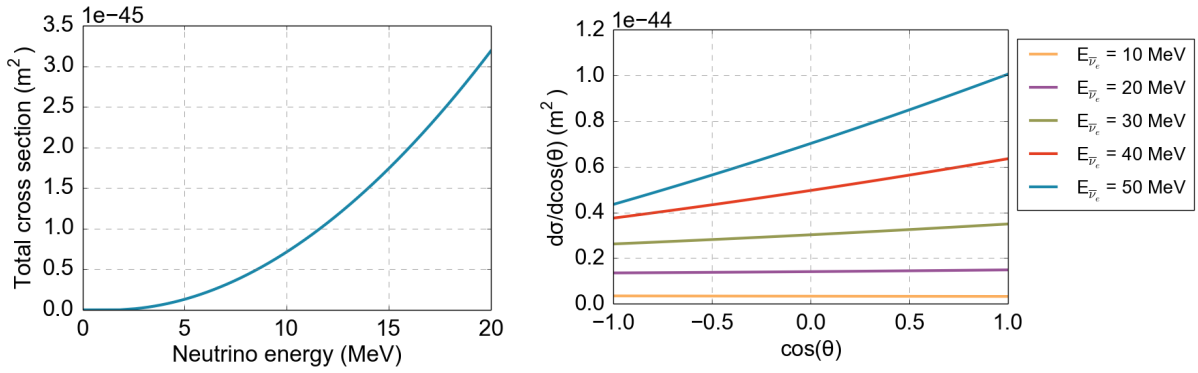

Figure 2.6: Left: Total cross section (Eq. 2.6) and **right:** angular cross section (Eq. 2.7) of the inverse beta decay. The total cross section is presented as a function of the energy of the incident antineutrino, while the angular cross section is depicted for different energies of the incident antineutrino as a function of $\cos\theta$, where θ is the angle of the emitted positron with respect to the incident antineutrino.

depends on the energy of the incident antineutrino and the super indexes (0) and (1) are the order level of $1/m_p$ approximation as described in [24]. θ stands for the angle of the outgoing positron with respect to the incoming antineutrino. The energy of the emitted positron can be obtained from θ and the energy of the incident antineutrino as [24]:

$$E_e^{(1)} = E_e^{(0)}\left[1 - \frac{E_\nu}{m_p}(1 - v_e^{(0)}\cos\theta)\right] - \frac{(\Delta_{mn}^2 - m_e^2)^2}{4m_p}, \tag{2.8}$$

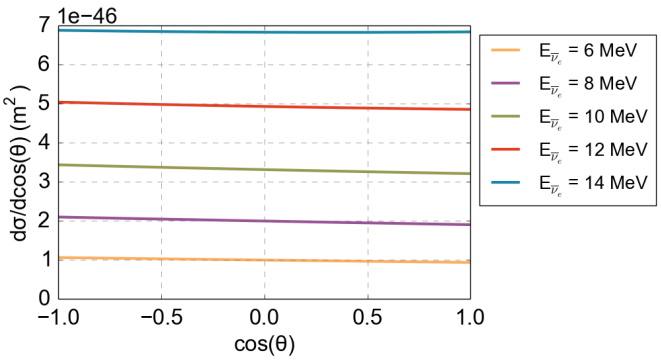

Figure 2.7: Angular cross section of inverse beta decay for low energies of the incident antineutrino, depicted as a function of $\cos\theta$, where θ is the angle of the emitted positron with respect to the incident antineutrino.

In Fig. 2.6 the total cross section and the angular cross section of IBD are depicted. It can be appreciate that the probability that the interaction occurs increases with the energy of the antineutrino. Fig. 2.6 right shows that for higher energies the direction of the positron have a forward preference, however, for lower energies there is almost no angular preference, with slightly higher values for backward directions, as can be appreciated in Fig. 2.7. Next section will show that most SN antineutrinos have energies below ∼25 MeV, which results in almost no angular preference for the emission of the positron. Therefore, this interaction has the biggest cross section but it is expected to do not conserve the direction of the incoming antineutrino.

2.2.2 Electron neutrino - electron elastic scattering (ENEES)

The electron neutrino - electron elastic scattering (ENEES),

$$\nu_e + e^- \rightarrow \nu_e + e^-, \tag{2.9}$$

is about 100 times less probably to occur than IBD. Nevertheless, it has the largest cross section for SN neutrinos in ice or water [1], and only the IBD of SN antineutrinos presents a larger cross section. The total cross section is given by [27]:

$$\sigma = \frac{G_F m_e E_\nu}{2\pi}\left[\frac{4}{3}\sin^4\theta_w + (1+2\sin^2\theta_w)^2\right], \tag{2.10}$$

where θ_w is known as the weak mixing Weinberg angle, which will be taken as $\sin^2\theta_w = 0.231$ [27]. Here, ν always refers to the incident electric neutrino and e stands for the emitted electron. Unbound electrons have been assumed in the study of this interaction. The angular cross section can be obtained as [28]:

$$\frac{d\sigma}{d\cos\theta} = \frac{2G_F^2 m_e^2}{\pi}\frac{4E_\nu^2(m_e+E_\nu)^2\cos\theta}{\left[(m_e+E_\nu)^2 - E_\nu^2\cos\theta\right]^2}\cdot \\ \cdot\left[g_1^2 + g_2^2 + \left(1 - \frac{2m_e E_\nu\cos^2\theta}{(m_e+E_\nu)^2 - E_\nu^2\cos\theta}\right)^2 - g_1 g_2\frac{2m_e\cos^2\theta}{(m_e+E_\nu)^2 - E_\nu^2\cos\theta}\right], \tag{2.11}$$

where the quantities g_1 and g_2 depends on the flavour of the neutrino, which in this case gives $g_1 = 0.73$ and $g_2 = 0.23$. In Fig. 2.8 the total and angular cross sections have been depicted. It can be seen that the cross sections are about 100 times smaller than for the IBD. Fig. 2.8 right shows a strong peak in the angular cross section when $\theta \rightarrow 1$, which means that ENEES conserves very well the direction of the incoming neutrino. Therefore, this interaction can be used to reconstruct the direction of the incident neutrinos and to point to the source of the detected neutrinos.

From the angle and the energy of the incident neutrino, the energy of the outgoing electron is determined by [28]:

$$E_e = \frac{2m_e E_\nu^2\cos^2\theta}{(m_e+E_\nu)^2 - E_\nu^2\cos\theta}. \tag{2.12}$$

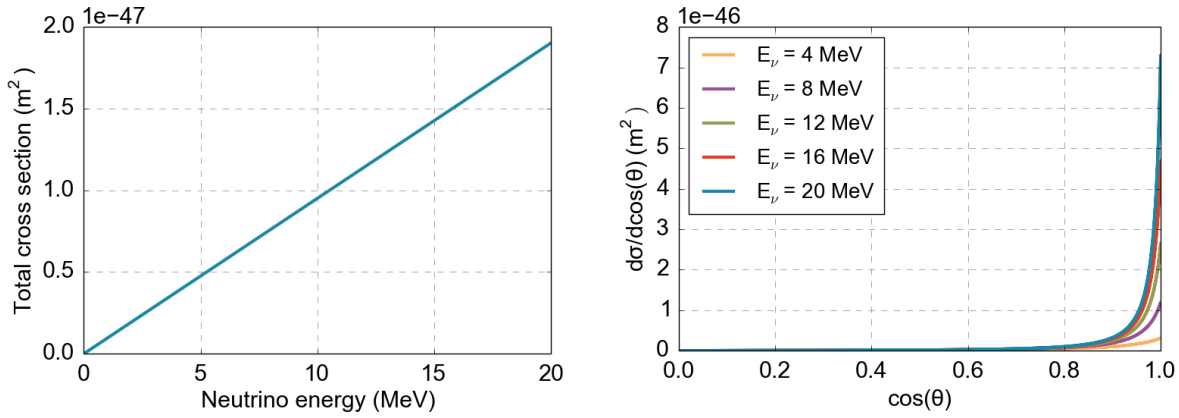

Figure 2.8: Left: Total cross section (Eq. 2.6) and **right:** angular cross section (Eq. 2.7) of the electron neutrino - electron elastic scattering. The total cross section is presented as a function of the energy of the incident neutrino, while the angular cross section is depicted for different energies of the incident neutrino as a function of $\cos\theta$, where θ is the angle of the emitted electron with respect to the incident neutrino.

2.2.3 Other interactions

Other interactions of neutrinos and antineutrinos in the SN burst energy range are also possible to occur in ice, such as $\bar{\nu_e} + {}^{16}O \rightarrow e^- + {}^{16}F^{(*)}$, $\nu_e + {}^{16}O \rightarrow e^+ + {}^{16}N^{(*)}$, and elastic scatterings as $\bar{\nu}_e + e^- \rightarrow \bar{\nu}_e + e^-$, $\nu_\mu + e^- \rightarrow \nu_\mu + e^-$ or $\nu_\tau + e^- \rightarrow \nu_\tau + e^-$, together with some others [1, 12]. These interactions will not be studied in this work, since they have much smaller cross section than IBD or ENEES. Therefore the results presented in this work would assumed that IBD and ENEES are the only two interactions that SN neutrinos and antineutrinos produce in ice. A summary of all possible interactions can be found in [12]

2.3 A supernova burst model

Since the development of a core-collapse supernova explosion is not totally well understood yet, for the purpose of this work models which contain the neutrino and antineutrino fluxes produced in a SN explosion are necessary, which have been kindly provided by *T. Hanka*[1] [29]. The models contain the luminosity, mean energy and square mean energy of neutrinos and antineutrinos depending on the time of the SN burst. Here, the fluxes for two different SNe are presented:

- A *heavy* SN, which results in a baryonic neutron star of about 1.77 M_{sun} and whose progenitor mass is about 27.0 M_{sun}.

[1] Max-Planck institute for astrophysics in Garching

- A *light* SN, which results in a baryonic neutron star of about 1.36 M_{sun} and whose progenitor mass is about 9.6 M_{sun}.

These are well lower and upper limits to stars which produce a neutron star, since heavier stars than ~ 30 solar masses result into black holes instead of neutron stars, while lighter stars than ~ 8 solar masses would produce a white dwarf [29]. The presented fluxes for each star were obtained from two different models which use different equation of state (EoS): the *LS220* (Lattimer-Swesty's) EoS [30], and the *SFHo* EoS [31]. Only the fluxes of the electron neutrino and antineutrino will be studied, since they are involved in the interactions taking into account in this work.

2.3.1 Fluxes and rate of events

The luminosity and mean energy of both neutrinos and antineutrinos from the models are depicted in Fig. 2.9 and Fig. 2.10. In the plots, the x-axis has been re-sized from the original fluxes for a better visualization. Comparing the different SNe, the heavier one shows higher luminosity as well as higher energies for both neutrinos and antineutrinos, therefore it is expected that the rate of detection is higher for heavier SNe. In Fig. 2.9, the different phases of the SN explosion described in section 2.1 can distinguished. At first, neutrinos are emitted while compressing the core until a short decrease appears in the neutrino flux, which is due to the neutrino trapping, followed by a sharp rise. This sharp rise is indeed the neutralization peak explained before. Then, the neutrino and antineutrino fluxes become roughly equal during the accretion phase. The last seconds correspond to the cooling phase, where both neutrino and antineutrino fluxes decrease. The different EoS give very similar values for each SN. Fig. 2.10 shows the mean energy of neutrinos and antineutrinos during the SN explosion, whose shapes differ from the heavier to the lighter SN. The energies are in the range of tens of MeV and, in most phases of the burst, the energy of the antineutrinos is expected to be slightly higher than the energy of the neutrinos. Again both EoS give very similar results for each SN.

Now, the expected rate of events for IBD and ENEES will be calculated. It will be assumed that the SN explosion takes place at 10 kpc of Earth[1]. 10 kpc is approximately the distance from Earth to the galactic center, and that value is frequently used in SN studies. The flux of neutrinos can be obtained by dividing the luminosity and the mean energy. From this, the number of neutrinos that would reach Earth per square meter is obtained assuming that the neutrinos are emitted from the SN in a spherical way using the following expression:

$$\Phi(t) = \frac{1}{4\pi d^2} \cdot \frac{L(t)}{\langle E(t) \rangle}, \tag{2.13}$$

where the distance d would be 10 kpc, $L(t)$ is the luminosity and $\langle E(t) \rangle$ is the mean

[1] A parsec (pc) is a unit of length used in astrophysics to measure big distances. One parsec is the distance at which one astronomical unit subtends an angle of one arcsecond, and it is equal to about 3.26 light years.

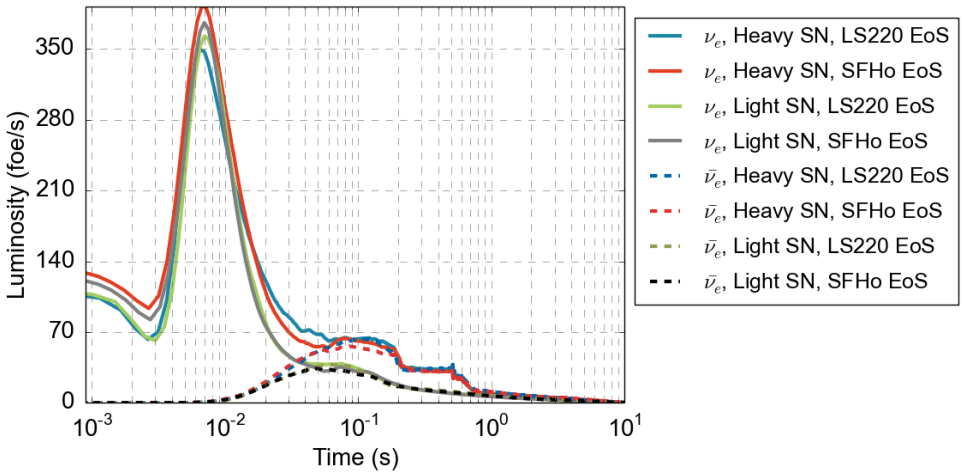

Figure 2.9: Fluxes of SN neutrinos and antineutrinos as a function of the time of the SN explosion, for two different SNe modeled by LS220 and SFHo EoS. Data kindly provided by *T. Hanka* [29].

energy of neutrinos or antineutrinos. Once the flux of neutrinos has been calculated, the rate of events of each interaction can be obtained by using its corresponding cross section and its number of possible targets. Calling N_{target} to the number of possible targets in one m^3 of ice, and assuming that the ice only contains H_2O molecules, N_{target} can be written as:

$$N_{\text{target}} = \frac{\rho \cdot N_a \cdot n}{M}, \tag{2.14}$$

where $\rho = 921.6\,\text{kg/m}^3$ is the density of the ice at -50 celsius degrees[1], $M = 1.8015 \cdot 10^{-4}\,\text{kg/mol}$ is the molar mass of H_2O, N_a is the Avogadro number and n is the number of targets per molecule. Then, it will be assumed that there are n = 10 possible targets per molecule for ENEES, so 10 electrons per molecule. In the case of the IBD, n = 2 targets per molecule will be considered. It should be noticed here that in the IBD one talks about protons referring to the hydrogen nuclei in the H_2O molecules. With all this, the rate of events can be calculated as:

$$r(t) = \sigma \cdot \Phi(t) \cdot N_{\text{target}} = \sigma \cdot \Phi(t) \cdot \frac{\rho \cdot N_a}{M} \cdot n. \tag{2.15}$$

From Eq. 2.15, the rate of the interactions is obtained and depicted in Fig. 2.11. Because of the larger cross section of the process, the rate of IBD is higher than the ENEES one, even if Fig. 2.9 shows that the flux of neutrinos is bigger than the flux of antineutrinos. If the curves of Fig. 2.11 are integrated, it is obtained the expected number of ENEES

[1]Density changes with the temperature and the depth of the South Pole ice, as well as the temperature presents seasonal and annual variations. The value of the density used here is therefore not a fix value but the most common one. In order to be consistent, this same value will be used in the rest of the work. Some more information about South Pole ice temperature and density properties can be found in [32] and [33].

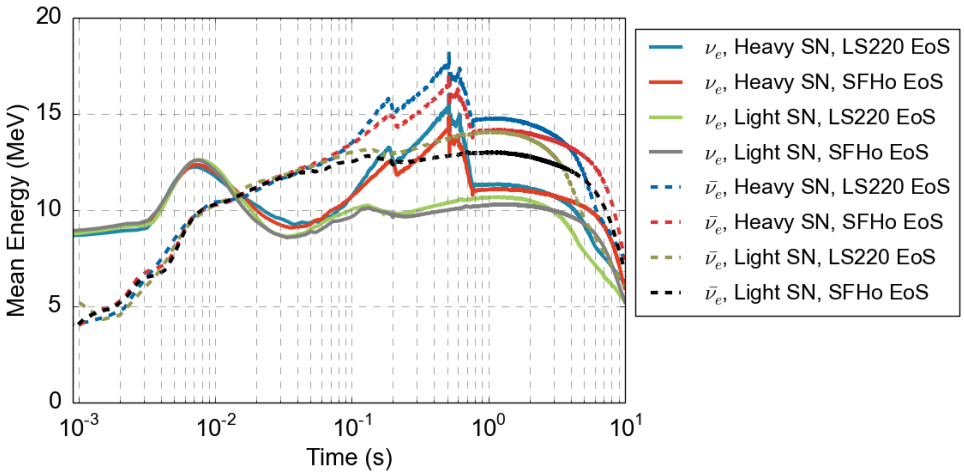

Figure 2.10: Energies of SN neutrinos and antineutrinos as a function of the time of the SN explosion, for two different SNe modeled by LS220 and SFHo EoS. Data kindly provided by *T. Hanka* [29].

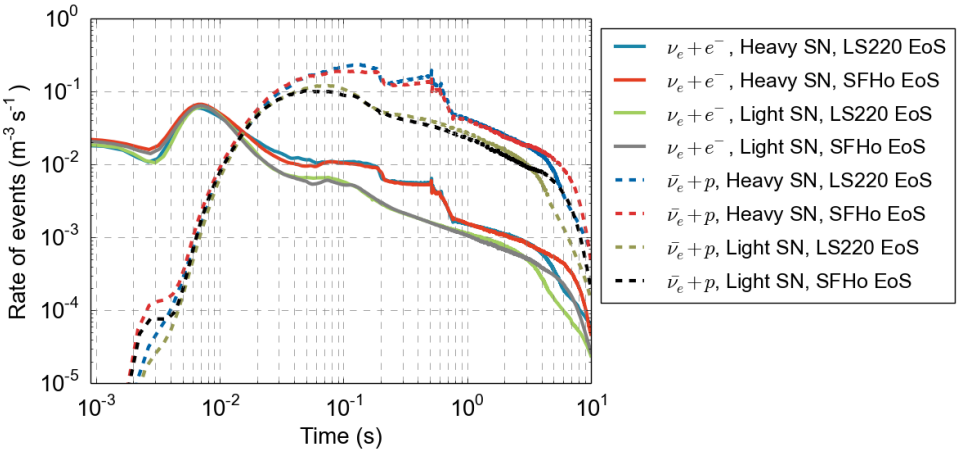

Figure 2.11: Rate of inverse beta decay and electron neutrino - electron elastic scattering per cubic meter of neutrinos coming from a two different SNe at 10 kpc, which has been modeled by LS220 and SFHo EoS.

and IBD produced by a neutrino burst coming from a core-collapse SN per cubic meter of South Pole ice. The results are summarized for the considered SNe models in table 2.1, assuming that the SN explosion takes place at 10 kpc of The Earth. The results show that number of expected interactions of IBD is about 20 times larger than of ENEES, relation that is satisfied for each model of both SN. It is expected that the heavier SN produces about twice more interactions than the lighter SN, because of its larger luminosity and energy spectra. In all cases, the number of interactions per cubic meter is very low, one of the reasons why neutrino telescopes need huge volumes in order to detect a considerable number of them.

Table 2.1: Expected number of interactions produced by a neutrino burst coming from a SN at 10 kpc obtained by integrating Eq. 2.15 from $t = 0$ to $t = 10\,\mathrm{s}$, using the SN fluxes kindly provided by *T. Hanka* [29]. The results are given for a heavy SN, which stands for a star of $27.0\,\mathrm{M_{sun}}$ that results in a $1.77\,\mathrm{M_{sun}}$ neutron star, and for a light SN, which stands for a star of $9.6\,\mathrm{M_{sun}}$ that results in a $1.36\,\mathrm{M_{sun}}$ neutron star. Each SN is presented with its result for fluxes with LS220 or SFHo as equation of state.

Interaction	Supernova	Number of interactions ($\mathrm{m^{-3}}$)	
		LS220	SFHo
$\nu_e + e^-$	Heavy SN	1.02×10^{-2}	1.06×10^{-2}
	Light SN	0.56×10^{-2}	0.57×10^{-2}
$\bar{\nu_e} + p$	Heavy SN	2.09×10^{-1}	2.09×10^{-1}
	Light SN	0.94×10^{-1}	0.96×10^{-1}

2.3.2 Energy distribution of SN neutrinos/antineutrinos

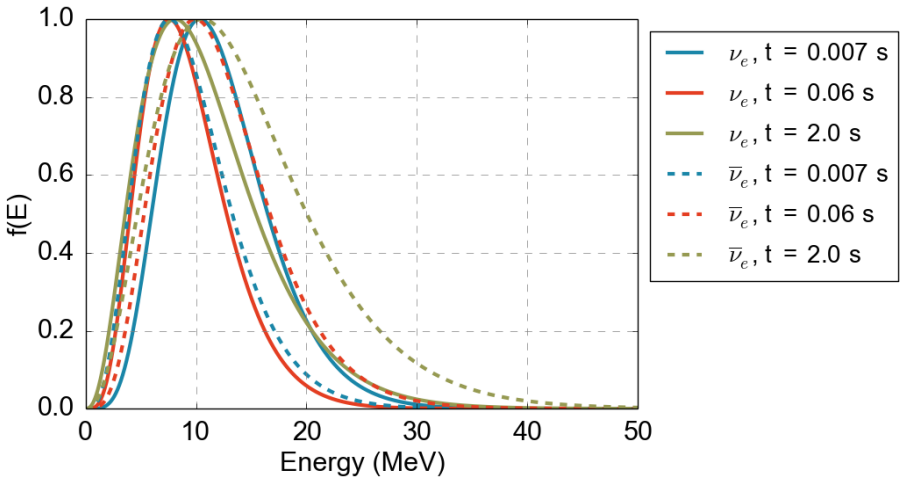

Figure 2.12: Core-collapse SN neutrino and antineutrino energy distributions obtained from the model of [34, 35] and scaled to 1, at different times of the SN burst.

A simple way to present SN neutrinos and antineutrinos spectra has been modeled in [34, 35]. The spectra is given by:

$$f_\alpha(E) = E^\alpha \cdot e^{-(\alpha+1)E/\langle E \rangle}, \tag{2.16}$$

where the α parameter can be obtained from:

$$\frac{\langle E_\nu^2 \rangle}{\langle E_\nu \rangle^2} = \frac{2+\alpha}{1+\alpha}. \tag{2.17}$$

Since the SN models used in this work contain the data of $\langle E_\nu \rangle$ and $\langle E_\nu^2 \rangle$, the neutrino and antineutrino spectra can be obtained from Eq. 2.16. The spectra are shown in Fig. 2.12 for the case of heavy SN with LS220 as EoS, where they have been scaled to one. As expected, antineutrino energy spectra tends to higher energies than neutrino spectra except to the region of the neutronization peak, which correspond to the blue curves at $t = 0.007\,s$. The generally higher energy of antineutrinos results in positrons from inverse beta decays with higher energies than electrons from elastic scatterings. This fact makes positron easier to be detected once they are produced. These details will be studied in next chapters.

3 IceCube and IceCube-Gen2

3.1 Brief introduction to Cherenkov-based detectors

Neutrinos interact so weakly that it is colloquially said that they pass through everything. How such an elusive particle can be detected? An object as a direct neutrino detector might not exist, since neutrino would simply pass through the mechanism. Also, because they have no charge, they do not ionize the medium they pass through, leaving no trace in their path. Hence, neutrinos can only be detected in an indirect way.

The detection of the Cherenkov radiation[1] emitted by charged particles produced in neutrino interactions is, by far, the most efficient method to detect neutrinos [7]. All flavours of neutrinos and antineutrinos interact by weak interactions with matter: from scattering to inverse beta decays. Among the resulting particles from the neutrino interactions, a charged particle which carries part of the energy of the neutrino is often found. This charged particle can be easily detected if it is produced in the proper medium [36].

A dielectric medium gets briefly polarised when a charged particle moves through it, since the charged particle disturbs the electromagnetic fields in it. Usually the disturbance elastically relaxes back, but when the particle goes faster than the phase speed of the light in the medium, it leaves a disturbance in its wake, since the medium response is slower than the particle speed [37]. The energy of the disturbance is emitted in form of a coherent shockwave, which is the Cherenkov radiation. The spectrum of the Cherenkov radiation is continuous and the wavelength of emitted photons depends on the refraction index of the medium. In the case of water or ice, visible light is emitted. Photons emitted by Cherenkov radiation form a cone of a fixed angle given by [37]:

$$\cos\theta_c = \frac{1}{n\beta}, \tag{3.1}$$

where $\beta = v_p/c$. Thus, the angle depends on the medium and the speed v_p of the particle. In Fig. 3.1 a sketch of the Cherenkov process for a neutrino interaction is presented. From Eq. 3.1 it becomes clear that $n > 1$ is necessary to produce Cherenkov radiation in a certain medium, since β can not be bigger than one. The amount of energy radiated per unit of length is given by the Frank-Tamm formula as [37]:

$$\frac{dE}{dx} = \frac{q^2}{c^2}\int\left(1 - \frac{1}{\beta^2 n(\omega)^2}\right)\omega d\omega, \tag{3.2}$$

where ω is the angular frequency and q is the charge of the particle. Hence, the amount of energy radiated in Cherenkov radiation increases with the energy and the charge of the particle. Equation 3.2 can be alternatively expressed as [38]:

[1] Named because of its discoverer Pavel Alekseyevich Cherenkov. His discover was recognized later with the novel prize in 1958.

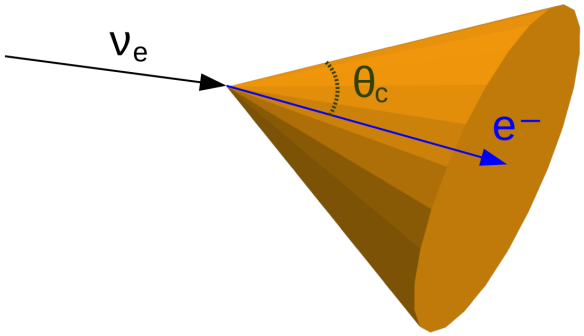

Figure 3.1: Sketch of the Cherenkov photon production for the process $\nu_e + e^- \rightarrow \nu_e + e^-$ in a dielectric medium, depicted as an orange cone. Outgoing neutrino is not drawn.

$$\frac{d^2N_\gamma}{dxd\lambda} = \frac{2\pi\alpha}{\lambda^2}\left(1 - \frac{1}{\beta^2 n^2}\right), \tag{3.3}$$

where λ is the photon wavelength and $\alpha = 2\pi q^2/(hc)$ with h as the Planck's constant. Shorter wavelengths are more intense in Cherenkov radiation, according with the Eq. 3.3. From Eq. 3.1, assuming relativistic energy for the charged particle as $E = \gamma m$, where $\gamma = 1/\sqrt{1-\beta^2}$ and m is the mass of the particle, one finds that the minimum energy E_{min} for a particle to produce Cherenkov light (corresponding to $\cos\theta_c = 0$) is:

$$E_{\text{min}} = m\sqrt{\frac{n^2}{n^2-1}}. \tag{3.4}$$

In Ice, assuming n = 1.33, this results in a minimum energy of $E_{\text{min}} \approx 0.78\,\text{MeV}$. Charged particles produced from neutrino interactions usually have much higher energies, which leads to a large production of Cherenkov photons when passing through the ice. Cherenkov-based detectors use huge volumes of dielectric mediums instrumented with photomultipliers to detect this radiation. Since neutrino interactions are so unlikely, a big volume is necessary to detect a considerable number of them. Usually these detectors need to be isolated as much as possible from potential background sources, specially when low energetic neutrinos are to be detected. These ingredients render neutrino detectors to be remarkable detectors, as e.g. *Super-Kamiokande* [1], which is located 1 km underground in an old mine, or IceCube, which will be described in the next chapter.

3.2 From IceCube to IceCube-Gen2

IceCube is a neutrino telescope built at the Amundsen–Scott South Pole Station in Antarctica [39]. It is the successor of the old *Amanda*[1] detector [40]. IceCube uses one cubic kilometer of South Pole ice as instrumented volume, making it the biggest neutrino detector currently operating [41]. The main goal of IceCube is to map the high energy neutrino sky. The IceCube detector is located 1450 meters beneath the surface. It has 86 vertical strings of 1 km length distributed over an area of 1 km^2 which contains a total of 5160

[1] Antartic Muon And Neutrino Detection Array. It was active from 1995 to 2009.

digital optical modules (DOMs) [42]. South Pole ice is extremely transparent and present very few contaminators, which make it the ideal medium for neutrino detection [33].

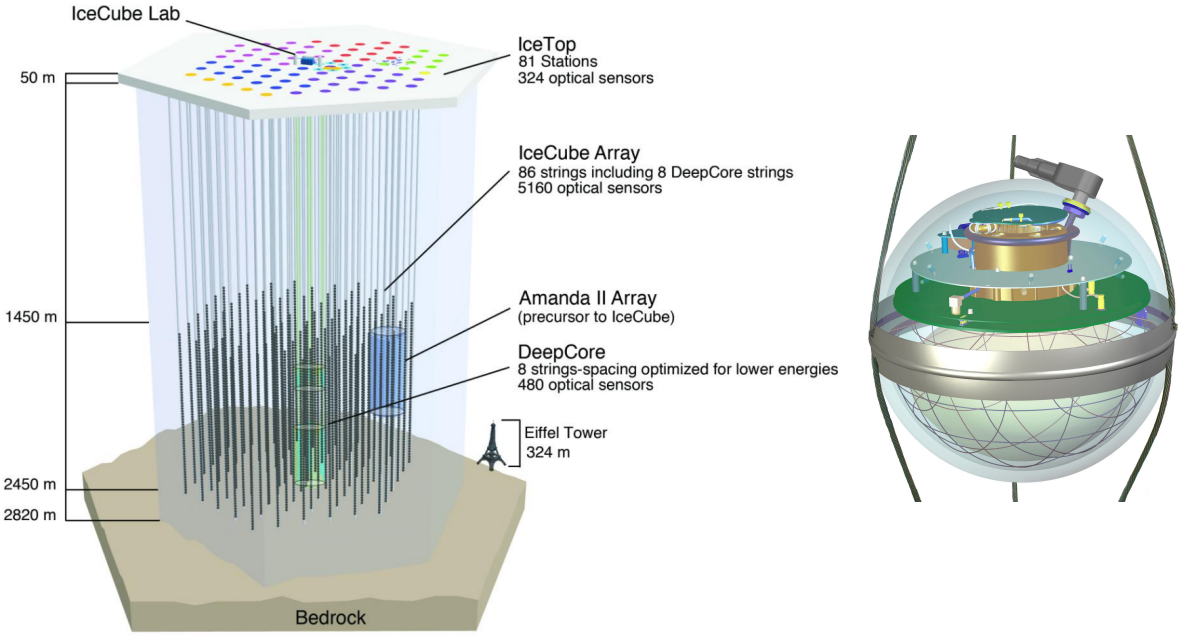

Figure 3.2: Left: Representation of IceCube detector with its different parts. The Eiffel tower is depicted in the lower right part as a size comparison. **Right:** Representation of the digital optical module (DOM). The DOMs have one big photomultiplier facing down. Figures taken from [43].

Fig. 3.2 shows a representation of IceCube and its module. IceCube DOMs are spherical 13-inch glass modules equipped with read-out devices. The pressure glass vessel of the modules needs to stand extreme conditions, since they are exposed to very high pressures up to 550 bars and low temperatures down to -50^o. The DOMs, beneath the South Pole ice, are connected by strings to the IceCube lab at the surface. The photomultiplier (PMT) has a radius of 10 inches and is facing down [42]. The modules are separated vertically by 17 meters and horizontally by 125 meters. This optimizes IceCube to detect neutrinos from energies above 100 GeV, much higher than SN neutrino energies, but that does not mean that lower energetic neutrinos are not detected. IceCube would detect MeV supernova neutrinos as higher counting rates in most of the PMTs in a time window of around 10 seconds, which is the burst duration [39], without information about individual events. To achieve event-by-event detection, coincidences are necessary. A coincident event is defined as an event which is detected in two or more different modules. If an event is detected in one single module, its signal can be easily confused with the background. Since particles produced by SN neutrino interactions travel only about 10 cm in South Pole ice, they are very unlikely to produce coincidences between different modules. On the other hand, the total amount of South Pole volume covered by IceCube optimizes the detector for neutrinos with energies as up to 10 PeV. Higher energetic neutrinos can also be detected, but above these energies the fluxes are so low that an interaction of these neutrinos inside the sensitive volume is very unlikely, leading to a very low rate detection of them. The main neutrino interaction product that IceCube currently measures are muons. Muon tracks appear in IceCube as a light deposition crossing the detector which usually finishes leaving the sensitive volume, since they can travel several kilometers if their energy is big

enough. The direction of the detected particles is reconstructed using the modules that have been hit by Cherenkov photons, together with their hit times.

A sub-detector called *DeepCore* is located inside IceCube. DeepCore is more densely instrumented than IceCube, with distances between the modules of 72 and 7 meters horizontal and vertical respectively, deploying 50 higher efficiency DOMs together with 21 nominal DOMs. With the higher density of modules, DeepCore is optimized to detect neutrinos of energies as low as ∼20 GeV [44].

The discovery of high-energetic cosmic neutrinos with IceCube has opened a new window in astrophysics, but the ability of IceCube to detect these high-energetic neutrinos is limited by the total instrumented volume. A new detector, IceCube-Gen2, is proposed as the next upgrade for IceCube, whose main objective is to detect higher energetic neutrinos and cosmic rays, collecting them at rates significantly higher than IceCube alone [10], using for that $\sim 8\,\mathrm{km}^3$ of South Pole ice as instrumented volume[1]. IceCube-Gen2 is planned to have about 120 new strings, each with 125 modules. The string separation will be around 240 meters. A bigger volume will not only improve statistics but also the reconstruction of muon track directions. The collection of higher statistics samples of astrophysical neutrinos could enable detailed spectral studies, significant point source detections and it also might open the possibility of totally new discoveries [9].

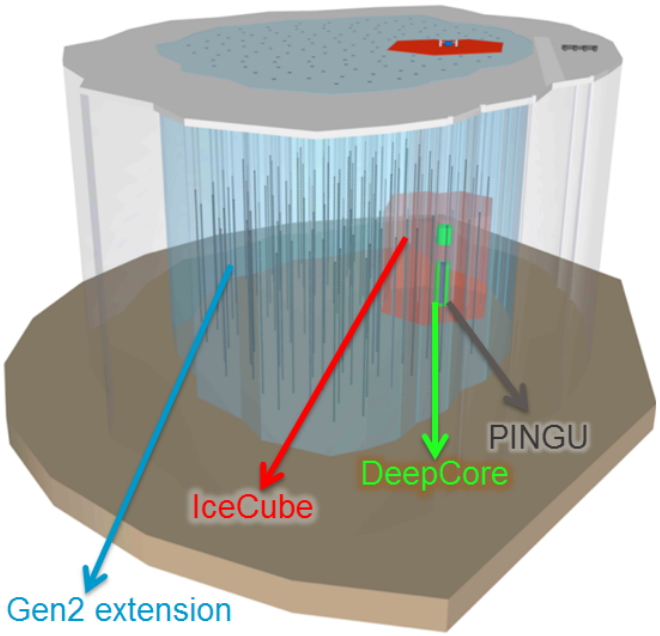

Figure 3.3: Representation of IceCube-Gen2 configuration. In red is plotted the actual IceCube, while the green volume represents DeepCore. In blue is presented what will be the new IceCube-Gen2 volume, where PINGU is depicted in gray as a denser infill extension within DeepCore. Figure taken from [43].

PINGU[2] is planned as a subdetector inside IceCube-Gen2 dedicated to the detection of low energetic neutrinos [45, 46]. It is planned to install 26 extra strings inside a sub-volume of DeepCore, with a string separation of 20 meters and modules distances of 5 meters[3]. This will feature PINGU with the world's largest effective volume for GeV neutrinos. PINGU will focus on getting results about neutrino oscillations, neutrino mass hierarchy,

[1] The total instrumented volume of IceCube-Gen2 is still under discussion, as well as the distribution of its arrays.

[2] Precision IceCube Next Generation Upgrade

[3] The construction of PINGU is still under discussion between the IceCube community, as well as the number of arrays and modules it would have.

muon neutrino disappearance, neutrino tomography of the Earth's core and it will also try to extent the search for solar WIMP dark matter. In Fig. 3.3 a sketch of IceCube-Gen2 with PINGU is shown. With its increased module density, PINGU will improve the sensitivity of IceCube to supernova neutrino bursts. Nevertheless, coincidences of MeV neutrinos interactions will still be very unlikely even with PINGU, expected to be about 1% or less of the total detected events [45]. PINGU started as a project inside IceCube-Gen2, but nowadays is being developed independently. In this work, when referring to IceCube-Gen2, it will be always about the IceCube-Gen2 extension without taking into account PINGU.

3.3 A multi-PMT optical module for IceCube-Gen2

IceCube-Gen2 will not deploy the same modules as current IceCube, since advances in technology allows to install better ones for a similar price. There are several proposals for new digital optical modules for IceCube-Gen2 which plan to improve the measurement characteristics. As one of these proposals, the **mDOM**, acronym for *multi-PMT Digital Optical Module*, can be found. Based on the modules of KM3NeT[1], mDOM keeps a high pressure glass protection, while it uses recent improvements in electronics to reduce complexity and power consumption [11], maintaining a similar cost per photocathode area. The mDOM consists in a module with 24 3-inch PMTs facing all directions. Current DOMs have one single PMT facing down, thus they would likely not detect photons coming from above, while the PMT distribution in mDOMs provides equally detection of photons coming from any direction. Some of the advantages of the mDOM compared to the conventional DOM are [11]:

- Bigger photocathode area: the 24 3-inch PMTs provide a larger photocathode area than one 10-inch PMT.
- Superior photoelectron counting: the signal of several photons in one single PMT gives a multi-photoelectron signal waveform. If these photons are distributed along different PMTs, the number of photoelectrons can be extracted more straight. This is also translated into a better timing resolution.
- Improved angular acceptance: mDOMs provide a near homogeneous 4π coverage, since photosensitive area is distributed along the whole module.
- Directional sensitivity: PMTs orientations provide direct information about the direction of the detected photons, improving the reconstruction of events.
- Background suppression: local coincidences algorithms can be developed in order to suppress correlated background sources. Local coincidences are defined as coincident signals in several PMTs inside the same module.

[1] KM3NeT is a neutrino telescope deployed at three different places under the water of Mediterranean Sea [47].

An illustration of the mDOM is shown in Fig. 3.4. It can be seen that the form of the mDOM is not a perfect sphere in order to maximize the number of PMTs per module. Nevertheless, the radius of the mDOM is slightly bigger than of DOM, which make more expensive to install them beneath the Ice. Around the PMTs, reflector cones are deployed with the objective of improving the effective area of each PMT. Optical gel is used for coupling the PMTs to the glass. The materials for each component of the mDOM are still under study, along with different PMT models. The readout electronics will be based on an extended KM3NeT layout [38].

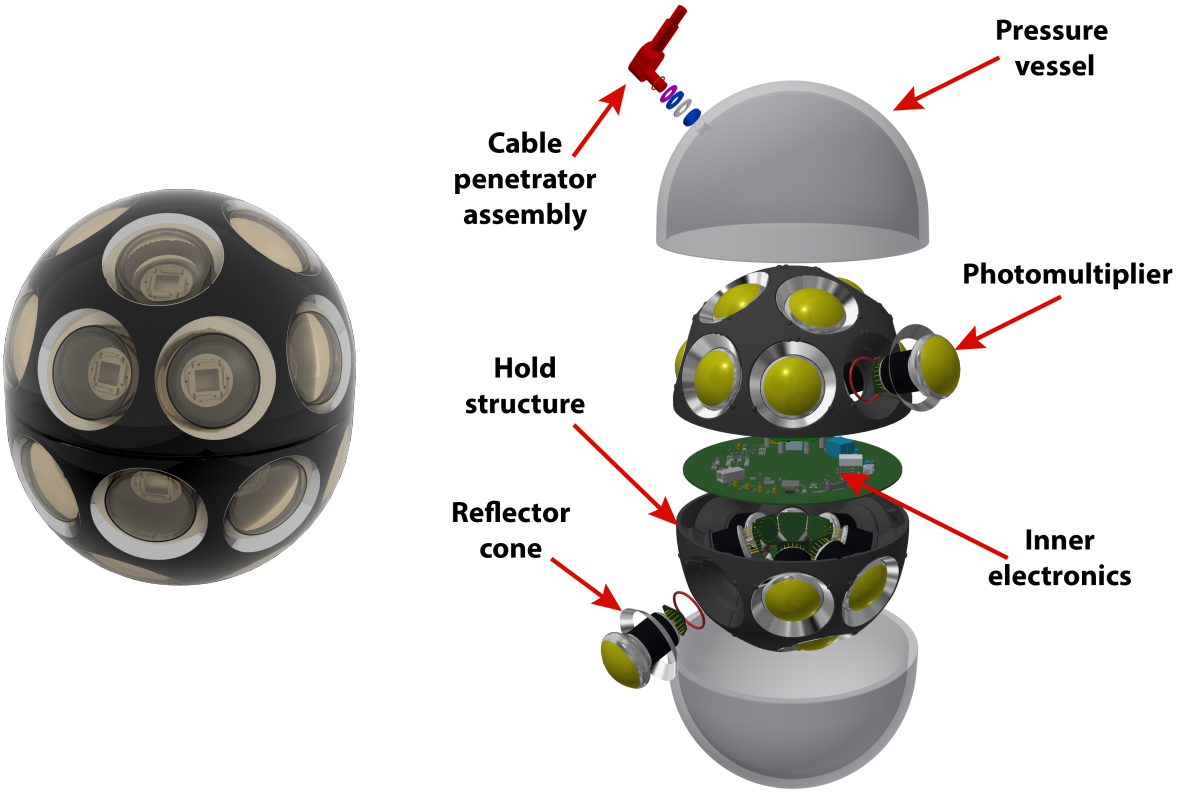

Figure 3.4: Left: Artist impression of the multi-PMT digital optical module (mDOM). **Right:** Exploded view of the mDOM, with its different components. Figures courtesy of IceCube group Münster.

Fig. 3.5 shows the values of the quantum efficiency (QE) of a PMT as a function of the wavelength of the photons. The QE gives the probability at which an incident photon is converted into an electron in a photosensitive device. Since the production of photons by Cherenkov effect per wavelength interval is proportional to λ^{-2}, the desired QE curves for PMTs in Cherenkov based detectors show higher values for shorter wavelengths. The QE is a very important feature to take into account, since the read signal of the module can change significantly from one PMT to another if their QE curves are different.

The use of mDOMs in the construction of IceCube-Gen2 can open new possibilities for the study of low energetic neutrinos and, more precisely, neutrinos coming from supernovae. This is because, in addition to use the local coincidences to suppress backgrounds, they can also be used for the recognition of events. As it was shown in previous chapters, SN

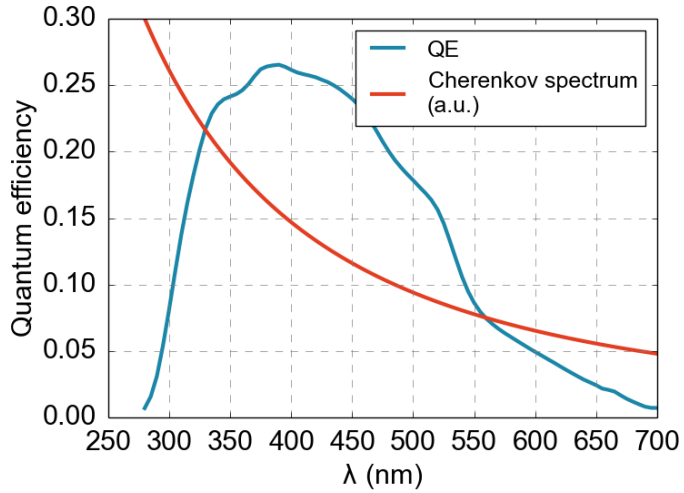

Figure 3.5: Values of the quantum efficiency for the *Hamamatsu R12199* PMT, model which will likely be chosen for the first mDOM prototype. Over the curve, it has also been depicted the Cherenkov spectrum using Eq. 3.3 in arbitrary units.

neutrino energy range is about tens of MeV, making electrons and positrons emitted from their interactions to travel about $\sim$10 cm in the ice before losing all their energy and stop [12]. Coincident rates between different modules are very low for these events, but local coincidences are much more likely. The use of one single module to look for coincidences allows to treat every module as a single small detector, therefore IceCube-Gen2 could work as a combination of individual detectors for the case of SN neutrinos. If this is proven, a single mDOM will be able to do event-by-event detection of low energetic neutrinos even when just few events have been detected, like it occurs for extra-galactic SNe, by requesting for an appropriate local trigger condition in order to avoid background rates. This possibility will be explored later in chapter 7.

4 Geant4 simulation

In order to study the sensitivity of the mDOM to SN neutrinos, simulations are necessary. These simulations describe the interactions of the SN neutrino fluxes going through the volume where the module is deployed, as well as the response of the mDOM to detect them. In this chapter, a mDOM simulation will be adapted to the case of detection of SN neutrinos, where the fluxes will be implemented using the SN explosion model described in section 2.3.

The simulation of the mDOM used here is written in Geant4[1]. Geant4 is a C++ based toolkit developed at CERN[2] with the goal to simulate the passing of particles through matter using Monte-Carlo methods. The code is freely available under the GPL license and continuously being upgraded [48]. Geant4 is currently being used in a broad variety of scientific fields, from high energy physics over nuclear and accelerator physics to medical applications or space radiation shielding optimization [49].

Geant4 covers the interaction of particles with the materials that are defined in the geometry, the production of secondary particles, the extraction of the result and the visualization of the geometries and tracks of the particles. It provides an abundant set of physics models to handle the interactions between particle and matter across a very wide range of energy. It includes physical properties and interactions going from electromagnetic to complex baryonic interaction processes. These processes have been widely validated, proving that the results from simulations agree with experiments [48].

4.1 mDOM simulation

The mDOM simulation was initially written in the framework of two PhD thesis [38, 50] in order to test the optical properties of the module. The geometry of the mDOM in the simulation can be seen in Fig. 4.1. The simulation includes all the external parts of the module: the pressure glass vessel, the PMTs, the reflector cones and the optical gel. The PMT is modeled as a solid glass containing the photocathode. Each component is composed of its own material and properties. Different types for each component are still being tested, thus the simulation allows to choose between them. Since the scope of this work is not to test them, the components used in the simulations made here are the ones most likely to be used in the first mDOM prototype. These components are Vitrovex glass, Wacker SilGel 612 A/B gel and Alemco V95 reflector cones. The holding structure of the mDOM is so far simulated as a total absorbing massive object, where the inner part of the module containing the electronics is not included since it has not been necessary for this or other studies yet. In the simulation, when a photon reaches the surface of the photocathode, the photon is removed and saved as a hit on that PMT. There is also the possibility to check the quantum efficiency (QE), so that the hit would be counted according to the quantum efficiency by using Monte-Carlo method.

[1] GEometry ANd Tracking.
[2] Conseil Européen pour la Recherche Nucléaire, Switzerland.

Table 4.1: Description of the physics list used in the mDOM simulation. First column shows the considered particle. Second column gives the Geant4 included processes. Third column offers a brief description of each process. Cherenkov effect is defined in the proper mediums when it has been excited by a charged particle energetic enough.

Particle	Processes included	Description
Optical photon	G4OpAbsorption	Absorption of optical photons in materials
	G4OpBoundaryProcess	Boundary interactions when photons changes medium
	G4OpMieHG	Mie scattering of photons
Gamma	G4LivermoreGammaConversionModel	Gamma conversion into an electron- positron pair
	G4LivermoreComptonModel	Compton effect for gammas
	G4LivermorePhotoElectricModel	Photoelectric effect for gammas
Electron	G4eMultipleScattering	Scattering of electrons in medium
	G4LivermoreIonisationModel	Ionisation of the medium by electrons
	G4eBremsstrahlung	Bremsstrahlung of electrons
Positron	G4eMultipleScattering	Scattering of positrons in medium
	G4eIonisation	Ionisation of the medium by positrons
	G4eBremsstrahlung	Bremsstrahlung of positrons
	G4eplusAnnihilation	Annihilation of positrons with electrons of medium

The result of propagating an electron of 10 MeV in ice with the Geant4 simulation can be seen in Fig. 4.1 right. As the electron travels, it emits Cherenkov photons, depicted as orange lines. It can also be seen how the electron changes its path through the ice because of scatterings.

In Tab. 4.1, the *physicslist* used in Geant4 for the simulations in this work are described. The physicslist contains the particles and processes that are included in the simulation. Other particles or processes were not directly used in the simulations of this work, therefore they have not been not included. Notice that there is no neutrino physics included. Neutrino interactions are poorly described in Geant4 [51], which is the reason they are not included here. The way SN neutrino interactions are implemented in the simulation

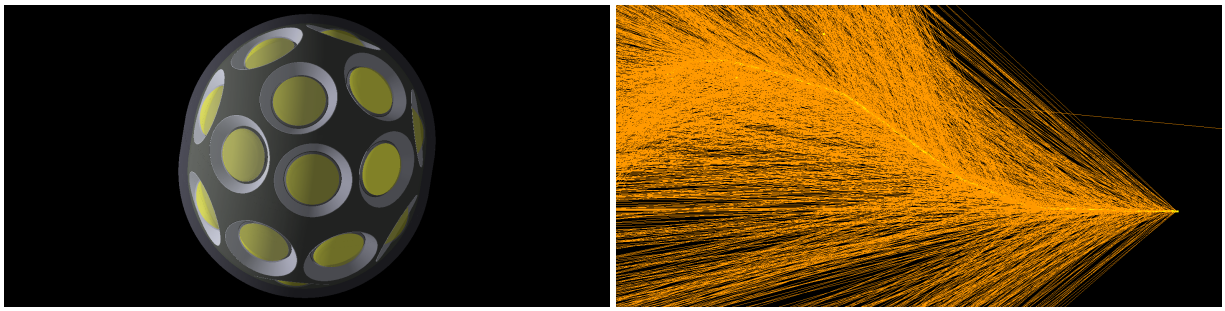

Figure 4.1: Left: Geometry of the mDOM in the Geant4 simulation. **Right:** Result of the simulation of an electron of 10 MeV in ice in the mDOM simulation. The Cherenkov photons production and scattering processes can be observed.

is described in section 4.3.

4.2 South Pole ice properties in the simulation

In order to have a realistic propagation of the particles through the medium, it is necessary to implement realistic properties to the ice where the module is going to be deployed. For South Pole depths deeper than 1300 meters, the propagation of the photons through the ice changes with the depth because of the vertical variation in the concentration of dust impurities. This variation is due climatological changes or catastrophic events occurred in the history of the Earth [52]. IceCube extends from around 1450 to 2450 meters deep [7], and in this range the ice properties change considerably.

In the simulations made in this work, only one mDOM is simulated and not the whole IceCube-Gen2 extension. Since the simulated ice volumes will be usually small, it is assume that the ice properties do not change inside it. However, the depth at which the simulated mDOM is deployed must be chosen in order to use the appropriate ice properties. The most important properties for the propagation of photons through the ice are scattering, absorption and refraction, of which scattering and absorption change with the depth. Because of the size of the dust particles, Mie scattering prevails over Rayleigh scattering for photons propagating through the South Pole ice [52, 53]. Scattering and absorption lengths have been parametrized in [52] and [54] as a function of the photons wavelength and the depth. The effective Mie scattering coefficient is given by [54]:

$$b(\lambda) = \frac{b_e(\lambda)}{1 - \langle \cos\theta \rangle} = b_e(400) \left(\frac{\lambda}{400} \right)^{-\alpha}, \tag{4.1}$$

where $1/b(\lambda)$ determines the average distance between successive scatters and θ is the scatter angle with respect to the incident direction. The formula has been parametrised using $b_e(400)$, value of the effective scattering coefficient at the center of IceCube as a function of the depth for photons of 400 nm. The parameters α and $\langle \cos\theta \rangle$ were determined in [54] to be $\alpha = 0.90 \pm 0.03$ and $\langle \cos\theta \rangle = 0.9$. In these formulas it is assumed that the ice properties only change with depth, while they are homogeneous among all other

directions. Absorption coefficient is parametrised as [54]:

$$a(\lambda) = a_{\text{dust}}(400)\left(\frac{\lambda}{400}\right)^{-k} + Ae^{-B/\lambda} \cdot (1 + 0.01\delta\tau), \tag{4.2}$$

where $1/a(\lambda)$ is the average distance that the photon would travel before it is absorbed in the ice and $\delta\tau$ is a temperature parameter [55]. The formula of the absorption coefficient has also been parametrised with $a_{\text{dust}}(400)$, value of the absorption parameter for photon's wavelength of 400 nm. The remaining parameters have been fitted in [52] to $A = (6954 \pm 973)\,\text{m}^{-1}$, $B = (6618 \pm 71)\,\text{nm}$ and $\kappa = 1.08 \pm 0.01$.

In Fig. 4.2, the average Mie scattering length and absorption length for different wavelengths as a function of depth are plotted, using the equations 4.1 and 4.2 together with the data of $b_e(400)$ and $a_{\text{dust}}(400)$ from [52]. It can be seen that the variation of the properties with the depth is significant, while both parameters follow a similar behaviour as they are both affected by the number of dust particles in the ice. For longer wavelengths, the probability that the photons are absorbed is higher, contrary of the probability of suffering Mie scattering, which is more likely for shorter wavelengths. The calculations in this work will be done in the *clean* part of the ice unless the contrary is specified, where the chosen depth is 2278.2 meters. At this depth, $1/a(400) = 227.2\,\text{m}$ and $1/b_e(400) = 76.8\,\text{m}$.

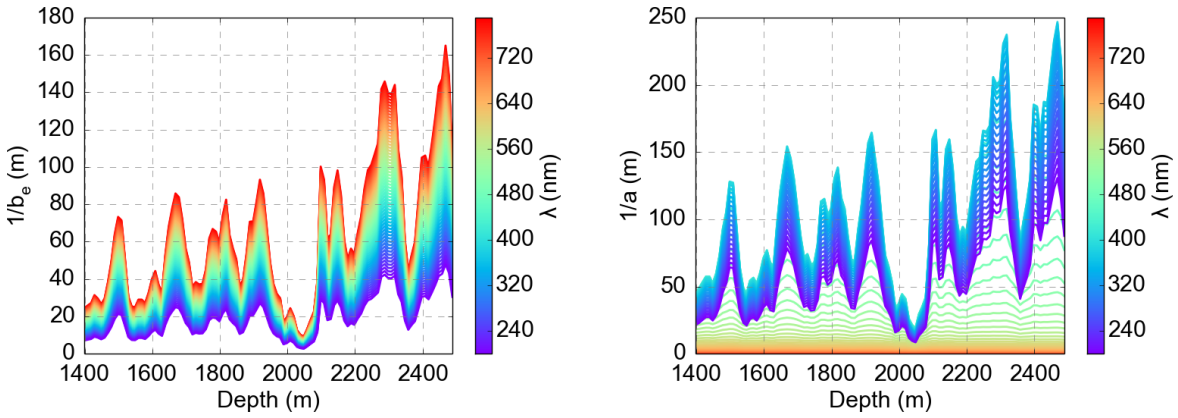

Figure 4.2: Average Mie scattering (**left**) and absorption (**right**) lengths for photons with different wavelengths propagating through South Pole ice as a function of the depth.

To simulate the Mie scattering angle of the photons, Geant4 uses the Henyey-Greensterin approximation [51, 56]. The Mie scattering angle distribution in South Pole ice has been calculated in [54]. Fig. 4.3 shows how it has been implemented in the mDOM simulation, according with the results of [54]. It can be observed that the Mie scattering distribution is peaked for $\cos\theta \to 1$, therefore photons are very likely to conserve the direction after the scattering. This is an important feature that enables IceCube to reconstruct directions with good resolution.

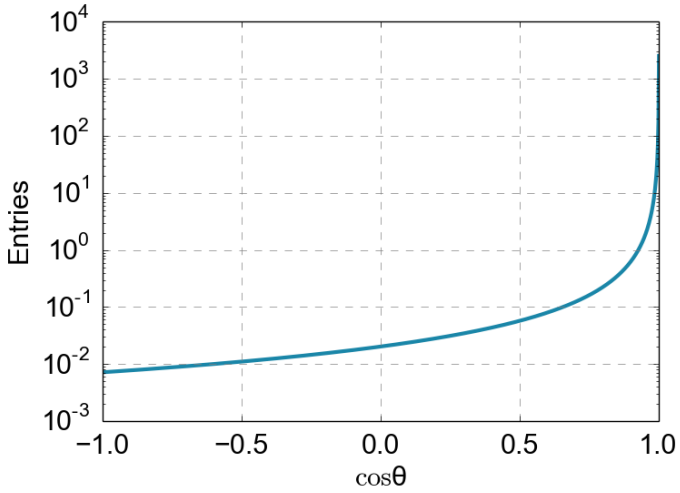

Figure 4.3: Mie scattering distribution implemented in the ice of the mDOM's simulation as a function of the cosinus of the scatter angle θ.

4.3 Simulation of the SN neutrino interactions

Since neutrino interactions are very unlikely, a simulation of neutrinos passing through ice and looking for their interactions would be highly inefficient. Instead, the resulting particles of the interactions from SN neutrinos in ice will be directly simulated. Therefore, when simulating IBD a positron will be generated in the ice, while it will be an electron in the case of ENEES. It is necessary to generate them in a coherent way in order to reproduce fairly that they have been produced from a neutrino coming from a SN burst which interacted in the South Pole ice. In order to do this, an algorithm for generating events has been implemented in the mDOM simulation. The algorithm works in the same way for both positron from IBD or electron from ENEES. The different steps that the algorithm takes to generate them are shortly described below:

1. The fluxes of neutrinos and antineutrinos coming from a supernova explosion are provided to the simulation by the Eq. 2.13 and the data described in section 2.3.1. Using the fluxes distribution, the algorithm normalises the function and chooses a time of the burst according to the height of the distribution at Y axis. This means, a value from the x-axis t is more likely to be chosen when the value of $f(t)$ is higher. Once the time of the burst is chosen, the mean energy of the neutrino/antineutrino can be obtained from the data of Fig. 2.10.

2. The energy distribution of the neutrino/antineutrino is built using the Eq. 2.16 with the value of mean energy obtained before. From this distribution, the algorithm chooses a single value of the $\nu_e/\overline{\nu}_e$ energy according to the height of the distribution at Y axis. This is the energy of the incoming $\nu_e/\overline{\nu}_e$ that produces the particle which is generated in the simulation.

3. The direction where the SN neutrinos and antineutrinos are coming from must be chosen. In fact, this would be the direction of the simulated SN. With the energy of $\nu_e/\overline{\nu}_e$, the angular cross section can be built from Eq. 2.7 and 2.11. From there, the algorithm chooses a value for $\cos\theta$ according to the values on the Y axis. This will

be the azimuthal angle of the emitted particle with respect to the direction of the SN, while the zenith angle is assumed to be isotropic and is chosen randomly.

4. From the energy of $\nu_e/\overline{\nu}_e$ and the angle θ obtained before, the final energy of the emitted electron/positron is calculated using Eq. 2.12 and 2.8. The particle is generated at a random position in the ice volume and propagated with its corresponding energy and direction calculated before.

5. Up to this point, the simulation generates a chosen number of events according to the SN neutrino burst spectra. Depending on the scope of the simulation itself, it might be necessary to weigh the events according to the probability that their interaction really occur in the simulated volume. The events should also be weighed according with the fluxes which travel through the simulated volume. For these cases, two different weights are defined.

   The first one, different for each event, takes into account that the chosen neutrino or antineutrino produces the desired interaction when it travels through the simulated volume. This event weight w_e is given by:

$$\omega_e = \sigma \cdot N_{\text{target}} \cdot r_{\text{path}} \tag{4.3}$$

   where σ is the total cross section of the interaction, N_{target} is the number of possible targets for the interaction in the ice per cubic meter and r_{path} is the length of the path that the neutrino or antineutrino travels through the simulated ice. Since σ depends on the energy of the incoming neutrino or antineutrino, each event weight will have a different value.

   The second weight considers the number of neutrinos or antineutrinos that travels through the simulated volume from a SN burst. If the SN is simulated to be at a certain distance, this weight will have a general fix value for neutrinos and a different one for antineutrinos. This general weight W_T is defined as:

$$W_T = \frac{N_{\text{mDOM}}}{N_{\text{generated}}} \cdot 4\pi r^2 \cdot \int_{\text{t=0 s}}^{\text{t=10 s}} \phi(t)dt = \frac{N_{\text{mDOM}}}{N_{\text{generated}}} \cdot \frac{r^2}{d^2} \cdot \int_{\text{t=0 s}}^{\text{t=10 s}} \frac{L(t)}{\langle E(t) \rangle} dt \tag{4.4}$$

   where $N_{\text{generated}}$ stands for the number of events that have been simulated, d is the distance to the SN and r is the radius of the surface of the simulated volume facing the neutrinos/antineutrinos direction. N_{mDOM} stands for the number of mDOMs, and it allows to scale the results with the detection in more than one single module, as e.g. a whole IceCube-Gen2 with mDOMs. The integral goes from 0 to 10 seconds because to cover the usual neutrino burst duration.

By using this particle generator, the interactions of SN neutrinos via IBD and ENEES can be reproduced. Some results of the generation are depicted in the next figures for the case of the heavy SN with LS220 as EoS. Similar results are expected for the rest of models descrived in section 2.3. In Fig. 4.4 the input fluxes are compared with the time from the burst selected by the simulation. It can be seen that the chosen times by the algorithm reproduce the flux distribution, which shows that the particle generator is working as desired.

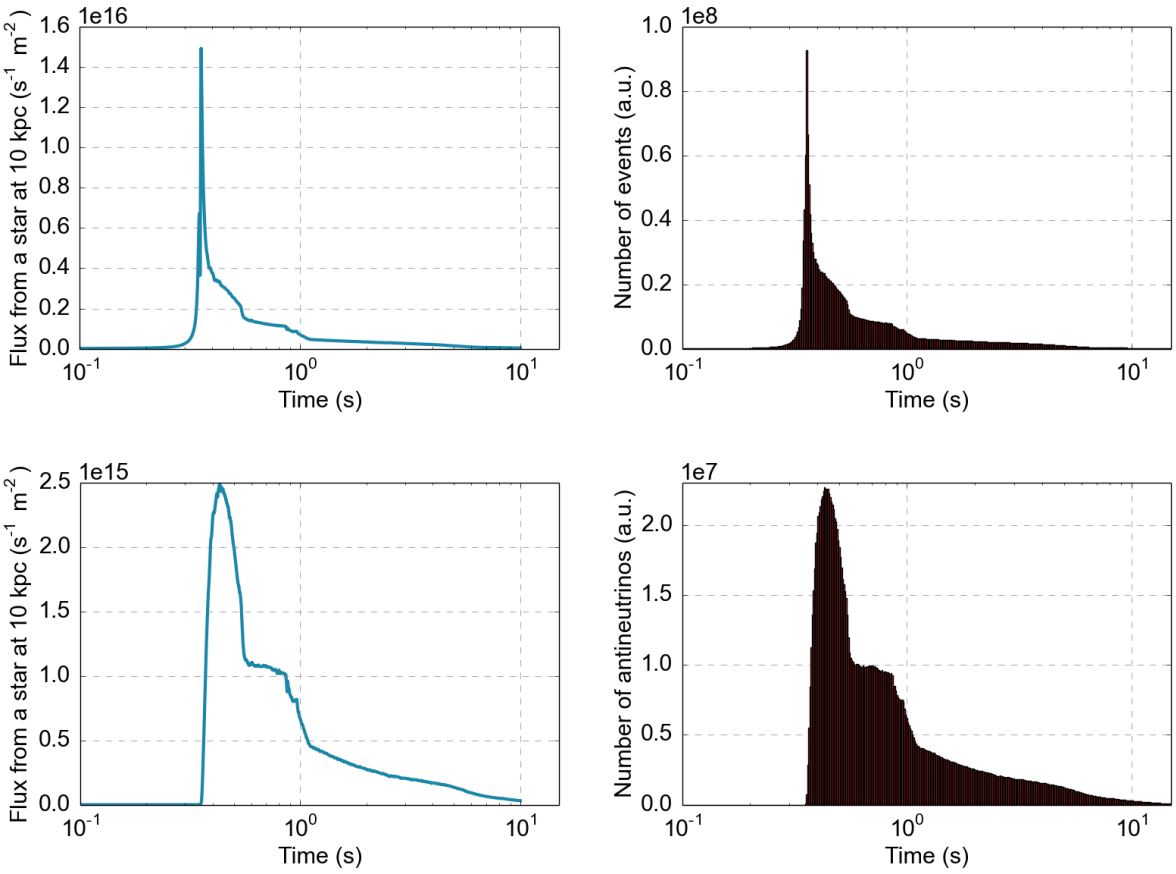

Figure 4.4: Fluxes from a SN at 10 kpc (**left figures**) and the result of the time of the burst selected by the particle generator with 20 millions of generated events (**right figures**). The upper plots show the result for ENEES, while the IBD is shown in the lower plots. The height of each bin has been divided by its width in order to use logarithmic scale to the x-axis.

Fig. 4.5 shows the results of the incident and emitted particle's energy in the simulation, for ENEES in the left and for IBD in the right. In the case of IBD, Fig. 4.5 shows the emitted positron carries most of the energy of the antineutrino, while in the case of ENEES the differences between the energy values of incident and emitted particles are bigger. Because particles with higher energy produce more Cherenkov photons (see Eq. 3.2), positrons from IBD will be easier to detect than electrons from ENEES.

In Fig. 4.6 the results of the simulation for the cosine of the angle between the emitted particle and the incident particle directions are shown. It can be seen that in the case of ENEES the direction of the incident particle is well conserved, as expected, since the distribution has its maximum for $\cos\theta \to 1$. In the case of IBD it was shown before that the angular cross section depends on the energy. For very high antineutrino energies the angular cross section shows that the forward direction was prefered while for energies below 15 MeV the angular cross section was slightly higher for negative values of $\cos\theta$ (see Fig. 2.6 and 2.7). Fig. 4.5 shows that in the case of IBD there will be more antineutrinos with energies below 15 MeV than higher. Once all the generated events from all possible energies are combined, the result is an isotropic emission of positron from IBD, as seen

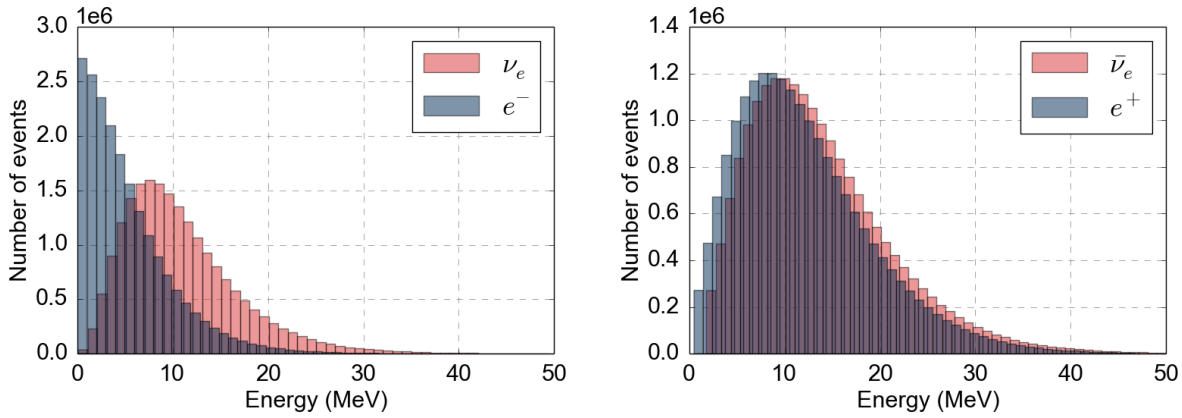

Figure 4.5: Results of the incident and emitted particle's energy in the simulation with 20 millions generated events from a SN burst, **left:** for ENEES and **right** for IBD.

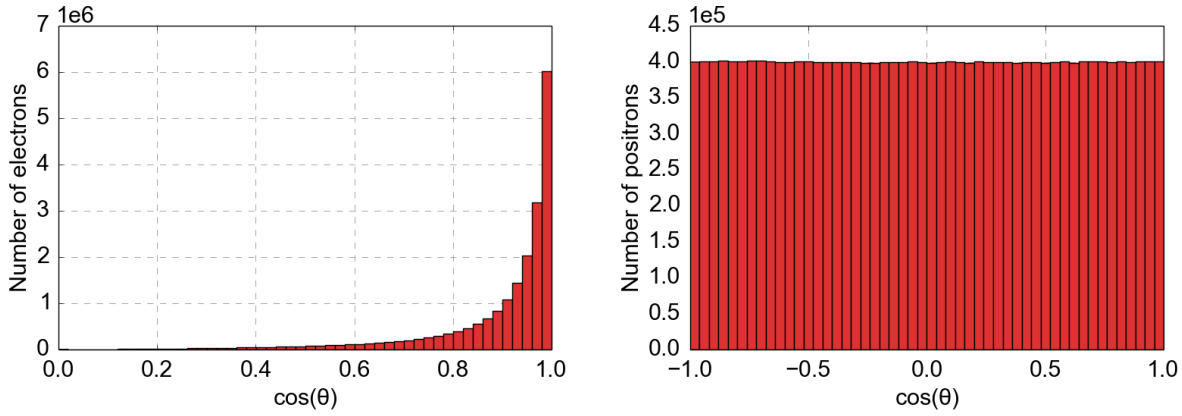

Figure 4.6: Results for the cosine of the angle between the emitted and incident particle's direction in the simulation with 20 millions generated events from a SN burst, **left** for ENEES and **right** for IBD.

in Fig. 4.6 right.

Up to now, these results have been obtained without taking into account the weights. The results for the angle of the incident particle considering the individual weights from 4.3 are presented in Fig. 4.7. Once the detected events are weighed, events produced by neutrinos or antineutrinos with higher energies will also have higher ω_e, since the value of the total cross sections is bigger. This results in a higher abundance and thus detection of positrons that conserve the direction of the incident antineutrino, as it can be seen in Fig. 4.7. This also enhances the conservation of the direction in the case of ENEES. In Fig. 4.6 left it is obtained that about 69% of the events have values of $\cos\theta > 0.9$, which corresponds to a deviation of less than 6° from the direction of the incident neutrino, while from Fig. 4.7 left, where the events have been weighed, about 74% of them would have values of $\cos\theta > 0.9$.

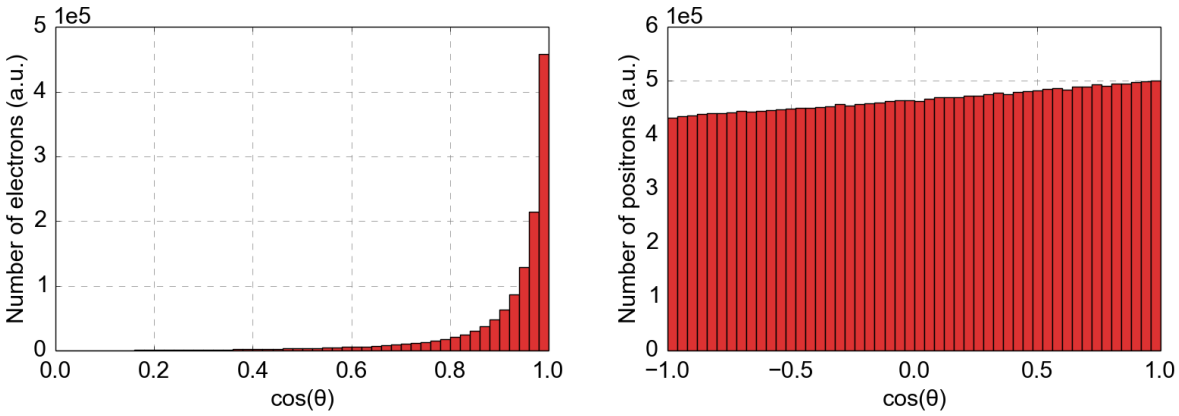

Figure 4.7: Results for the cosine of the angle between the emitted and incident particle's direction in the simulation with 20 millions generated events from a SN burst, after weighing the results by their individual weights with Eq. 4.3, **left** for ENEES and **right** for IBD.

5 Effective volume for SN neutrinos

The effective volume,

$$V_{\text{eff}} = \frac{N_{\text{det}}}{N_{\text{total}}} \cdot V_{\text{gun}}, \tag{5.1}$$

quantifies the volume in which a number of events N_{total} needs to be produced inside a volume V_{gun} in order to detect N_{det}. In this case, V_{eff} will be the effective volume for the detection of MeV SN neutrinos. The effective volume is an important feature in order to build an efficient simulation, since it provides the volume where the mDOM is sensitive to the detection of the events. V_{eff} can also be seen as the volume in which any produced event would be detected. This is an assumption because the direction of the generated event is also relevant, since an event generated inside the effective volume but with an opposite direction to the module would probably not be detected. The effective volume does not mean that an interaction outside it would not be detected.

5.1 The effective volume of the mDOM

The effective volume of the mDOM deployed in South Pole ice is expected to scale down with the absorption length of photons in the medium [57]. Since the optical properties of the South Pole ice change with the depth, the effective volume for the mDOM depends on the depth at which it is deployed. From the simulation, the effective volume can be obtained by generating events inside a gun volume V_{gun} and quantifying the ratio $N_{\text{det}}/N_{\text{total}}$. If the same number of events is being generated randomly distributed along the whole gun volume, the number of detected events would decrease with increasing V_{gun} because of the loses by the absorption. As V_{gun} increases, the ratio $N_{\text{det}}/N_{\text{total}}$ decreases until an asymptotic value of V_{eff} is reached, the effective volume.

The effective volume will be first obtained in a scenario with clean ice and high value for the energy of the produced particle. The chosen depth for the ice parameter is 2278.2 m, and the generated particles are electrons of 25 MeV. The results would not change if the chosen particle is a positron, as both particles have the same absolute value for their charge and thus their production of Cherenkov photons are the same.

Because of the absorption parameters shown in last section, photons with longer wavelengths produced far from the mDOM are likely absorbed. This, together with the Cherenkov spectrum, results in the detection of photons whose wavelengths are likely between 300 and 450 nm. Fig. 3.5 shows that for wavelengths between 300 and 450 nm the QE is around or above 0.20. Therefore, the quantum efficiency in these simulations is applied afterwards, scaling the results by a factor of 0.20. Thus, V_{eff} is calculated as:

$$V_{\text{eff}} = \frac{n_{\text{det}}}{N_{\text{total}}} \cdot V_{\text{gun}}, \tag{5.2}$$

where $n_{\text{det}} = QE \cdot N_{\text{det}}$. This allows to get better statistics within less simulations, necessary because the computational time of each simulation increases dramatically with the size of the generation volume.

It is also assumed that the mDOM provides an isotropic sensitivity in all directions, which is a good approximation since it is almost spherical. With this assumption, the electrons can be generated in only one direction. It also allows to approximate both the gun volume where particles are being generated and the effective volume as spheres with the mDOM in their center. The effective volume is therefore calculated and depicted in Fig. 5.1, together with its effective radius.

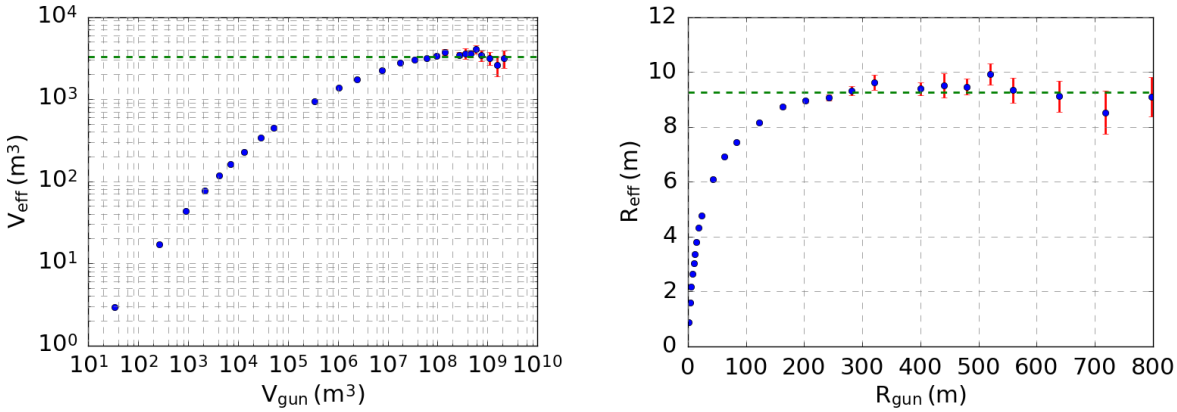

Figure 5.1: Effective volume (**left**) and effective radius (**right**) as a function of the gun volume and radius, respectively, where the events have been generated.

Fig. 5.1 shows how increasing the size of the world generation also increases the effective volume up to a certain value where the effective volume stabilizes. This value is $V_{\text{eff}} = (3316 \pm 81)\,\text{m}^3$ of a sphere with radius $R_{\text{eff}} = (9.27 \pm 0.08)\,\text{m}$. In order to calculate the uncertainties in the results, it has been necessary to separate $N_{\text{total}} = N_{\text{det}} + N_{\text{n.det}}$, where $N_{\text{n.det}}$ is the number of events that have not been detected, assuming $\sigma(N_{\text{x}}) = \sqrt{N_{\text{x}}}$ for statistical uncertainties. With n_{det} as defined before, $n_{\text{n.det}} = N_{\text{total}} - n_{\text{det}} = N_{\text{det}} + N_{\text{n.det}} - QE \cdot N_{\text{det}}$. This results to an uncertainty in the effective volume that can be calculated as:

$$\sigma(V_{\text{eff}}) = V_{\text{gun}} \cdot \sqrt{\left(\frac{n_{\text{n.det}}}{(n_{\text{det}} + n_{\text{n.det}})^2}\right)^2 \cdot \sigma^2(n_{\text{det}}) + \left(\frac{n_{\text{det}}}{(n_{\text{det}} + n_{\text{n.det}})^2}\right)^2 \cdot \sigma^2(n_{\text{n.det}})}, \tag{5.3}$$

where $\sigma(n_{\text{det}}) = QE \cdot \sqrt{N_{\text{det}}}$ and $\sigma(n_{\text{n.det}}) = \sqrt{N_{\text{det}} + N_{\text{n.det}} - \sigma^2(n_{\text{det}})}$.

The same method can be used to obtain the effective volume for different conditions. There are two main conditions where the effective volume is of interest. The first one

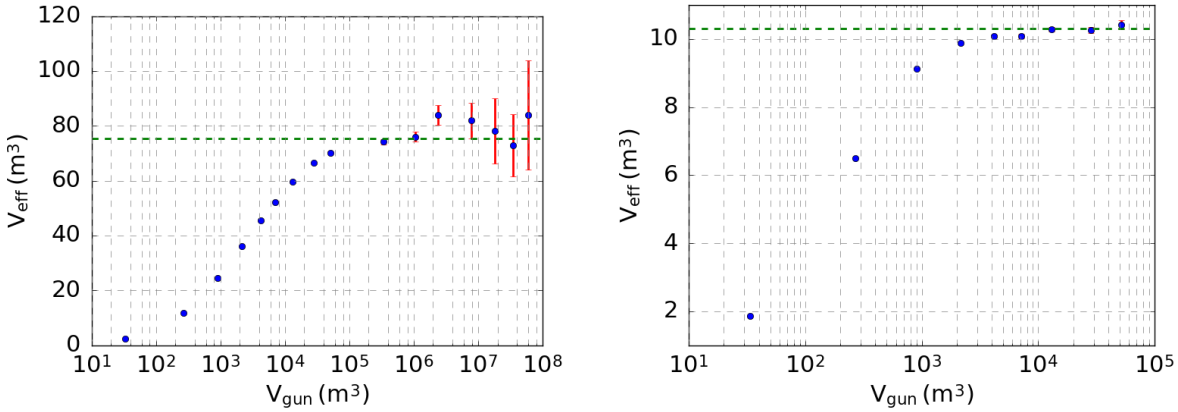

Figure 5.2: V_{eff} for events that give a coincident signal (**left**) and for events which produce 5 or more hits (**right**).

Table 5.1: R_{eff}, V_{eff} and M_{eff} for different conditions. Volumes have been approximated to spheres with the mDOM in their center. Only statistical errors have been included.

Condition	R_{eff} (m)	V_{eff} (m^3)	M_{eff} (ton)
At least 1 hit	9.27 ± 0.08	3316 ± 81	3056 ± 75
At least 2 different hit PMTs	2.62 ± 0.01	75.4 ± 0.9	69.4 ± 0.8
At least 3 different hit PMTs	1.758 ± 0.002	22.74 ± 0.08	21.0 ± 0.8
At least 4 different hit PMTs	1.374 ± 0.003	10.86 ± 0.06	10.01 ± 0.05
At least 5 hits	1.349 ± 0.003	10.28 ± 0.06	9.47 ± 0.05

is the volume where any SN neutrino interaction would give a coincident signal. This is the case if two or more different PMTs detect the event. The second one is the effective volume at which the mDOM measures a certain number of hits, e.g. when 5 hits from the same event are required. The Eq. 5.2 can be used again, where instead n_{det}, $n_{condition}$ will be used as the number of detected events that satisfied the condition. In Fig. 5.2 the V_{eff} for coincident events is shown, while the right part shows the V_{eff} for events that give 5 or more hits. The results are presented in the table 5.1 together with their corresponding effective masses and with the results for 3 and 4 different hit PMTs, whose figures have not been presented.

In the case of IceCube-Gen2 with mDOMs, the module separation distances are planned to be around one hundred meters. From the results above it can be concluded that it is very unlikely that one single event is detected in more than one module in IceCube-Gen2, since module distances are much larger than the effective radius. It has also been shown that events can give coincidences in the same module if they are produced close enough to it. From these results, it can be claimed that each mDOM in IceCube-Gen2 can be treated as an individual detector looking only for local coincidences for the case of detecting SN neutrinos, since no coincidences between different modules are expected. This result enables the study of the potential of a whole IceCube-Gen2 identifying SN neutrino events by considering only local coincidences, which is done in chapter 7.

5.2 The effective volume of IceCube-Gen2 with mDOMs

From the results of this chapter, the total effective volume of IceCube-Gen2 for the detection of SN neutrinos can be estimated. In the previous section, the effective volume was obtained at a certain depth and energy. It is expected that it changes with the energy of the particles and with the absorption length of the ice [12]. Here, the effective volume is calculated using the same method as before, for different energies of the charged particle as well as for different depths which differ in their absorption length. The results are shown in Fig. 5.3. It can be observed that the effective volume as a function of the energy and of the absorption length are well fitted by lineal regressions.

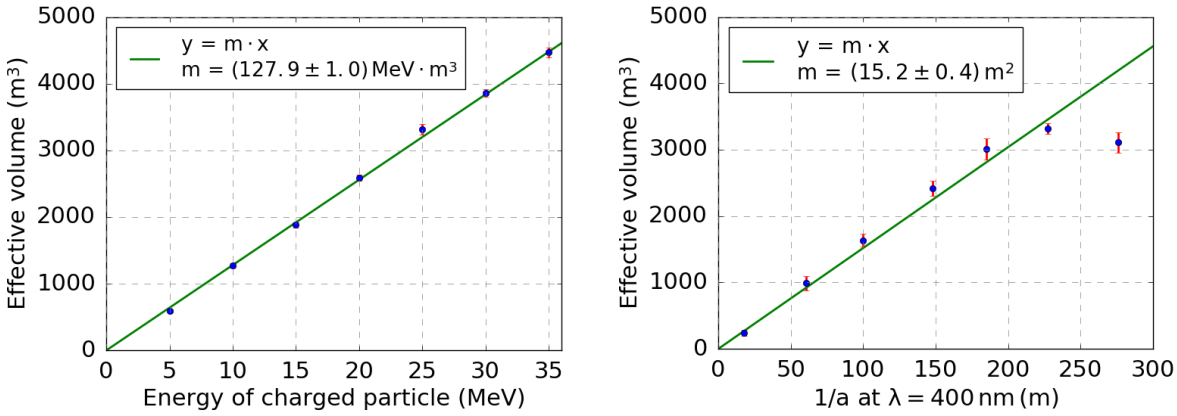

Figure 5.3: Left: effective volume for different energies of the charged particle at 2278.2 meters depth. **Right:** effective volume for different values of the average absorption length of photons with $\lambda = 400\,\text{nm}$, for energy of the charged particle of of 25 MeV.

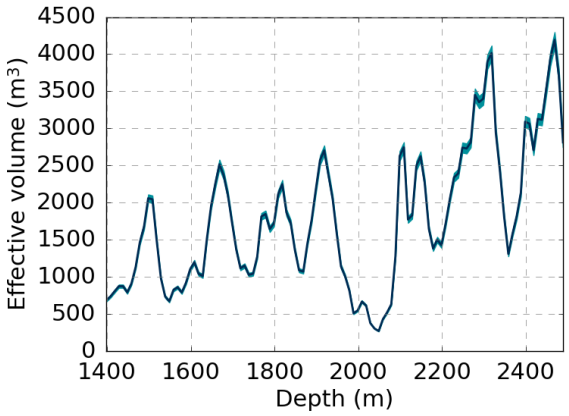

Figure 5.4: Effective volume of the mDOM at any depth, calculated using the lineal fit of Fig. 5.3 right. Shaded region stands for the uncertainty region.

From Fig. 5.3 right, the effective volume can be scaled to any depth using its absorption length. It should be mentioned that the discrepancy of the last point with the rest ones is probably due to a too small generation volume to obtain V_{eff}, therefore it has not been included to calculate the slope of the line. Assuming that IceCube-Gen2 will have 120

strings with 125 modules each one, and those modules will be equally spaced in depth[1], a total effective volume and mass is obtained to be:

$$V_{\text{eff}} = (2.670 \pm 0.007) \times 10^7\,\text{m}^3,\ M_{\text{eff}} = (2.461 \pm 0.007) \times 10^7\,\text{ton}. \tag{5.4}$$

Therefore, IceCube-Gen2 with mDOMs is expected to have a total effective mass of approximately 24.6 Mton for the detection of neutrinos coming from supernovae. From here, the average effective volume of the mDOM in IceCube-Gen2 is $\overline{V}_{\text{eff}} = (1780 \pm 5)\,\text{m}^3$. In [12] the mean effective volume of IceCube DOMs was calculated to be $\overline{V}_{\text{eff}} = (29.0 \pm 3.8)\,\text{m}^3/\text{MeV} \cdot \overline{E}_{e^+}$, which gives a total of $V_{\text{eff}} \approx (3.8 \pm 0.5) \times 10^6\,\text{m}^3$ and $M_{\text{eff}} \approx (3.5 \pm 0.5)$ Mton for energies of 25 MeV, taking into account that 50 modules from DeepCore has about 30% higher QE. The results are summarized in table 5.2. A factor of about 2.6 is predicted as an improvement of the effective volume of the mDOM to the current DOM for the detection of SN neutrinos, while this become a factor 7 when referring from IceCube to IceCube-Gen2 extension equipped with mDOMs. The results are in good agreement with the higher effective area of mDOM, which, for the glass vessel used in the simulation, is larger than the effective area of DOM by a factor of ~ 2.5 [38].

Table 5.2: Comparison between effective volume and mass of IceCube (from [12]) and IceCube-Gen2 with mDOMs. Quantities have been obtained for the detection of particles (e^- or e^+) with an energy of 25 MeV. The results of IceCube-Gen2 are only for the extension, and not for the whole IceCube+IceCube-Gen2. The results obtained here only includes statistical uncertainties, while the results from [12] also includes systematic ones.

	$\overline{V}_{\text{eff}}$ per module (m^3)	Total V_{eff} (m^3)	Total M_{eff} (Mton)
Icecube with DOMs	725 ± 95	$(3.8 \pm 0.5) \times 10^6$	3.5 ± 0.5
IceCube-Gen2 with mDOMs	1780 ± 5	$(2.670 \pm 0.007) \times 10^7$	24.61 ± 0.07

These calculations have been made for IceCube-Gen2 extension alone, but indeed IceCube-Gen2 will operate together with the current IceCube, which would provide a total effective mass of about 28 Mton for the detection of neutrinos coming from core-collapse supernovae.

[1] In IceCube-Gen2, strings will probably cover from 1360 to 2620 meters depth [9], instead the actual strings which covers from ∼1400 to ∼2450 meters depth [39] used in the calculation of this work.

6 Reconstruction of MeV neutrino interactions with mDOM

The reconstruction of an event stands for the information that can be obtained from its signal in the detector. In the case of SN neutrinos, this refers to obtain the information of the produced particles in their interactions, electron or positron. The reconstruction of individual MeV neutrino interactions is not straightforward, since the path of the produced particles in the ice is only about 10 centimeters [12]. From the results of the previous chapter, it can be assumed that a SN neutrino interaction will not be detected in more than one single module in IceCube-Gen2, therefore this chapter will focus in the possibilities of reconstruct SN neutrino events using one single mDOM. The reconstruction of single SN neutrino interactions is not possible in IceCube, since event-by-event detection can not be achieved, something that is different with local coincidences in mDOMs. It is expected that photons which arrive to a module from the same SN neutrino interaction would be detected below the time resolution of the PMTs, being not possible to distinguish which photon arrives sooner or later. The absence of timing information makes harder the reconstruction of these events.

The reconstruction of an event is achieved when the position where the event is generated ((x, y, z) or $(r, \theta_{pos}, \phi_{pos})$), its direction $(\theta_{dir}, \phi_{dir})$ and energy are obtained. The number of detected photons from a single SN neutrino interaction would scale down with the distance of the event, although it would increase with its energy, thus it is not expected that the energy or distance of these events can be reconstructed by using one single mDOM. Therefore, the reconstruction will be focused on getting the position $(\theta_{pos}, \phi_{pos})$ and the direction $(\theta_{dir}, \phi_{dir})$ of the events. Since the QE only plays a proportional factor in the number of detected hits but not in their distribution, it is not included in these simulations.

The direction reconstruction can be an important feature for suppressing background neutrinos, specially those ones coming from The Sun [58]. There is a considerable number of neutrinos from The Sun which reaches Earth. The main neutrino production in The Sun is due the β^+ decay from ^{8}B [59]. The energies of these neutrinos are in the order of tens of MeV, the same order of magnitude as SN neutrino energies [60]. This makes solar neutrinos indistinguishable from SN neutrinos. It was shown before that the most important neutrino interaction in this range of energy is the elastic scattering, whose emitted electron likely conserves the direction of the incident neutrino. Therefore, if the direction of MeV neutrinos can be reconstructed, the background from solar neutrinos can be suppressed by its directionality. This become even more important when detecting few events from extra-galactic SN, where the number of detected events would be very low, making crucial to distinguish them from any other neutrino sources.

6.1 Signal of SN neutrinos at the mDOM

Fig. 6.1 left illustrates how SN neutrino interactions would be detected by the mDOM. The picture has been obtained by the average signal in the PMTs of generating 5 MeV electrons at one meter of the module. The signal in each PMT depends on its orientation to the simulated event, and the result would not change by generating electrons or positrons. In Fig. 6.1 right the frame of reference used in this chapter is depicted. The directions will be expressed using the Geant4 convention, with the vector or the angles coordinates depending on which is more convenient:

$$\begin{aligned} u_x &= -\sin\theta\cos\phi \\ u_y &= -\sin\theta\sin\phi \\ u_z &= -\cos\theta, \end{aligned} \tag{6.1}$$

where θ has been chosen to be always positive for better visualization, going from 0^o to 180^o, while ϕ goes from -180^o to 180^o.

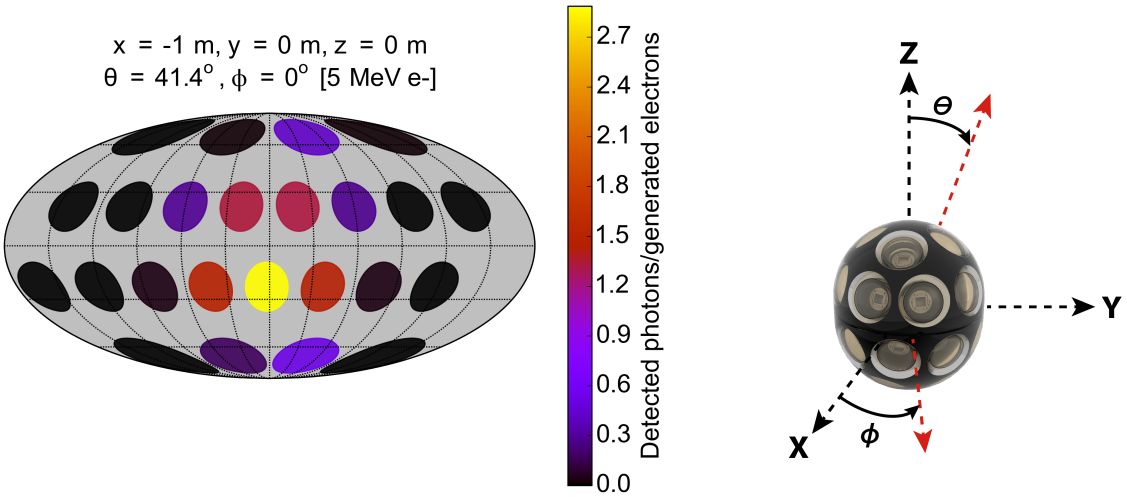

Figure 6.1: Left: representation of how MeV events would be detected at the mDOM in Mollweide projection. Each circle represents a PMT. The ratio of detected photons to generated electrons is presented in colors. The electrons have been generated at 1 meter distance from the mDOM, with 5 MeV of energy and direction $\theta = 41.4^o$, $\phi = 0^o$. **Right:** The frame of reference used in this chapter.

In Fig. 6.2, the Cherenkov angle as a function of energy in ice has been plotted, using Eq. 3.1 and assuming n = 1.33. It can be seen how the Cherenkov angle does not change significantly for energies above 2 MeV, stabilising at about $\theta_c = 41^o$. The lower limit of Cherenkov emission in ice can be seen at $E_{\text{min}} \approx 0.78\,\text{MeV}$, as it was obtained before. Since the particle loses energy while moving forward, the angle of its Cherenkov cone changes considerably when it is about to stop, but for energies above 2 MeV it can be assumed that this angle has a constant value of $\sim 41^o$.

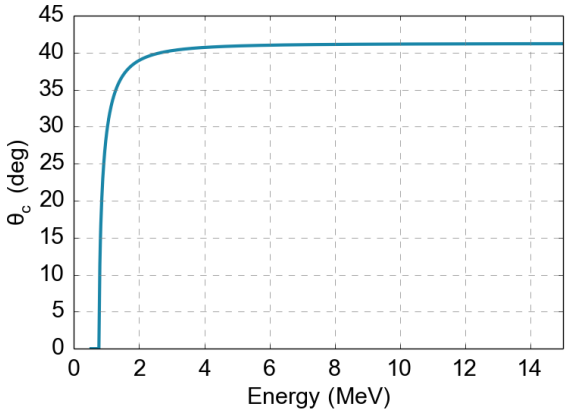

Figure 6.2: Angle of emission of Cherenkov photons from the path of the charged particle as a function of the energy of the electron or positron in Ice.

6.2 Direct reconstruction

In this section, a method of direct reconstruction is studied in order to get information about the position and direction of the electrons created by SN neutrinos. It consists in obtaining the direction of the Cherenkov photons that reached the mDOM and from this deduce the direction of the electron that generated them, using the value of the Cherenkov angle obtained in the previous section. The direction of the photons $\hat{\vec{v}}$ is calculated by weighing the vector, in which each PMT is pointing, by the number of hits registered in that PMT:

$$\vec{V} = -\sum_{i=1}^{24} n_i \times \hat{\vec{r}_i} \tag{6.2}$$

$$\hat{\vec{v}} = \frac{\vec{V}}{\left\|\vec{V}\right\|}, \tag{6.3}$$

where n_i is the number of hits in PMT number i and $\hat{\vec{r}_i}$ is a vector with module = 1 that points from the center of the mDOM to the center of the PMT i. In others words it could be said also that $-\hat{\vec{v}}$ should point directly to the place where the electron has been generated, since the photons came from there, thus the method could be used to get the position of the event. Nevertheless, this method is based on many assumptions. First, all the photons do not come from the same location, since the electron is moving forward while it is producing them. As shown in Fig. 4.1, the electron scatters with the ice and changes its direction while producing photons, which also means that not all the photons come with the same direction. Besides, the way the direction of the PMTs is obtained here would only be true if the photons hit the center of the PMT perpendicularly, which of course is not the general case. Nevertheless, since the vectors are weighed with the number of hits, the vector obtained by Eq. 6.3 should approximately be the average direction of the photons, with better results when more photons have been detected, which is the case for closer or higher energetic events.

To study the possibilities of this method to obtain the vector that points to the position

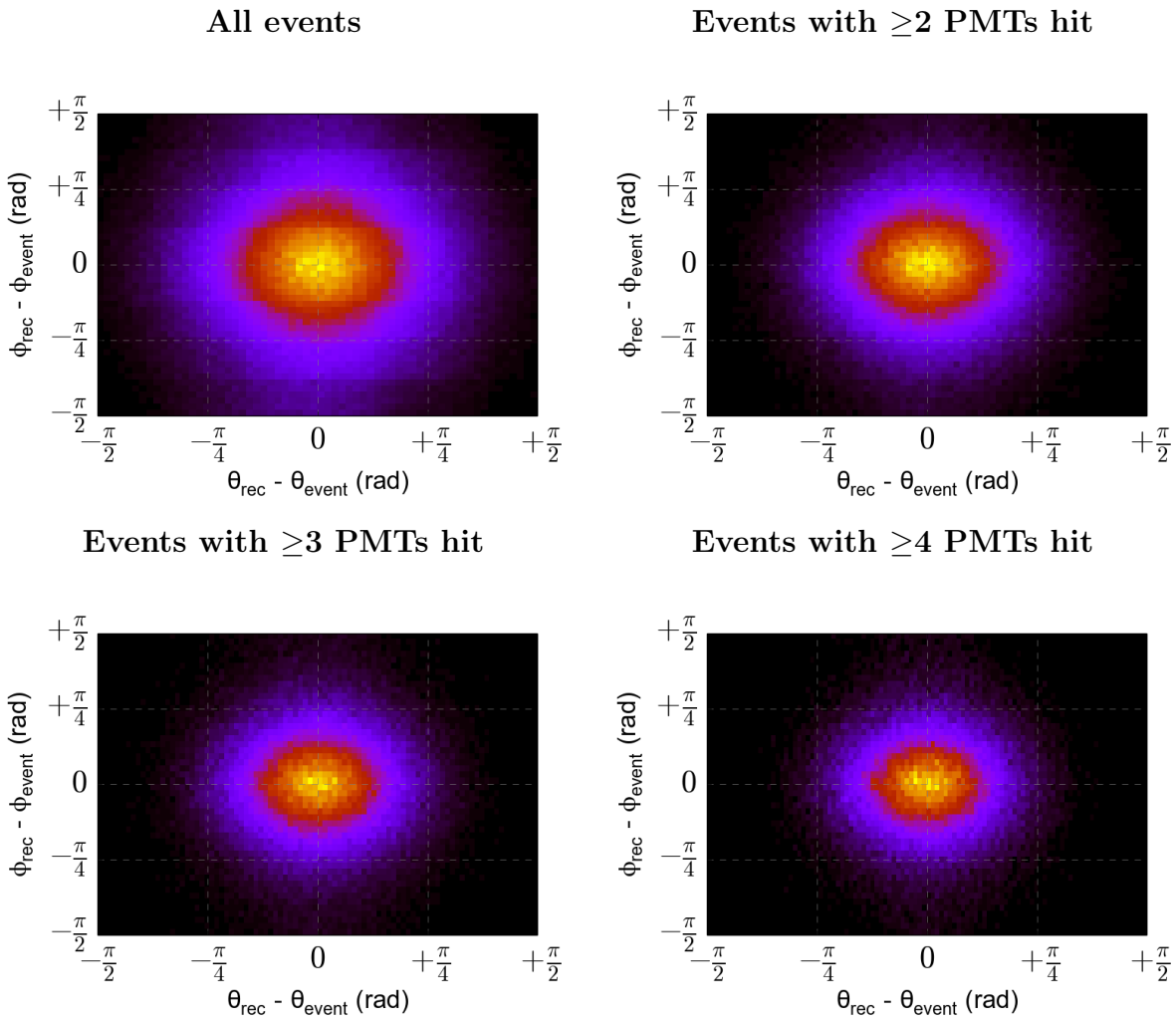

Figure 6.3: Differences between the real vector that points to the position of the event and the vector $-\hat{\vec{v}}$ obtained from the direct reconstruction, depicted in a 2-dimensional histogram where lighter color stands for larger number of events.

of the event, $-\hat{\vec{v}}$ is expressed by two coordinates (θ_{rec}, ϕ_{rec}), as well as the vector which points from the mDOM to the real position of the event (θ_{event}, ϕ_{event}). In Fig. 6.3 it is depicted the result of obtaining $-\hat{\vec{v}}$ for a big number of events produced with random directions in random positions. The differences between the θ and ϕ coordinates of the reconstructed vector and the real vector position have been plotted. The color stands for the number of events in that bin. It can be seen that the distribution is symmetrical with respect to θ and ϕ, result of the almost isotropic sensitivity of the mDOM. In Fig 6.4, the results have been limited to $\theta_{\text{rec}} - \theta_{\text{event}} = 0$ and normalized. It can be seen how the distributions, centered in 0, are narrower when less PMTs are required for the reconstruction. The value of the standard deviation σ for the best Gaussian fit of every curve is shown in the legend. If e.g. 3 PMTs are required, this method would give the direction where the electron has been produced with one σ deviation of about 20^o.

Once $\hat{\vec{v}_i}$ has been obtained, the direction of the electron would form an angle of about 41^o with respect to it. Nevertheless there is an implicit uncertainty in the direction of

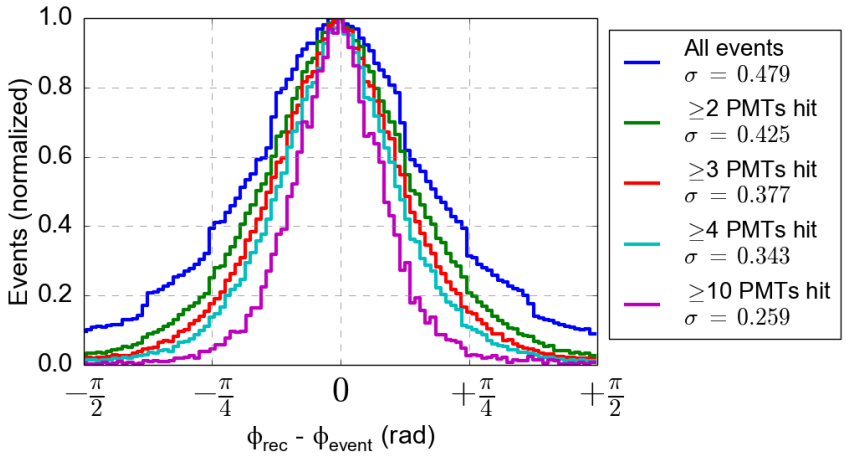

Figure 6.4: Results of the direct reconstruction at $\theta_{\text{rec}} - \theta_{\text{event}} = 0$. The parameter σ stands for the standard deviation of the best Gaussian fit of each curve.

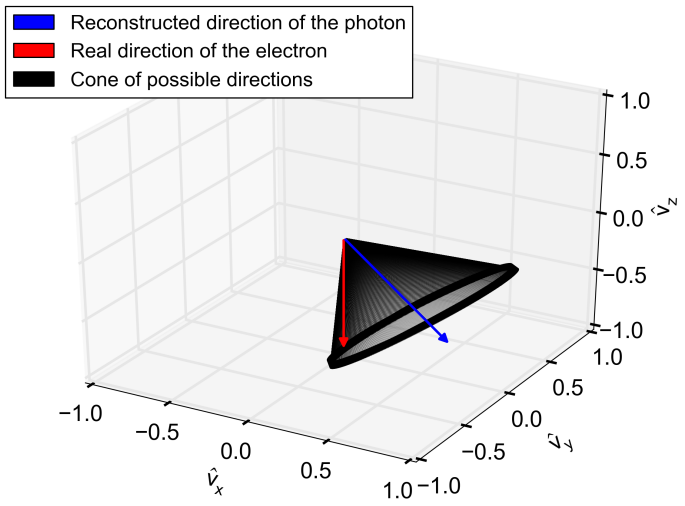

Figure 6.5: Visualization of the direct reconstruction. It is shown the direction of the electron that wants to be reconstructed (red), the reconstructed direction of the photon (blue) and the possible directions for the electron obtained from the reconstruction (black).

the electrons obtained from the direction of the photons. The photons generated by Cherenkov effect form a cone around the electron direction, hence there is a cone of possible directions of the electron which created the detected photons. Fig. 6.5 shows how the direct reconstruction would look like for an example event. It can be seen that the real direction of the electron lies over the cone of possible electron directions, but the uncertainty in the direction of the electron can not be avoided by this method. If an event is measured by two different modules, the resulting cones of possible directions of the electron should intersect themselves at two different points. If the event is detected in three different mDOMs, there should be only one intersection point. Nevertheless, since distances between different modules are big, this is something very unlikely, hence it does not seem like something feasible. A different method of direction reconstruction will be studied in the next section in order to improve the results for the direction reconstruction.

6.3 Reconstruction using the maximum likelihood method

The maximum likelihood (ML) method is an procedure of estimation widely used in reconstructions, as well as in other situations where the maximum of a function is sought.

This method consists of estimating the parameters of a model given by observation looking for the maximum of a likelihood function [61]. In this section, the possibilities of using the maximum likelihood method to reconstruct the direction of SN neutrinos with the mDOM will be studied.

6.3.1 Building the likelihood function

An usual way to write the likelihood function is [61]:

$$\ell = \prod_{i=1}^{N} P(n_i, \mu_i), \tag{6.4}$$

where n_i is the sample of data, μ_i is the sample of the expected values for the data and

$$P(n_i, \mu_i) = \frac{e^{-\mu_i} \mu_i^{n_i}}{n_i!} \tag{6.5}$$

is the Poisson distribution, which gives the probability of obtaining n_i events when the expected number is μ_i. For the scope of this study, the likelihood function will be built as a combination of a Poisson function for each PMT, having therefore a total of 24 Poisson functions. In this case, $n_1, ..., n_{24}$ are the number of hits in every PMT and $\mu_1, ..., \mu_{24}$ are the number of expected hits in every PMT. In order to make the likelihood function easier to be treated mathematically, it is transformed to:

$$\mathcal{L} = -\log \ell = -\sum_{n_i>0} \log P(n_i, \mu_i). \tag{6.6}$$

This transformation is done because there are better algorithms to find the minimum of a function than to find the maximum. The logarithm is included in order to avoid operating with the product operator but with the summation, which is usually simpler. Since the logarithm is a monotonically increasing function, it does not change the position of a maximum or a minimum. Hence, the new likelihood function presents a minimum when the signal at the PMTs get closer to the expected values. This can be used together with the simulation to reconstruct events. Thus, if an MeV neutrino event detected as $\mu_1, ..., \mu_N$ is to be reconstructed, the simulation can be run with electrons with a certain position, direction and energy, obtaining $n_1, ..., n_{24}$, which gives a value for the likelihood function. If this is repeated with different coordinates, different values of the likelihood function are obtained. The minimum of the likelihood function should be obtained when running the simulation at the correct parameters of the event.

The problem of using this reconstruction is that the treatment has to be done in a six-dimensional space $(\mathrm{x}, \mathrm{y}, \mathrm{z}, \theta_{\mathrm{dir}}, \phi_{\mathrm{dir}}, \mathrm{E})$. This is mathematically complex and the computational effort needed to find the minimum of such a function is huge. As discussed before, it can be expected that the distance and energy of the particle only determine the number

of detected photons but not their distribution over the PMTs. Furthermore, the position of the particle might be determined by the direct reconstruction studied in the last section. Hence, as a starting point to the study of the likelihood function, it is assumed that the position and the energy of the particle to reconstruct are known. Therefore, the likelihood space is limited to a two-dimensional space of the directionality of the event: $\mathcal{L}(\mathrm{x}, \mathrm{y}, \mathrm{z}, \theta_{\mathrm{dir}}, \phi_{\mathrm{dir}}, \mathrm{E}) \rightarrow \mathcal{L}(\theta_{\mathrm{dir}}, \phi_{\mathrm{dir}})$.

As an example, the likelihood function of an electron which has been generated by a SN neutrino at the position $\mathrm{x} = 1\,\mathrm{m}$, $\mathrm{y} = -1\,\mathrm{m}$ and $\mathrm{z} = 0.2\,\mathrm{m}$, with 5 MeV and with a direction $\theta = 90^{\mathrm{o}}$ and $\phi = 0^{\mathrm{o}}$ is obtained. This example event has been simulated, giving the signal shown in the Fig. 6.6 left, with hits in a total of five PMTs. The hits are located in the same region of the mDOM, except one of them which probably comes after some scatter of the electron or the photon. Because of the existence of these deflected hits, it is possible that the directionality reconstruction might not point to the correct direction in cases with many scatterings. The simulation is run generating 10000 electrons every 5 degrees in θ and ϕ, and μ_i is divided by the number of electrons that have been generated. The result is presented in the right side of Fig. 6.6. This and the rest of likelihood functions plotted in this chapter are depicted in Mollweide projection, where parallels and meridians lines have been depicted every 30^{o}.

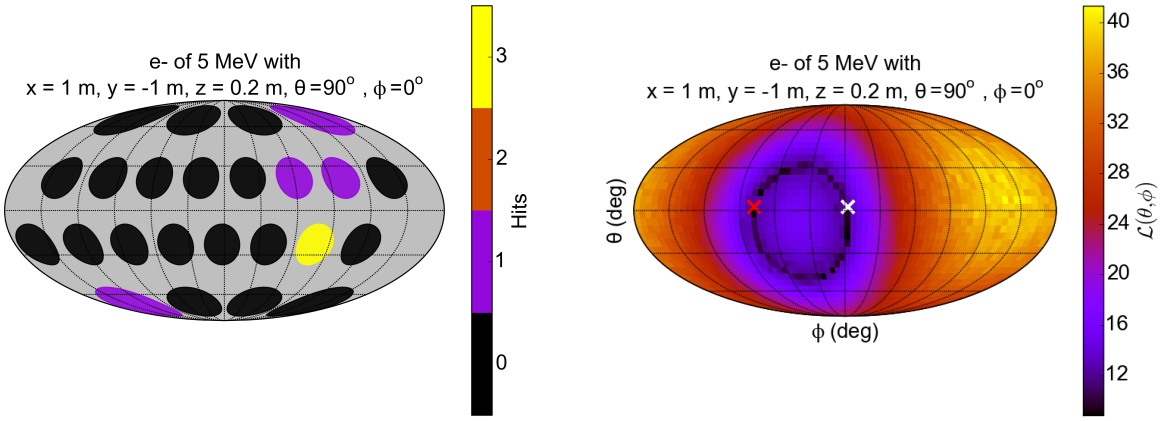

Figure 6.6: Left: Illustration of the PMTs that have been hit by an example event. **Right:** Likelihood function $\mathcal{L}(\theta_{\mathrm{dir}}, \phi_{\mathrm{dir}})$ for all possible θ and ϕ assuming that position and energy of the particle are known in the reconstruction of the example event. The white marker represents the real direction of the event, while the red marker is depicted at the minimum of the likelihood function.

In Fig. 6.6 right, two little markers (white and red) have been depicted over the likelihood function. The white marker is depicted over the coordinates of the real direction of the event, while the red marker is over the minimum of $\mathcal{L}(\theta_{\mathrm{dir}}, \phi_{\mathrm{dir}})$. It can be seen that there is a circular region where the value of the likelihood function is considerably smaller than the rest of the regions. This emerges because of the aforementioned uncertainty in the direction of a photon produced by Cherenkov effect, which translated to a (θ, ϕ) space looks like a circle in it. If there were not uncertainty because of the Cherenkov cone, the position of the markers should be the same for a likelihood function working as desired. In fact, the minimum where the red marker is plotted in Fig. 6.6 is mainly statistics and there is no reason why both markers should be at the same coordinates, since all the

directions inside the circular region of low likelihood values are equally probable to give the same event. In Fig. 6.7 are presented the $\mathcal{L}(\theta_{\text{dir}}, \phi_{\text{dir}})$ for two different events, where the likelihood space looks much different since it depends on the particular event. It is remarkable that the event on the left part of the plot was only detected by two different PMTs, which shows the capability of this method with just few statistic.

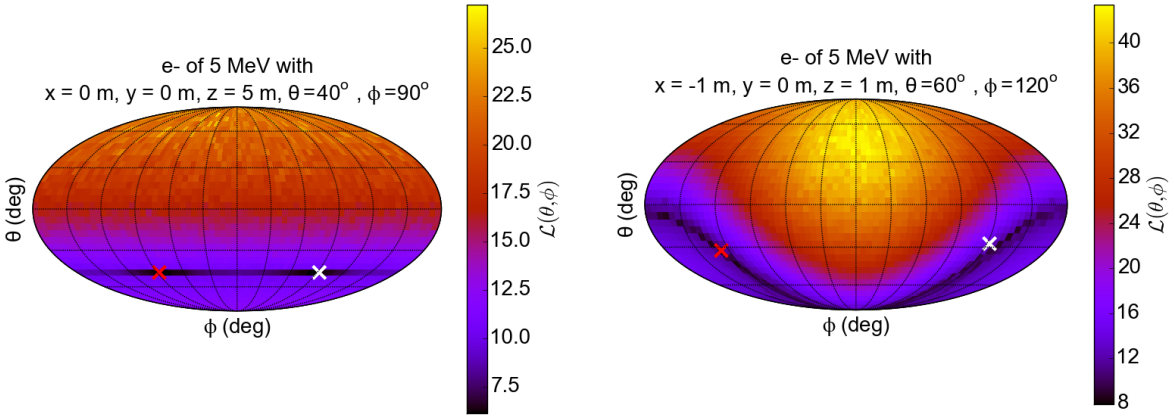

Figure 6.7: $\mathcal{L}(\theta_{\text{dir}}, \phi_{\text{dir}})$ for 2 different events.

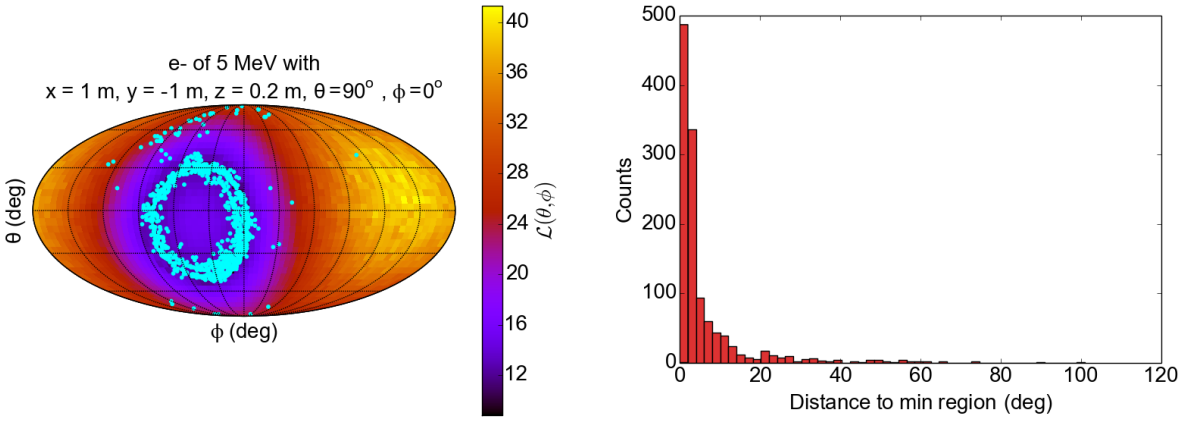

Figure 6.8: Left: Result of the minimization algorithm (cyan dots) plotted over the likelihood space for a certain event. **Right:** angular difference between the results obtained from the minimization algorithm and the closest point from the region of minimum $\mathcal{L}(\theta_{\text{dir}}, \phi_{\text{dir}})$ of this event.

More events, which are not shown here, have been reconstructed using this method. From all the results, one can safely say that $\mathcal{L}(\theta_{\text{dir}}, \phi_{\text{dir}})$ gives a region of potential minimum, but not a useful minimum itself. A minimization algorithm can be used to reach the minimum region without building the whole likelihood space. In the following, this is done as an example of the usefulness of the likelihood function. A minimization algorithm is written with Minuit2 [62, 63] using the method known as *simplex method* [64]. In an attempt to reconstruct the event plotted in Fig. 6.6, the simulation is run with random θ and ϕ and the minimization algorithm tries to find the minimum by repeating the simulation at different coordinates. The result of this is shown in Fig. 6.8. The simplicity of this method makes it to not always find the correct minimum, but the purpose here was just to show

that in a fast way the minimum of $\mathcal{L}(\theta_{\text{dir}}, \phi_{\text{dir}})$ can be obtained with just a few simulations instead of building $\mathcal{L}(\theta_{\text{dir}}, \phi_{\text{dir}})$ at each θ and ϕ. The simulation has been run an average of 17.08 times per minimization. By making this number higher, the minimum should be found with better accuracy. It can be seen that most of the minimization results lie over the circular region of minimal $\mathcal{L}(\theta_{\text{dir}}, \phi_{\text{dir}})$.

In the next sections it will be studied how the likelihood space changes depending on the parameters of the event. This, in fact, provides information about the sensitivity of the mDOM to these parameters of MeV events.

6.3.2 Study of the likelihood function with the distance and energy of the events

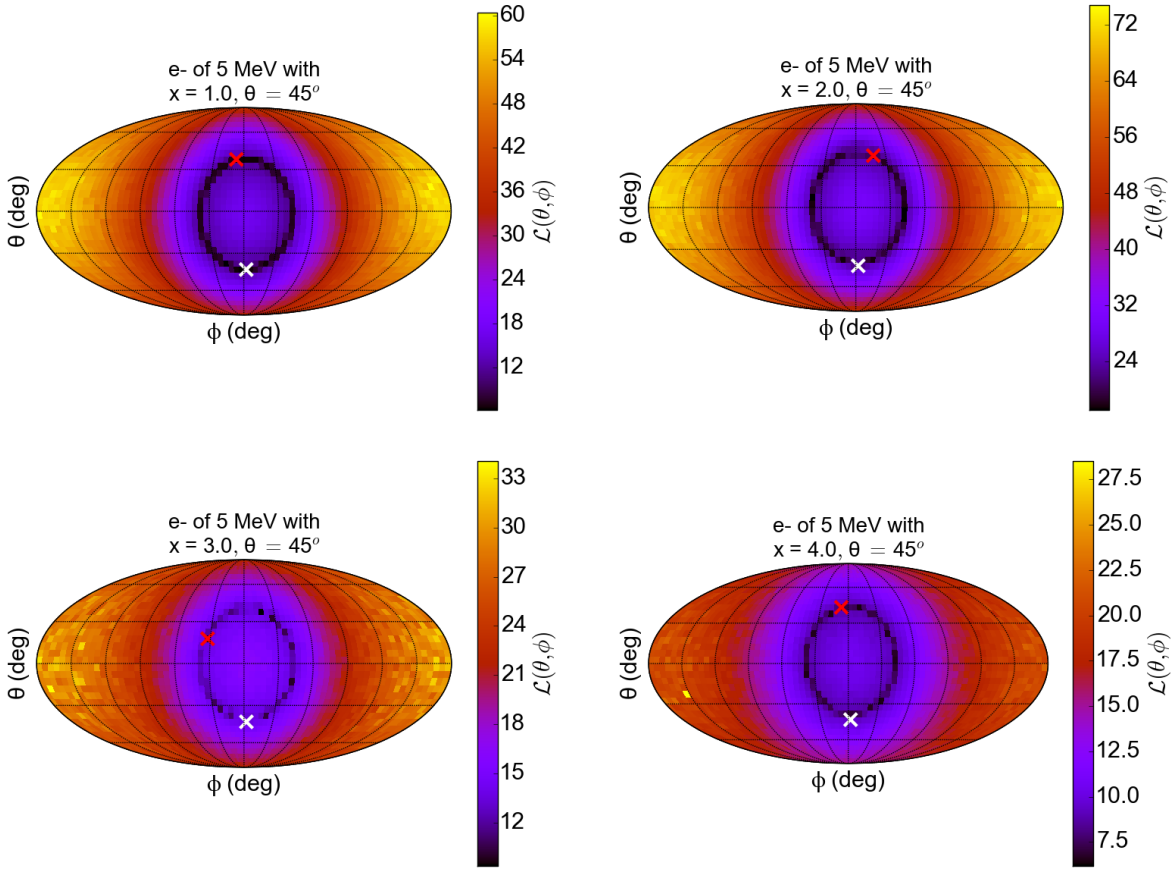

Figure 6.9: Likelihood function $\mathcal{L}(\theta_{\text{dir}}, \phi_{\text{dir}})$ for events at distances x = 1, 2, 3 and 4 meters of the mDOM, with the same energies and direction.

So far, it was assumed that energy and distance of the event are known, but the likelihood function might change with the energy of the event or its distance with respect to the mDOM. For further events, the detected photons are more likely to have suffered scattering, meaning a loss of information about their direction. Lower energetic events also provide less statistics. Fig. 6.9 shows the likelihood function for events which differ in the

distance from the mDOM at which they have been generated. Comparing the results, it can be seen that the circular region of the minimal $\mathcal{L}(\theta_{\text{dir}}, \phi_{\text{dir}})$ does not change its position with the distance. The likelihood space seems better defined for closer events because of larger number of statistics, both in n_i and μ_i. This can be seen better in Fig. 6.10, where the results of cutting $\mathcal{L}(\theta_{\text{dir}}, \phi_{\text{dir}})$ at $\theta = 0^o$ are is shown.

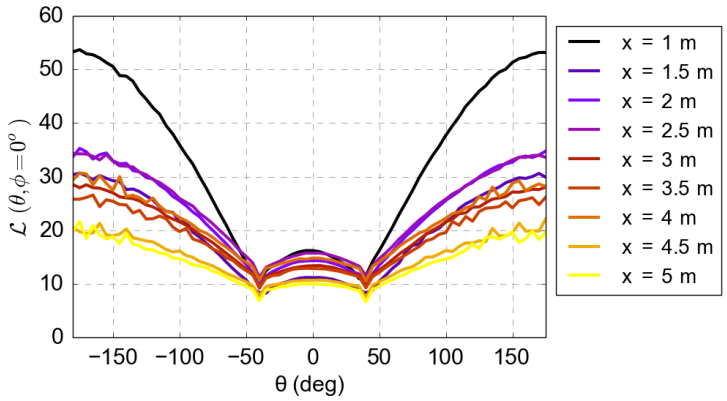

Figure 6.10: Likelihood function cut in $\theta = 0^o$ for events at different distances from the mDOM, with the same energy and directions.

A closer event would likely produce more hits than a further one, but if they lie over the same direction, the PMTs that they are able to hit are mainly the same. A similar behaviour can be expected with the energy of the events. This is briefly shown in Fig. 6.11, where the likelihood for two events with different energies have been obtained. The circular region of minimum likelihood is also better defined when increasing the energy because of the larger statistics, but it can be found at the same place.

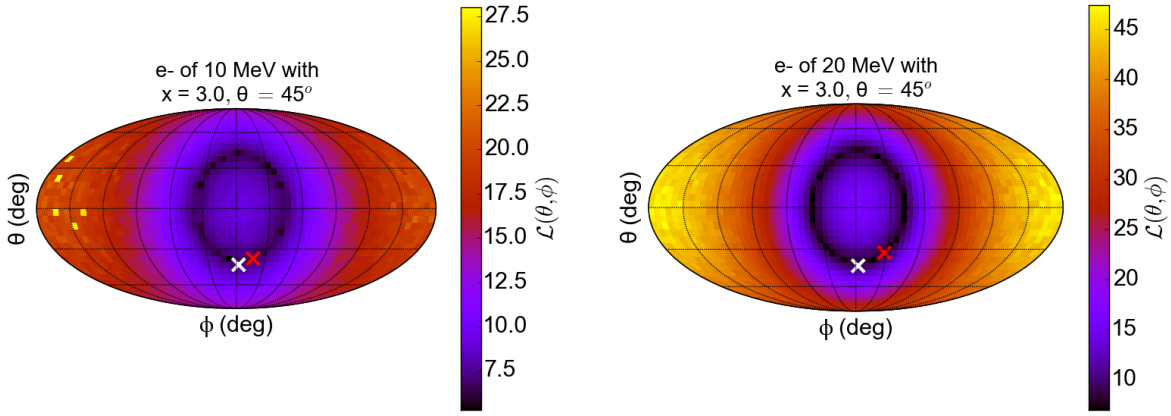

Figure 6.11: Likelihood function $\mathcal{L}(\theta_{\text{dir}}, \phi_{\text{dir}})$ for events with E = 10 and 20 MeV of energy, at the same position and with the same direction.

Since the position of the region of minimum likelihood does not change with the distance of the events, would it change if the reconstruction is made at a distance that is not where the event has been generated? So far, it has been assumed that the true position of the event is well known. Here, the vector that points to the position of the event will be supposed to be known, but the distance at which the event occurs is not. This, for instance, would be the case when the vector position has been obtained from the direct reconstruction. To study this, an event is produced at 5 meters from the mDOM and the reconstruction is made at different distances along that same vector, therefore the

simulations to obtain $\mathcal{L}(\theta_{\text{dir}}, \phi_{\text{dir}})$ does not generate electrons at the same position of the event to reconstruct. The results are shown in Fig. 6.12. It can be seen that there is no significant differences between the likelihood built at the correct distance with the function at the wrong ones. A similar behaviour is expected if the reconstruction is made with wrong energy values.

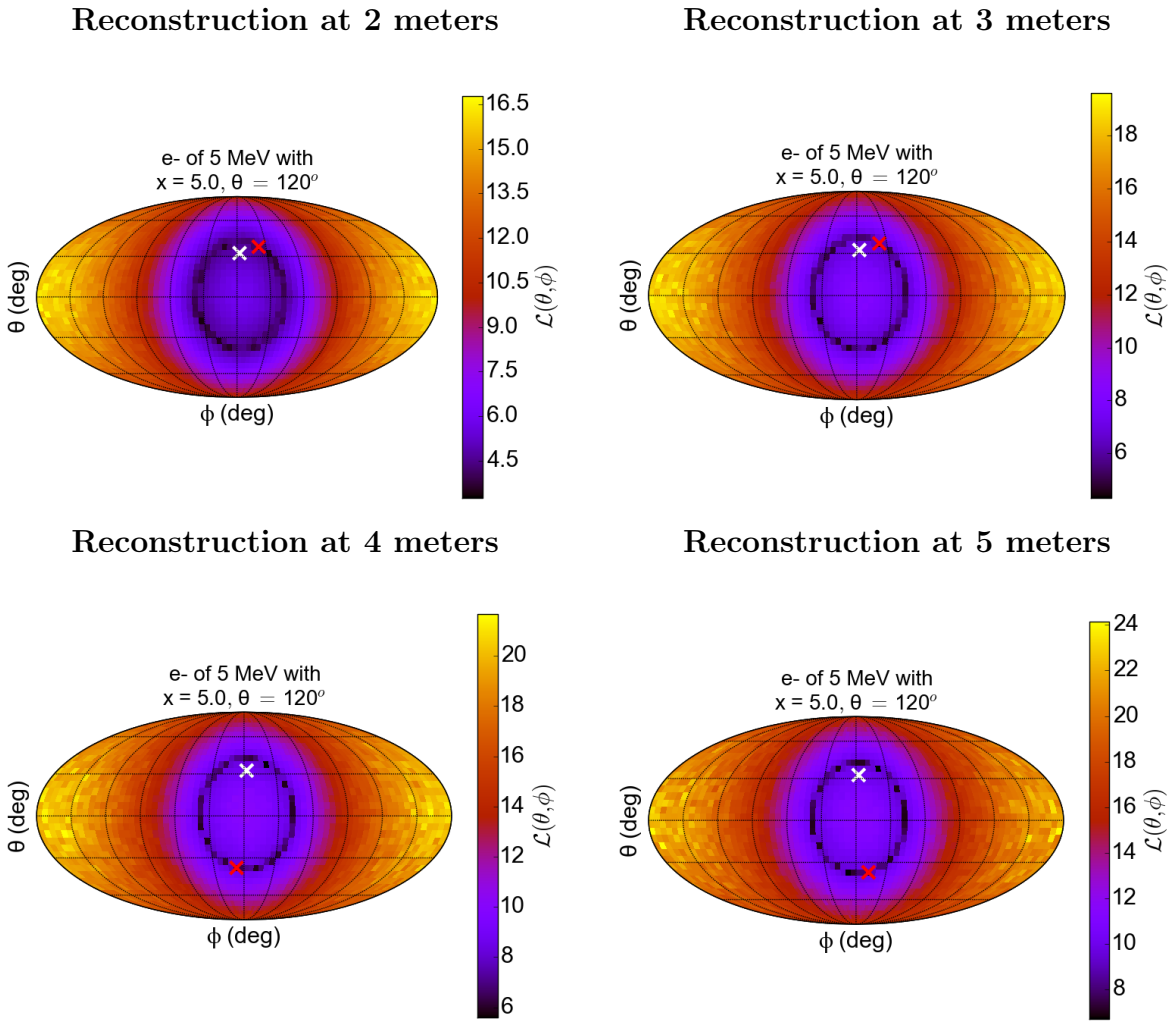

Figure 6.12: Likelihood function $\mathcal{L}(\theta_{\text{dir}}, \phi_{\text{dir}})$ for an event at a distance of x = 5 m, while the reconstruction has been done at x = 2, 3, 4 and 5 m.

This likelihood function can not be used to obtain the distance or energy of the events, since both are related only with the amount of statistics that the mDOM measures. Because they do not affect to the position of the minimum region, the likelihood space can go from the original 6-dimensional space into a 4-dimensional space: $\mathcal{L}(\text{r}, \theta_{\text{pos}}, \phi_{\text{pos}}, \theta_{\text{dir}}, \phi_{\text{dir}}, \text{E})$ $\rightarrow \mathcal{L}(\theta_{\text{pos}}, \phi_{\text{pos}}, \theta_{\text{dir}}, \phi_{\text{dir}})$, therefore it can be concluded that the likelihood space in θ and ϕ can be obtained when only the vector that points to the event is known. It should be noticed that if the likelihood is obtained at the wrong distance or energy, reasonable values for them should be provided to the simulation. Those values could be the radius of the effective volume of coincident events as the distance, and the mean energy of the spectrum as the energy.

6.3.3 Study of the likelihood function with the direction of the events

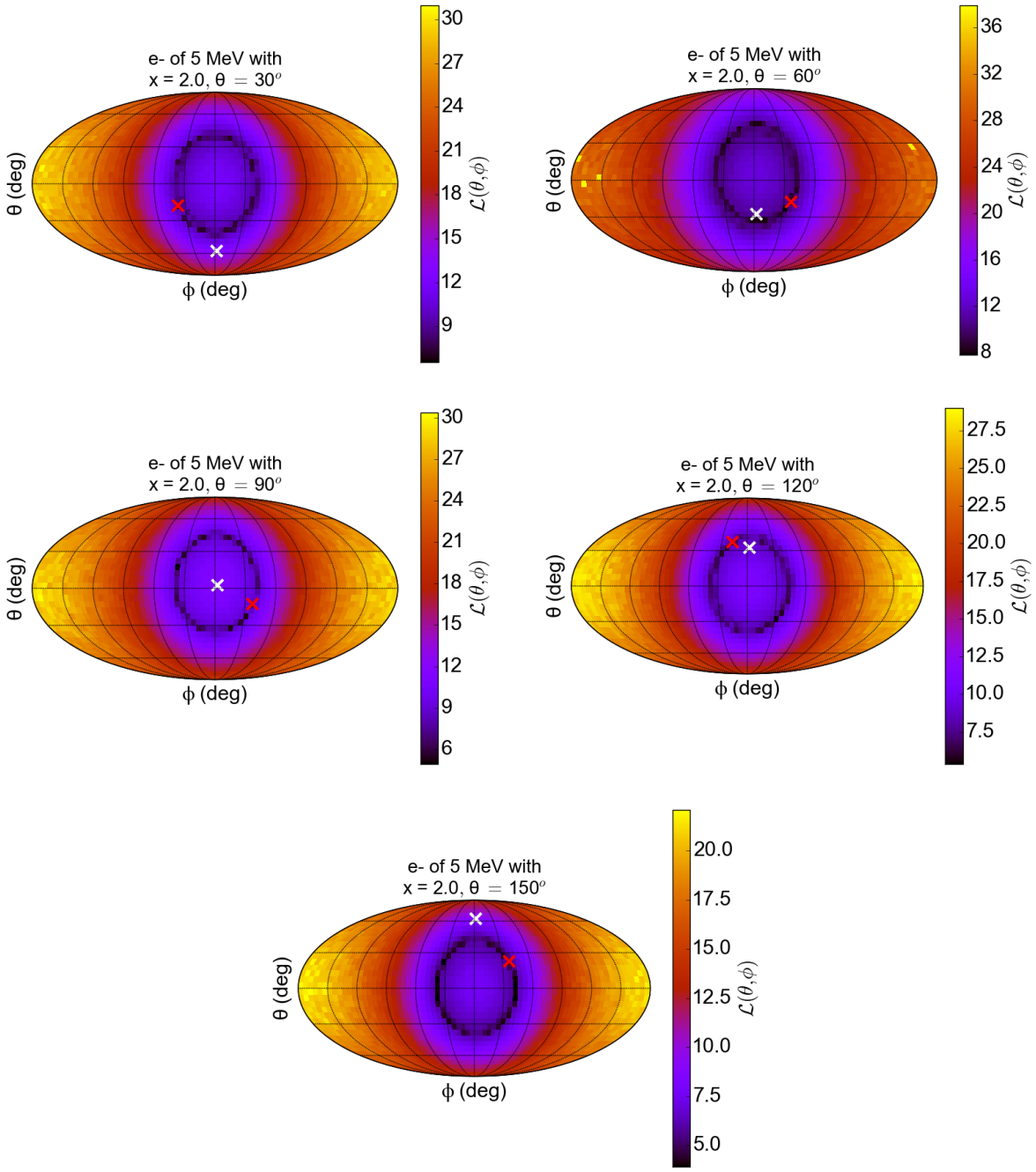

Figure 6.13: Likelihood function $\mathcal{L}(\theta_{\text{dir}}, \phi_{\text{dir}})$ obtained for events generated with the same position and energy, but with different directions: $\theta_{\text{dir}} = 30^{\text{o}}$, 60^{o}, 90^{o}, 120^{o} and 150^{o}, while ϕ_{dir} is always 0^{o}. The event with $\theta_{\text{dir}} = 90^{\text{o}}$ points directly to the center of the mDOM.

The behaviour of the likelihood function with the direction of the events will be now studied. Here, the events have been generated along θ_{dir} while ϕ_{dir} is kept constant.

Similar results are expected if the events would have been obtained at different ϕ_{dir}. At the position where the events have been generated, $\theta_{\text{dir}} = 90^o$ are events whose direction points to the center of the module. The results are depicted in Fig. 6.13.

Fig. 6.13 shows that changing the event direction does not change the likelihood function, while the white marker does change its coordinates, which results with the marker out of the circular region of minimum. This undesired behaviour is due the scattering of the particles, in particular of the electron. In Fig. 6.14, two different situations are depicted to illustrate it. If both events are detected, they would probably hit the same face of the mDOM. From the detection at the mDOM, these two events can not be differentiated if they give the same signal. It should not be overlooked that in these studies the events have been required to have some parameters. An event which initially does not point with an appropriate angle to the mDOM would be less likely to be detected than the contrary, resulting in a higher yield of detection of events whose direction over the likelihood functions are close to the region of minimum. For instance, this is the case of the events presented in Fig. 6.13 with $\theta = 30^o$ and $\theta = 150^o$. Those events are initially pointing to the mDOM with an angle of 60 degrees, which means that they need to suffer some scatter to be detected, resulting in a failure of the direction reconstruction from the likelihood function. Something similar occur with the event at $\theta = 90^o$, which, without any scattering, its emitted photons would just form a cone around the mDOM without hitting the PMTs.

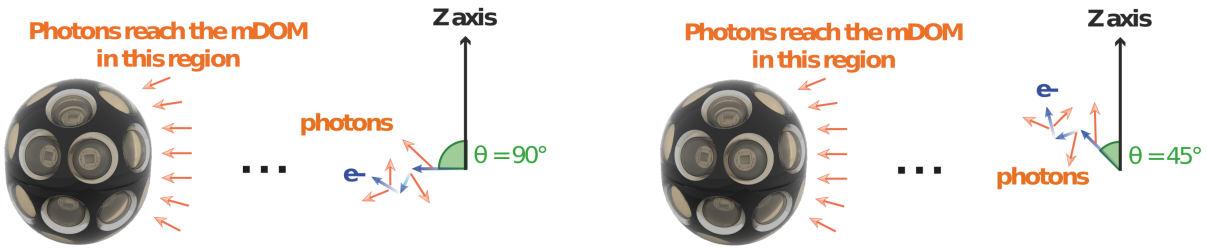

Figure 6.14: Representation of how two events with different directions can give a similar signal at the mDOM. Photons are emitted with the Cherenkov angle from the particle, but the particle itself suffers scattering and also the photons once they are produced. If photons reach the mDOM, they will reach the one face of the mDOM in a similar to a plane shock.

The calculations made in this chapter show not only the behaviour of the likelihood function but the sensitivity of the mDOM itself for the position, direction and energy of particles produced by MeV SN neutrino interactions. There is an uncertainty in the events directions that can not be avoided by the mDOM. This uncertainty is due both to the random nature of scattering of particles and the 2π uncertainty of the Cherenkov emission of photons. The reconstruction of the direction of individual events seems to need more sophisticated methods to reach more precise results, since the likelihood function built here might fail depending on the direction of the events, as well as it does not provide a global minimum but a region in the likelihood space where is more probably that the direction of the event is.

7 IceCube-Gen2 equipped with mDOMs for SN neutrino detection

In this chapter, the sensitivity of IceCube-Gen2 equipped with mDOMs to the detection of a core-collapse SN neutrino burst will be studied. First, the results for a SN burst at 10 kpc will be obtained. Then, these results will be used to estimate the sensitivity of the detector to extra-galactic SNe. A detailed calculation will be shown for the case of the heavy SN, while only the most important results will be shown for the lighter one (see section 2.3). Since the fluxes for LS220 and SFHo EoS shown very similar results, only the fluxes of LS220 EoS will be simulated.

7.1 A core-collapse supernova neutrino burst simulation

The simulated supernova is chosen to be in the positive direction of the Z-axis of the reference frame described before, which means at the center of the sky as seen from the South Pole. Because of the almost isotropic effective area of the mDOM, the direction of the SN should not modify significantly the results. A sketch of the simulation is presented in Fig. 7.1. The simulated volume consists in a cylinder of South Pole ice with 20 meters height and 20 meters radius oriented along the Z-axis, with the mDOM in its center.

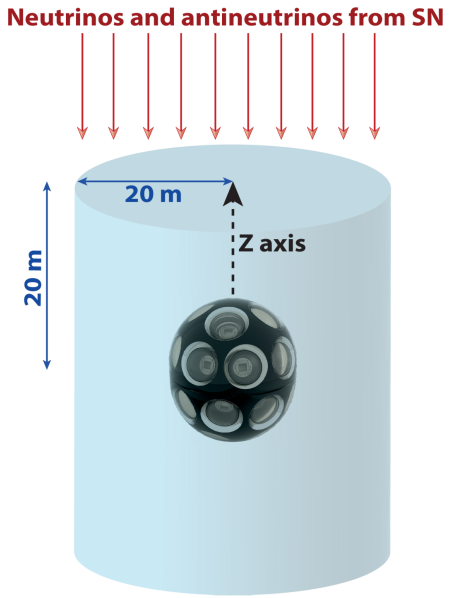

Figure 7.1: Sketch of the world simulation. Neutrinos and antineutrinos come from a SN along the positive Z-axis at a distance of 10 kpc. The light blue cylinder stands for the simulated volume, with the properties of South Pole ice and the mDOM in its center. Scales are only representative.

The procedure to simulate the neutrino and antineutrino interactions in ice is implemented using the particle generator explained in section 4.3, so ENEES for neutrino and IBD for

antineutrino interactions will be simulated. Quantum efficiency for the PMTs are directly applied in all simulations made in this chapter. To extrapolate the response of the whole IceCube-Gen2 using the simulation with one single mDOM two considerations are taken: first that in IceCube-Gen2 all the mDOMs face exactly in the same direction, and second that the properties of the ice are the same for all modules. For the first consideration, it can be assumed that, in the case it is not true, the rotation of each mDOM will be known, therefore this effect can be corrected. The second assumption is necessary in order to extrapolate the results from one single module simulation. The impact on the results of the chosen generation volume will be discussed later in section 7.3.

By using the particle generator, the events must be weighed according to their interaction probability in the simulated volume and to the number of them that would travel throughout the simulated volume in a real SN explosion. This is done by using the individual ω_e and general W_T weights from Eq. 4.3 and 4.4. The cylindrical volume simplify the geometrical parameters in both formulas. For the fluxes presented in section 2.3.1 of the heavy SN with LS220 EoS and the surface of the cylinder as defined in Fig. 7.1, the general weights from Eq. 4.4 are:

$$W_T\left(\nu_e + e\right) = \frac{2.08 \times 10^{23}}{N_{\text{generated}}} \tag{7.1}$$

$$W_T\left(\overline{\nu}_e + p\right) = \frac{1.58 \times 10^{23}}{N_{\text{generated}}}, \tag{7.2}$$

assuming that the SN takes place at 10 kpc of Earth and that IceCube-Gen2 will be equipped with 15000 mDOMs. The individual weights ω_e from Eq. 4.3 have a different value for each event, since the total cross section of the interaction depends on the energy of the incident particle. By weighing, the number of events that are detected in the simulation with one single mDOM are scaled with the number of events that would be detected by a whole IceCube-Gen2 extension equipped with mDOMs from a core-collapse SN burst. Since the detected events will be weighed, the uncertainties of the quantities exposed in this chapter are only statistical, obtained by doing $\sigma(x) = \sqrt{\sum_i^N \omega_e^2(i) \cdot W_T^2(i)}$, where i is each event included in the calculation of x.

7.1.1 Results for ENEES

The results for the detection of electrons coming from ENEES of SN neutrinos are presented here, after multiplying the signal that each event produces in the mDOM by its individual and global weights as described before. In Fig. 7.2, the number of hits and the number of PMTs that have been hit per detected event are shown. From these results, the expected number of detected neutrinos coming from a heavy SN at 10 kpc is $(8.328 \pm 0.008) \times 10^4$ events. The ratio between the number of events with coincidences and the total detected events is $(5.25 \pm 0.03)\,\%$. There are few events giving a large number of hits. This is explained by the events whose electrons have likely entered in the glass of the mDOM, producing there a lot of Cherenkov photons that are collected by the PMTs.

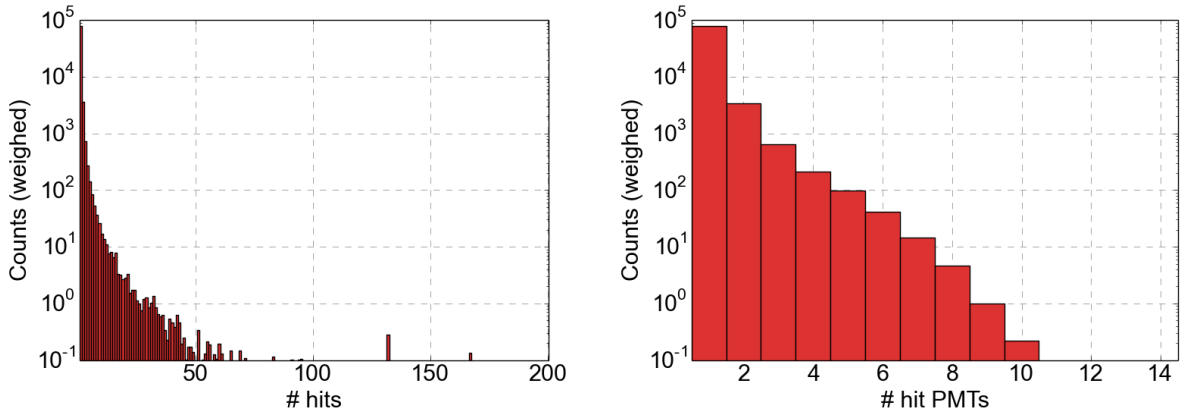

Figure 7.2: Number of hits (**left**) and number of PMTs that have been hit (**right**) per detected event from ENEES of neutrinos coming from a heavy SN at 10 kpc in a whole IceCube-Gen2 detector using mDOMs as modules.

On the left side of Fig. 7.3, the time difference between the earliest and latest hit from the same coincident event is shown. From the results, it is obtained that ∼99% of the coincident events would produce their coincidences within less than 10 nanoseconds.

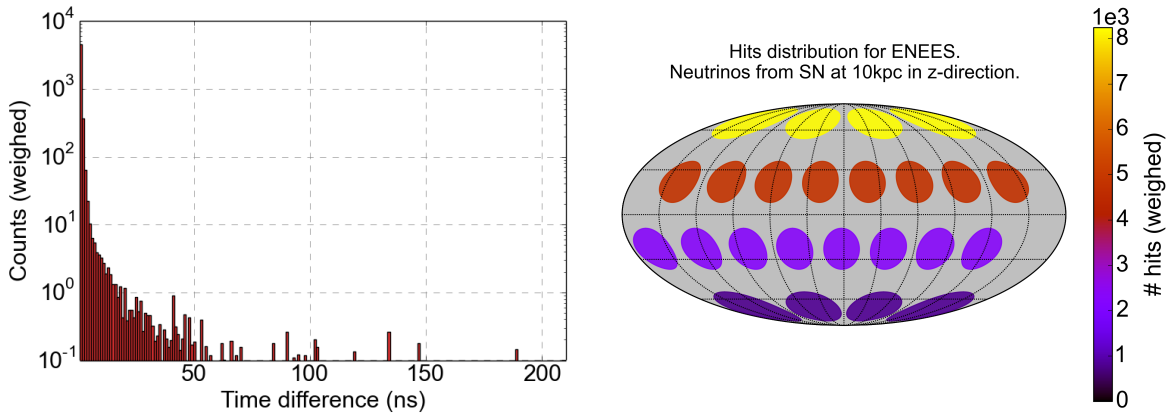

Figure 7.3: Time difference between the earliest and latest hit from the same coincident event (**left**) and distribution of the hits in the modules (**right**) for ENEES of neutrinos coming from a heavy SN at 10 kpc in a whole IceCube-Gen2 detector equipped with mDOMs. It is assumed that all mDOMs are facing in the same direction.

Fig. 7.3 right shows the sum of the hits for each PMT of all mDOMs assuming that every mDOM has the same orientation or that the orientation differences have been corrected. The results clearly show a higher yield of detection in the PMTs facing directly to the direction of the SN, as expected from the direction conservation of ENEES. Although the Cherenkov photons are produced along a cone from the path of the electron, when a big number of events are taken into consideration, it statistically leads to a clearly preferential direction which points to the source.

7.1.2 Results for IBD

In the same way as for ENEES, the results for positrons coming from IBD of heavy SN antineutrinos at 10 kpc are obtained. The results of the number of hits and the number of PMTs that have been hit can be seen in Fig. 7.4. The detected events are $(6.311 \pm 0.004) \times 10^6$, where (7.56 ± 0.02) % of them give coincidences. In comparison, the results for IBD are much higher than for ENEES, as it is expected because of the larger cross section of IBD and the larger energy of its generated particle, which also increases the ratio of coincidences.

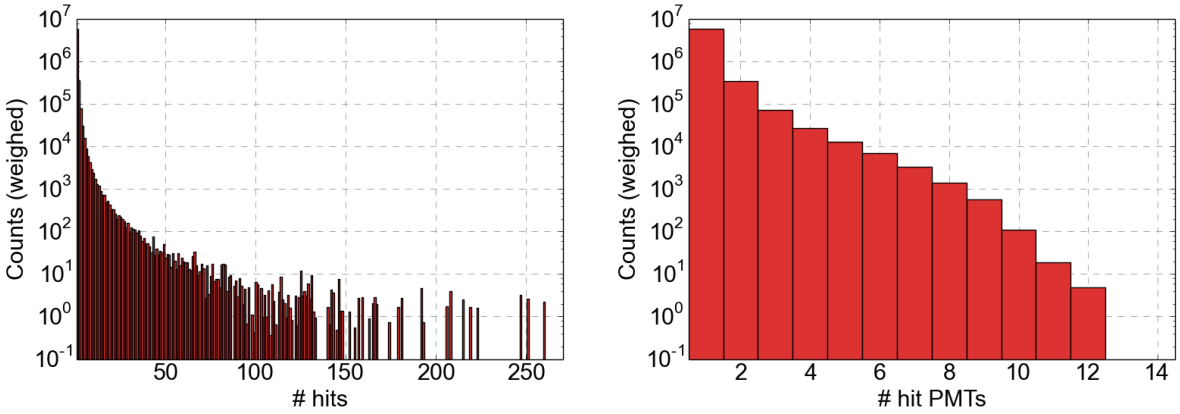

Figure 7.4: Number of hits (**left**) and number of PMTs that have been hit (**right**) per detected event from IBD of antineutrinos coming from a heavy SN at 10 kpc in a whole IceCube-Gen2 detector using mDOMs as modules.

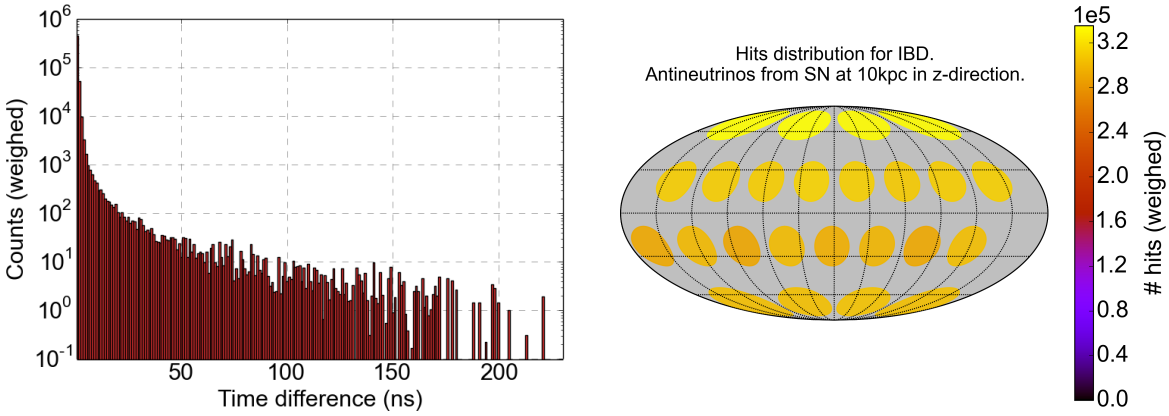

Figure 7.5: Time difference between the earliest and latest hit from the same coincident event (**left**) and distribution of the hits in the modules (**right**) for IBD of antineutrinos coming from a heavy SN at 10 kpc in a whole IceCube-Gen2 detector equipped with mDOMs. It is assumed that all mDOMs are facing in the same direction.

Fig. 7.5 shows the results of the time difference between the earliest and latest photon from a coincident event and the hits distribution along the PMTs in the mDOM, analogously as

done in the case of ENEES. Again, in about 99% of cases, photons from coincident events reach the PMTs within 10 nanosecond. From the hit distribution, it can be observed that the hits are spread much more homogeneously around the mDOM than in ENEES, with a slightly higher number of hits in the PMTs that are facing the direction of the antineutrinos, as expected from the results of Fig. 4.7.

7.1.3 Combined results

In the previous subsections, the SN neutrino interactions have been studied individually. In a real SN detection it would not be possible to distinguish them, since all the hits would be detected together, as well as the rest of interactions which were not included in the simulation. From this point of view, the quantities presented here are slightly underestimated in regard to what to expect from a real SN detection, where not only ENEES and IBD but the rest of interactions of ν_x and $\overline{\nu}_x$ would take place. The results of adding up together ENEES and IBD are summarized in Tab. 7.1. Around 6.4 million events would be detected by IceCube-Gen2 equipped with mDOMs for a core-collapse SN of 27 M_{sun} of progenitor mass at 10 kpc, according with the simulation made in this work.

Table 7.1: Results of a SN at 10 kpc in a whole IceCube-Gen2 extension equipped with mDOMs, obtained from simulating ENEES and IBD with the fluxes of a SN which results in a 1.77 M_{sun} baryonic neutron star and whose progenitor mass is about 27.0 M_{sun} (see section 2.3.1). R(X ns) stands for the ratio of events that give coincidences in less than X ns. Only statistical uncertainties has been assumed.

	Simulation results (ENEES+IBD)
Detected events	$(6.394 \pm 0.004)\times10^6$
Coincident events	$(4.81 \pm 0.01)\times10^5$
Ratio of coincident events (%)	7.53 ± 0.02
Events that hit $\geq$3 PMTs	$(1.261 \pm 0.006)\times10^5$
Events that hit $\geq$4 PMTs	$(5.26 \pm 0.04)\times10^4$
Events that hit $\geq$5 PMTs	$(2.54 \pm 0.03)\times10^4$
R(1 ns) (%)	85.7 ± 0.1
R(10 ns) (%)	99.2 ± 0.1

In [7] it was estimated that the actual configuration of IceCube would detect around 1.1 million events from a SN at 10 kpc[1]. The results from this simulation give a factor of $\sim$2 more detected events per module. This result will be discussed later in section 7.3, since it slightly disagrees with what expected from the results of the effective volume in chapter 5. The differences between IceCube and IceCube-Gen2 with mDOMs become larger when considering coincident rates. From the simulation it has been obtained that 7.53% of the events gives a coincident signal, while in IceCube this number was estimated to be only a few per mil. PINGU extension equipped with higher quantum efficiency DOMs would have a coincident rate of only 1% for MeV neutrino in the best case [45].

[1]The results from [7] were obtained by a SN model whose progenitor star mass is about 20 solar masses.

If the direct reconstruction from equations 6.2 and 6.3 is done using each PMT with all the photons that have been detected, the obtained vector direction is $\hat{\vec{v}} = (0.016,\ 0.003,\ -0.999)$. This is the average direction of the detected photons. The original direction of the simulated neutrinos is $(0, 0, -1)$, therefore, it can be seen that the direct reconstruction gives the average direction of the neutrinos when a large number of events have been detected, even if IBD reduces significantly the preference directionality of events. The vector $-\hat{\vec{v}}$ can also be used as a vector pointing to the SN in the sky, which gives the right direction with a deviation of 0.95^o with respect to the real one.

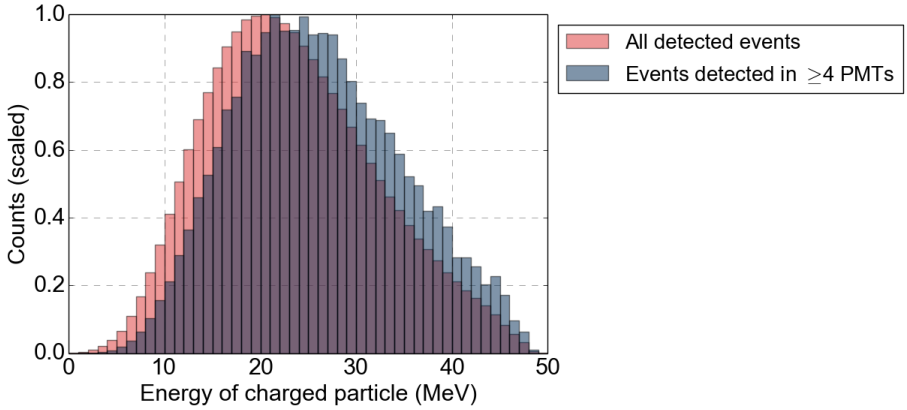

Figure 7.6: Energy distribution of detected events and of events which have been detected in at least 4 different PMTs. The histograms have been scaled to one for better comparison.

In Fig. 7.6, the energy distribution of the detected events have been depicted. Because higher energetic events present a larger cross section and also produce more Cherenkov photons, the energy spectrum of detected events tends to higher values in comparison with the spectrum of the whole flux of neutrinos or antineutrinos, shown in Fig. 4.5. It can also be seen that, when four hit PMTs are requested to the events, the spectrum tends to higher energies, since higher energetic particles are more likely to produce coincidences and meet conditions like this one. The mean energy of all detected events by a core-collapse SN of IceCube-Gen2 with mDOMs results to be $\langle E \rangle = (22.92 \pm 0.02)$ MeV, while it is $\langle E \rangle = (25.5 \pm 0.2)$ MeV for the events detected in 4 or more PMTs.

The losses due to the consideration of ENEES and IBD as the only interactions of SN neutrinos in ice can be estimated to be around 4.2% of the detected events, according with the results of [25]. This would lead to a total of about 6.8 million detected events considering all interactions, obtained from scaling the results from table 7.1.

A no neutrino oscillation scenario has been assumed for all this calculations. A fast calculation can be done to estimate the number of detected events with different oscillation scenarios, using the results from table 7.1 and the data from [1], which gives a value of $\sim$ 7.2 million events detected in a normal hierarchy scenario, and $\sim$ 8.9 million events for a inverse hierarchy scenario. Thus, the scenario of no oscillation leads to the weakest signal. Inverted neutrino mass hierarchy would provide the largest signal because energetic $\overline{\nu}_x$ would oscillate into $\overline{\nu}_e$ [12]. Nevertheless, these results are just illustrative, since a different oscillation scenario would also modified the energy spectra, therefore another simulation should be done in order to calculate appropriate values.

7.1.4 Results for a lighter SN

The results above have been obtained for a SN explosion of a $27\,M_{sun}$ star which results in a $1.77\,M_{sun}$ neutron star. In table 7.2, there are summarized the most important results obtained using the fluxes of a progenitor star of $9.6\,M_{sun}$ which results in a $1.36\,M_{sun}$ neutron star, using again the model of LS220 as EoS, calculated in the same way as before.

Table 7.2: Results of a SN at 10 kpc in a whole IceCube-Gen2 extension equipped with mDOMs, obtained from simulating ENEES and IBD with the fluxes of a SN which results in a $1.36\,M_{sun}$ baryonic neutron star and whose progenitor mass is about $9.6\,M_{sun}$ (see section 2.3.1). R(X ns) stands for the ratio of events that give coincidences in less than X ns. Only statistical uncertainties has been assumed.

	Simulation results (ENEES+IBD)
Detected events	$(2.799 \pm 0.002)\times10^6$
Coincident events	$(1.984 \pm 0.006)\times10^5$
Ratio of coincident events (%)	7.08 ± 0.02
Events that hit $\geq$3 PMTs	$(5.11 \pm 0.03)\times10^4$
Events that hit $\geq$4 PMTs	$(2.09 \pm 0.02)\times10^4$
Events that hit $\geq$5 PMTs	$(9.8 \pm 0.2)\times10^3$
R(1 ns) (%)	85.7 ± 0.1
R(10 ns) (%)	99.2 ± 0.1

The number of detected events is lower for this SN model by a factor of about 2.3, which is consistent with the expected results according with the rate of expected interactions calculated in section 2.3.1. The ratio of coincident events is also lower, because of the lower energy of the spectrum of the lighter SN. If the mean energy of the detected events is calculated, the result gives a value of $\langle E \rangle = 20.39 \pm 0.03\,\text{MeV}$ for all detected events, while events detected in 4 or more PMTs have a mean energy of $\langle E \rangle = 22.7 \pm 0.4\,\text{MeV}$. Since the light and heavy SNe simulated in this chapter are near the lower and upper mass limits for stars which result in a neutron star after the SN explosion, the results can be seen approximately as lower and upper limits of the detected events from such SNe at a distance of 10 kpc.

7.2 Sensitivity for the detection of extra-galactic SN neutrinos

The results of the last sections are very encouraging for the detection and investigation of SNe within the Milky Way. Nevertheless, the expected rate of galactic SNe is only between 1 and 3 per century [65]. In this section, the results from the simulation calculated before are used in order to determine the potential of IceCube-Gen2 equipped with mDOMs for the detection of extra-galactic SNe. The study will be done using the results obtained for

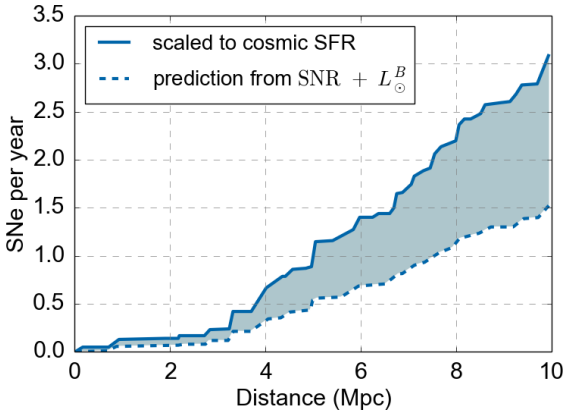

Figure 7.7: Range of cumulative expected supernova rate; lower curve according to observed SN rate and blue luminosity (SNR + $L_{\odot}^{B}$), upper curve scaled to match expectations from the cosmic star formation rate (SFR). Data kindly provided by *S. Böser* [25].

the heavy SN.

The flux of neutrinos and antineutrinos which reach us from a SN would decrease with the distance as d^{-2}. This means that, when a SN explosion takes place at far distances, only mini-bursts of neutrinos would reach detectors on Earth [25, 66]. This translates into the detection of just few events from extra-galactic supernovae. In Fig. 7.7 the cumulative expected SN rate as a function of the distance is shown, according to the observed SN rate and blue luminosity[1], and according to the expectations from cosmic star formation rate [25, 68]. The rate of SNe detection by actual detectors seems to be about half of the expected considering massive-star formation rates [69]. A detector able to measure extra-galactic SN neutrinos can help to solve this riddle, and test models of dark SNe – core collapse objects that directly form a black hole –, mergers of binary neutrino stars or the formation of quarks stars [25]. IceCube-Gen2 is planned to be focused on the detection of very high energetic neutrinos, but its potential for the detection of low energetic extra-galactic SN neutrinos should not be underestimated because of its possibility for local coincidences in each module. Assuming the SN rate production given by these two models, the extra galactic SN detection rate is calculated in the following sections.

7.2.1 Constrains imposed by dark noise

So far, events with only one single registered photon have been considered as identifiable signal events. However, this is usually not enough to distinguish events from background signals. Above the low cross sections of neutrino interactions, the main problem of neutrino detectors is the detection of not-desired background events, and this become even more important when trying to detect a few number of low energetic neutrinos. Until now, this work has not discussed background signals. Beyond the background rate due external sources like the Sun or the atmospheric neutrinos, which could be avoided by using selection algorithms (not yet written) or by their directionality, an intrinsic *dark noise* is present in every single module. Let us define the noise rate as the rate of detection produced by events generated internally in the mDOM. So far, the expected noise rate per

[1]Blue luminosity and SN formation rate in galaxies are related, while the relation changes for SN and galaxy types. The combination of the observed SN rate and blue luminosity is often used to estimate the number of SNe in a galaxy [67].

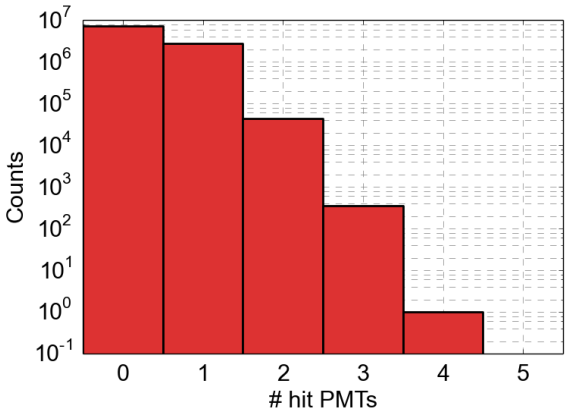

Number of hit PMTs.

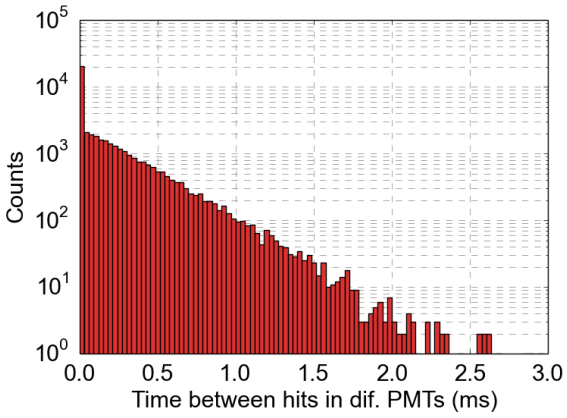

Time differences in ≥2 PMTs.

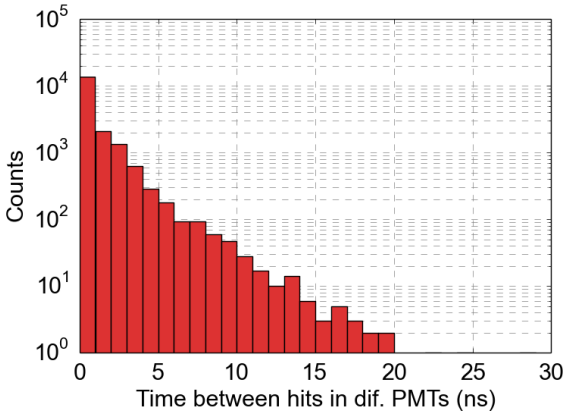

Time differences in ≥2 PMTs only for Cherenkov photons.

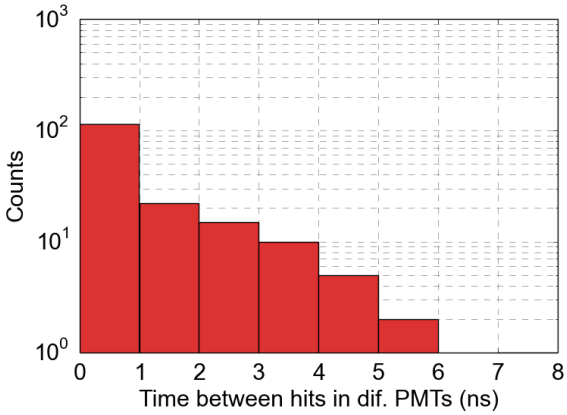

Time differences in ≥3 PMTs only for Cherenkov photons.

Figure 7.8: Results of ^{40}K decay in the glass for the number of hit PMTs and the time differences between the hits. Data courtesy of IceCube group Münster.

PMT in the mDOM has not been totally determined, since there is not a definitive version of the materials for the glass, the PMTs and the gel that will compose the mDOM. The dark noise per PMT would mainly depend on these materials, since its main contribution comes from the radioactive isotopes present in them, as well as on the internal dark rate of the PMTs themselves [38]. The radioactive decays cause signals in the PMTs because they are able to produce optical photons both by Cherenkov effect or scintillation of the glass. Provisional studies suggest that a conservative value for the dark noise would be around 500 s^{-1} per PMT. For our case, the dark noise will be defined as uncorrelated when the signal produced by them do not show temporal or spatial dependencies between different PMTs in the same module. This is the case for the internal PMT dark rate. For the dark noise due to radioactive nuclei presented in the glass and gel, some correlation between different PMTs can be found [70]. This can have a negative impact, since they might look like a real event, but can turn into something positive if an algorithm is able to suppress them, which is still under study.

A brief test will be made in order to see the effects if no correlation in the dark noise

Table 7.3: Maximally allowed noise/background trigger rate f_{noise} for an average of 1 false SN event per year, consisting of N_ν events falling into a time window of ΔT_{SN}.

N_ν	ΔT_{SN} (s)	f_{noise} (ms^{-1})
3	10	0.86
4	10	3.74
5	10	9.61
6	10	18.82

produced by radioactive decays is assumed. The ^{40}K is expected to be the most important isotope producing Cherenkov photons in the glass, with an activity of (75.3 ± 0.7) Bq/kg [71], which gives a rate of $\sim$978 s^{-1} in the $\sim$13 kg of vessel glass[1]. These decays would also produce scintillation in the glass, however the scintillation photons are expected to arrive up to μs after the Cherenkov photons[2] [70, 72], therefore they can be easily distinguish from single SN neutrino interactions whose coincidences arrive just in few nanoseconds, as it was shown in the previous section. As an example, Fig. 7.8 shows the number of PMTs that have detected photons from 10 millions ^{40}K decays in the glass and the time difference between the hits when $\geq$2 or $\geq$3 different PMTs have detected them. It can be seen how most of the decays are not detected or are detected in only one PMT. Only around 0.5 % of the decays would be detected in two or more PMTs and $\sim$0.004 % in 3 or more PMTs. The first column of the time differences is much higher due to the Cherenkov photons which arrive within some nanoseconds, much faster than the scintillation effect whose signals arrive up to milliseconds after the decay. If a closer look to the lower values of the time differences is taken, it can be seen how the Cherenkov photons arrive with a difference of just few nanoseconds, as SN neutrino coincident signals do. The probability that one of these decays gives a hit in three different PMTs of the mDOM in 10 seconds is only of $\sim 4 \times 10^{-8}$, and even lower if more hit PMTs are required. Since the probability that the correlation of the dark noise cause a signal similar to the one produced by a SN is very small, for the scope of this study it can be assumed that the correlation has no impact over the probability of the dark noise to give false detections, therefore a non-correlated dark noise scenario will be assumed.

Still, uncorrelated dark noise is able to cause false detections. To allow detection of individual events, some conditions must be requested in order to determine whether a signal originates from a SN neutrino interaction or whether it was generated by dark noise. Trigger requirements will be applied to manage it, defined as a minimal number of PMTs being hit by an event n_{coin}, within a time window Δt_{coin}. Then, if an event causes signal in $\geq n_{\text{coin}}$ PMTs within a time $\leq \Delta t_{\text{coin}}$, it will be assumed that this event has been produced by a neutrino interaction. There would still be a possibility that dark noise causes such a trigger signal, but the rate of these noise triggers can be calculated. First, the probability that one PMT detects signal due to dark noise within a time window Δt_{coin} can be presented as the complementary of not registering any hit. This can be

[1] The activity of ^{40}K and other radionuclide in the vessel glass are still under study, and the values used here have not been confirmed yet.

[2] The production of scintillation photons depends on the composition of the glass. So far, an estimation from [72] has been used to reproduce this scintillation, which still needs deeper study.

Table 7.4: False SN rate detection for the considered cases. First and second columns determine the trigger condition. Third column shows the value of f_{noise} for that trigger condition, obtained by Eq. 7.5. Fourth column shows the minimum number of triggered events that are being required. Fifth column shows the rate of false SN detection cause by the dark noise, obtained by Eq. 7.6. Last column shows the percentage of detected events that causes coincidences within Δt_{coin}, according with the results of section 7.1.3.

n_{coin}	Δt_{coin} (ns)	f_{noise} (ms^{-1})	N_ν	False SN rate (year^{-1})	Events inside Δt_{coin} (%)
3	0.85	8.97	5	0.72	86.6
	1.2	17.88	6	0.74	94.4
4	10	4.6×10^{-2}	3	1.5×10^{-4}	99.7
			4	2.3×10^{-8}	
			5	2.6×10^{-12}	
5	10	2.0×10^{-5}	3	1.23×10^{-14}	99.7
			4	$<1 \times 10^{-15}$	
			5		

expressed by Poisson probability as:

$$P_{\text{m}} = 1 - P\left(0, \mu = f_m \Delta t_{\text{coin}}\right) = 1 - e^{-f_{\text{m}} \Delta t_{\text{coin}}}, \tag{7.3}$$

where f_m is the noise rate of one single photomultiplier. Once a hit is detected, it needs $n_{\text{coin}} - 1$ more hit PMTs within the time window to meet the trigger condition. The probability of this can be expressed as the complementary probability of registering $n_{\text{coin}} - 2$ hit PMTs as [25]:

$$P_{\text{noise}} = 1 - B_{\text{cum}}\left(n_{\text{coin}} - 2 | N_{\text{PMT}}, P_{\text{m}}\right), \tag{7.4}$$

where N_{PMT} is the number of PMTs per module and $B_{\text{cum}}\left(m|n,p\right) = \sum_{k=0}^{m} \binom{n}{k} p^k (1-p)^{n-k}$ is the cumulative binomial probability for up to m successes out of n tries when the probability of success is p [25, 61]. If f_{noise} is defined as the rate of events produced by the dark noise which meet the trigger condition in the whole detector, it can be written as [25]:

$$f_{\text{noise}} = P_{\text{noise}} \cdot f_{\text{m}} \cdot N_{\text{tot}}, \tag{7.5}$$

where N_{tot} is the number of modules in the detector. Since neutrinos come from SN in burst, in order to distinguish them from uncorrelated noise, a certain number of triggered events will be required within the time window of a SN burst. This means N_ν triggered events in a time window of $\Delta T_{\text{SN}} \sim 10\,\text{s}$. However, there would still be a probability of false SN detection. Under the constraint that a limited number of false SN detection has to be accepted, the number of false SN detection in one year can be obtained as [25]:

$$N_{\mathrm{SN}} = f_{\mathrm{noise}} \cdot [1 - P_{\mathrm{cdf}}\,(N_\nu - 2, \mu = f_{\mathrm{noise}} \Delta T_{\mathrm{SN}})] \cdot 1\,\mathrm{year}, \tag{7.6}$$

where P_{cdf} is the cumulative Poisson distribution. If the rate of false SN detection is limited to as much as one per year, the maximal allowed value of f_{noise} to not exceed this rate of false SN detection can be obtained by iteration from Eq. 7.6. The results are presented in table 7.3.

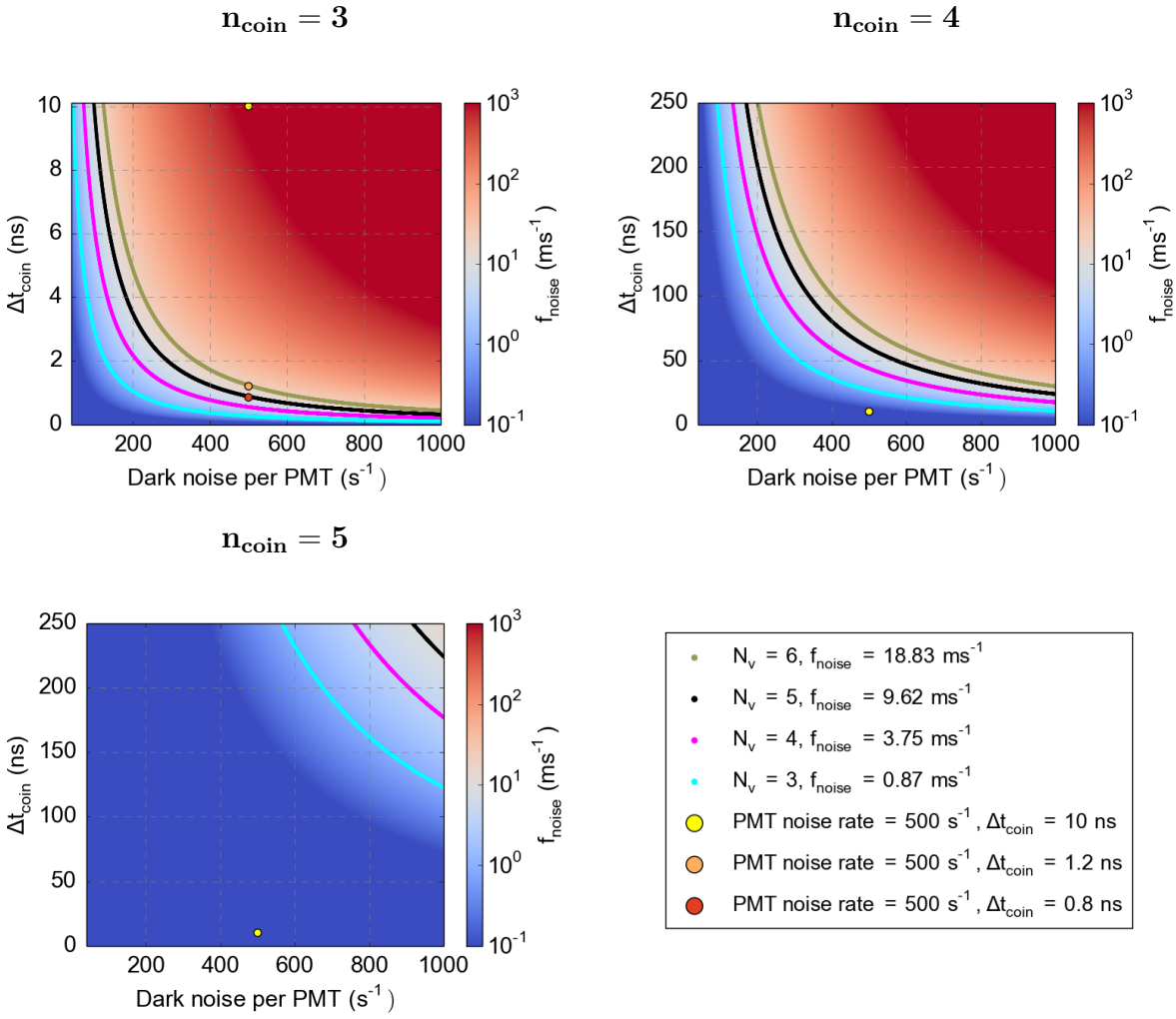

Figure 7.9: Value of f_{noise} for different number of hit PMTs (n_{coin}) as a function of the time trigger and the PMT noise rate. The maximal allowed values of noise rate for detection of $N_\nu = 3$, 4, 5 or 6 events within the trigger condition are shown as curves over the figures. Also, three different reference points corresponding to possible values for the noise rate and time trigger have been plotted.

Now that the maximum allowed values for the noise trigger rate have been obtained, it can be calculated whether the detector operates below these values or not. The values of f_{noise} as a function of the noise rate per PMT f_m and the time trigger Δt_{coin} are presented in Fig. 7.9 for $n_{\mathrm{coin}} = 3$, 4 and 5 hit PMTs. This figure brings information about the

allowed operation region of the mDOM. Over each figure, the position where the noise rate per PMT is $500\,\mathrm{s}^{-1}$ and the Δt_{coin} has values of 10, 1.2 and 0.8 ns has been depicted as reference points. The value of 10 ns is an appropriate reference, since $\sim 99\%$ of coincident hits from the same event occur within 10 ns, according with the results of the last section. It can be seen that the values of f_{noise} are well below the maximal allowed values in the case of $n_{\mathrm{coin}} = 4$ and 5 hit PMTs for most values of Δt_{coin}, even when demanding the detection of only 3 events. Therefore, in these cases, 10 ns of time trigger can be applied for the detection of $3, 4, 5$ or 6 events. If n_{coin} is chosen to be 3, the value of f_{noise} always surpass the allowed limits when Δt_{coin}= 10 ns. In order to be below the maximal allowed values of f_{noise}, the time trigger should be ~ 1.2 ns for the detection of $N_\nu = 6$ events and ~ 0.85 ns for the detection of $N_\nu = 5$ events. So far, it is not clear whether this is feasible, since the transit time spread of the PMTs might be around two nanoseconds. Therefore, the cases $n_{\mathrm{coin}} = 4$ and 5 hit PMTs with $N_\nu = 3$, 4 and 5 triggered events will be considered, while the cases of $n_{\mathrm{coin}} = 3$ hit PMTs with $N_\nu = 5$ and 6 triggered events will be presented taking into account the precaution announced above. It is also noticeable that, for most trigger conditions, the rate of false SN detections turn up to be much below than one, as shown in Tab. 7.4. There, it is also presented the percentage of the events lost by the Δt_{coin} condition with respect to the detected events with n_{coin} hit PMTs, from the results of the simulation. This percentage will be used to scale the results if the corresponding trigger is applied.

7.2.2 Expected extra-galactic SNe detection.

From the results obtained in the simulation and presented in the table 7.1, the probability for SNe detection as a function of the distance can be calculated. Since the fluxes change with the distance according to Eq. 2.13 as d^{-2}, the number of detected neutrinos and antineutrinos can be scaled down. This is done for the cases $n_{\mathrm{coin}} = 3$, 4 and 5 presented in the previous subsection and that satisfy the requirement of less that one false SN per year. By scaling the results, Fig. 7.10 is obtained.

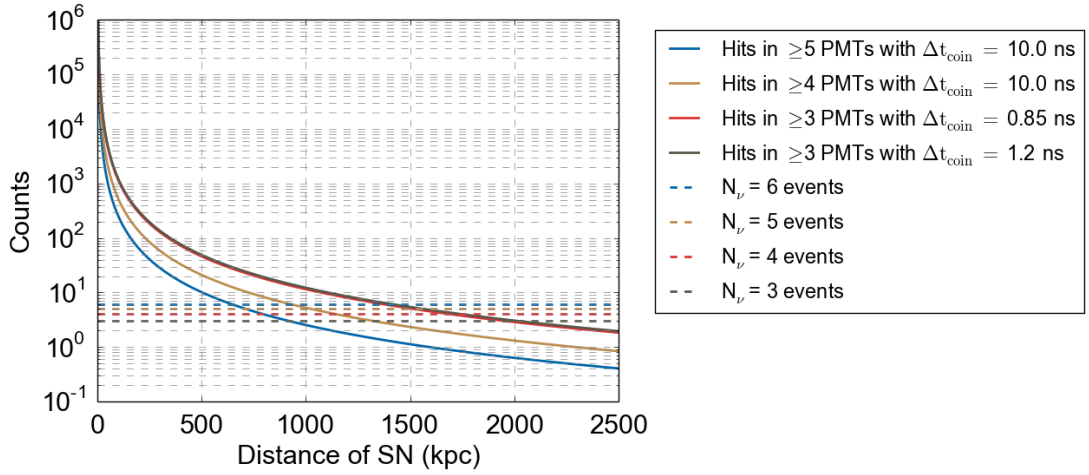

Figure 7.10: Results for the number of detected events scaled by the distance for the conditions that satisfied the triggers.

Table 7.5: Distances where the scaled curves of the expected number of detected events for each trigger condition reaches a certain number of detected events. The first and second columns determine the trigger condition. Third column shows the minimum number of detected event for the trigger condition. Fourth column shows the distance at which the expected number of detected events is equal to N_ν for each trigger condition.

n_{coin}	Δt_{coin} (ns)	N_ν	Distances at which the curves cut N_ν values (kpc)
3	0.85	5	1469 ± 5
	1.2	6	1408 ± 5
4	10	3	1323 ± 7
		4	1146 ± 6
		5	1025 ± 5
5	10	3	919 ± 7
		4	796 ± 6
		5	712 ± 5

Fig. 7.10 shows the expected number of detected events per SN distance for each trigger condition. From here, the table 7.5 shows the values where the curves has a value of $3, 4, 5$ or 6 expected triggered events. From the results, a Poisson probability can be built in order to get the probability of SN detection per distance. Being $\mu(d)$ the expected number of detected events for a certain trigger condition at the distance d, the probability that the trigger condition is satisfied is the probability of getting $n \geq N_\nu$, where N_ν is the minimal number of detected events demanded by the trigger. This can be easily expressed as:

$$P(n \geq N_\nu, \mu) = 1 - P_{\text{cdf}}(N_\nu - 1, \mu), \tag{7.7}$$

where P_{cdf} is the cumulative Poisson function. Performing this calculation with the data of Fig. 7.10 yields to Fig. 7.11. There it can be seen the probability of SN detection as a function of distance for all considered scenarios, with a dashed line crossing at 50% of detection probability. The safe scenario of require at least 3 events hitting 4 or more PMTs gives a probability of 50% for a SN detection at a distance of 1400 kpc, while a SN at 1469 kpc would be detected with 50% of probability when 5 triggered events hitting 3 or more PMTs are demanded. Therefore, the event-by-event detection of SN neutrinos coming much beyond the Large Magellanic Cloud, located at ~ 50 kpc, is assured. The results open the possibility to study SNe from e.g. the Andromeda Galaxy (~ 775 kpc) – largest galaxy of the local group – or the Triangulum Galaxy (~ 900 kpc).

The use of Eq. 7.7 to scale down the results leads to a small underestimation of the probability of detection by distance. The simulation has generated events within the first 10 s of the SN burst model. This means that the few neutrinos that are still being emitted at $t > 10$ s are not being considered. In a real detection, the time window of 10 seconds would be opened when the first event is detected, bringing the possibility to still detect those latest neutrinos.

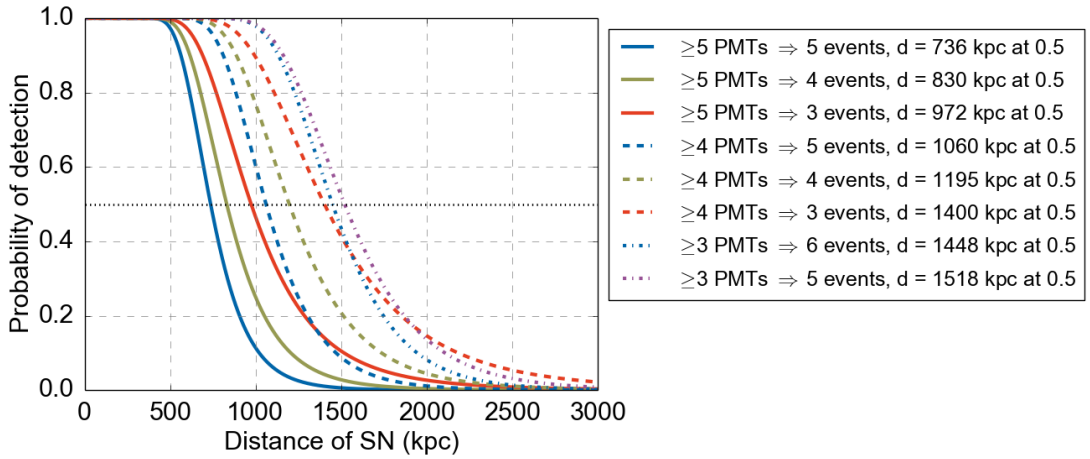

Figure 7.11: Probabilities of SNe detection with the distance in the considered trigger scenarios, calculated using the results obtained from the simulation of a whole SN detection in IceCube-Gen2 with mDOMs.

With the SN formation rate from Fig. 7.7 and the probability of detection per distance, the expected rate of SN detection for each trigger can be calculated. The results are summarized in table 7.6 for one decade of operation, which clearly show that $n_{\text{coin}} = 3$ can not be considered as an useful trigger condition, since the expected number of false SN detection is much higher than the expected real SNe detection. The highest detection rate would be obtained with the trigger condition of $N_\nu = 3$ events hitting 4 or more different PMTs within 10 nanoseconds. The trigger condition are just the minimum requirement, but a few SN might be closer, even galactic, yielding a much higher detection of triggered neutrinos. Because of the use of several models in this calculations, not only for the SN spectrum but also for the SN rate formation in the nearest universe, these numbers should not be assumed as definitive results and deeper studies should be done in order to claim a value for the rate of SN detection. Nevertheless, the potential of event-by-event detection of SN neutrinos in IceCube-Gen2 with mDOMs has been shown, with almost 100% of probability for detecting heavy SNe within 800 kpc from Earth using the best trigger condition.

In order to reach higher rate of SN detection, e.g. one per year, it would be necessary to detect a SN at 4.4 Mpc with 50% of probability for the curve of the best trigger condition. To reach those values, the detection of ten times more events than the results obtained here would be necessary. The construction of PINGU would help to reach higher SN rate detection because of the possibility of implementing new trigger conditions between different modules, and because its modules would likely have PMTs with higher QE. However, a SN detection rate of one per year does not seem reachable, either with a larger number of modules, since it would be necessary to deploy ten times more of them. The use of better components in the mDOM, like PMTs with higher quantum efficiency, could lead to improve the SN detection rate. An hypothetical new design for the mDOM with 48 instead of 24 PMTs, maintaining the same effective area, would provide about one SN detection per year in IceCube-Gen2, assuming that the number of events detected in 2 PMTs in this simulation can be extrapolate into 4 PMTs in a module with the double number of them. A deeper study about the trigger requirement could also improve the identification of SN neutrinos with less statistics. This could be, for instance, to require

geometrical correlation between the hits, as the MeV events usually hit PMTs over the same region of the mDOM. This would be translated into a smaller impact of the dark noise, which could lead to apply trigger conditions of fewer events or fewer hit PMTs, increasing the SN detection rate.

Table 7.6: Expected number of supernova detections within one decade of IceCube-Gen2 operation equipped mDOMs for different trigger conditions. The first, second and third columns determine the trigger condition. The fourth and fifth columns display the expected number of SN detection in 10 years, obtained from the cosmic formation rate (SFR) and from the observed SN rate and blue luminosity (SNR + $L_{\odot}^{B}$) depicted in 7.7. The last row shows the expected number of false SN detection, according with the rate of false SN detection obtained from 7.6.

Min. PMTs hit (n_{coin})	Δt_{coin} (ns)	Number of events (N_{ν})	Detected SN (in 10 years)		False SN detected (in 10 years)
			Scaled to cosmic SFR	Prediction from SNR + $L_{\odot}^{B}$	
3	0.85	5	1.83	0.92	7.2
	1.2	6	1.80	0.90	7.4
4	10	3	1.88	0.94	1.5×10^{-3}
		4	1.76	0.88	2.3×10^{-7}
		5	1.71	0.85	2.6×10^{-11}
5	10	3	1.61	0.81	1.23×10^{-13}
		4	1.45	0.72	$<1 \times 10^{-15}$
		5	1.30	0.65	

7.3 Effects of the generation volume on the results

In this chapter, the same ice properties for all mDOMs were assumed, which has been chosen as the ones of the clean ice at 2278 meters depth. In a real case, the mDOMs in IceCube-Gen2 will not be deployed at the same depth, therefore each module would be surrounded by ice with different properties, as it was shown in Fig. 4.2. This, together with the limited size of the generation volume, have had an impact over the results obtained here.

The simulated volume has been chosen as a cylinder of 20 meters height and radius. In chapter 5, it was shown that the effective volume can be approximated by a sphere with radius of about 9.3 m, which fits inside the simulated cylinder volume. Nevertheless, this does not mean that there are no losses with respect to a real detection, where an event generated outside this cylinder can still be detected. Fig. 5.1 shows that the effective volume increases with the radius of the generation volume until $R_{\text{gun}} \sim 220\,\text{m}$. This means that the number of detected events is being underestimated, since events produced outside the generation volume can still be detected. This can be directly observed in Fig. 7.12, where the distance at which the detected events have been generated are depicted. The

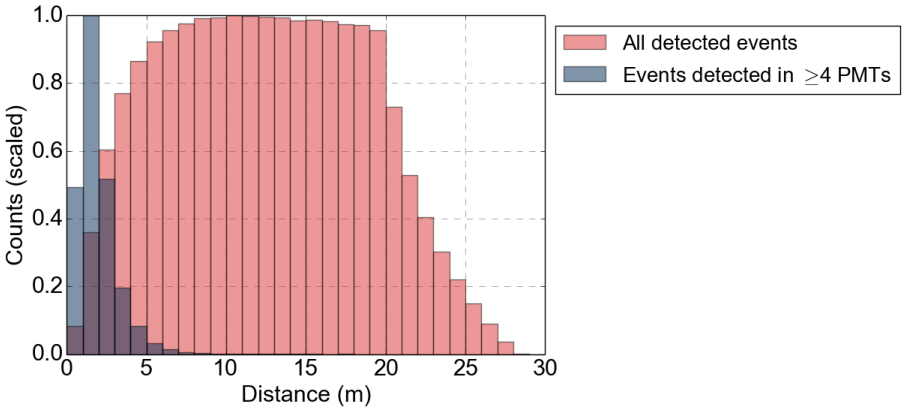

Figure 7.12: Detected events and events which have been detected in at least 4 different PMTs per distance from the mDOM, according of the simulation where the events have been generated in a cylinder of 20 meters height and radius with the mDOM in its center. The histograms have been scaled to one for better comparison.

results clearly show that events produced further than the size of the cylinder would still be detected, since a "cut" appears in the histogram at about 20 meters, length of height and radius of the cylinder. For events which produce signal in 4 or more PMTs, it can be seen that the generation volume cover well the whole sensitive volume, therefore those events are not being lost by the limited size of the simulation. Notice that, even if closer events are more likely to be detected, the number of generated events rises up with r^2, where r is the distance from the mDOM to the event, since they have been generated randomly in the whole volume, reason because the maximum of the histogram does not appear at the lowest distance value.

On the other hand, mDOMs placed in dirtier ice would detect less events because of the higher absorption of photons. The effective volume can also be used to scale the amount of detected events with the ice properties, since it depends directly on the ratio of detected to generated events and it changes linearly with the absorption length of the ice, as it was shown in Fig. 5.3. Nevertheless, to scale the results, it would have been necessary that the generation volume has lengths of about 220 meters, where the effective volume has already a constant value and does not depend on the size of the generation volume anymore. From Fig. 4.2 right, it can be obtained that the mean absorption length in the region of short photon's wavelength – the important region in regards to the typical QE curves and Cherenkov emission – is usually above 20 meters. Therefore, even if placing the module in dirtier ice would cause less detection, this should not modify significantly the results because of the small path of the photons inside generation volume. The simulation in clean ice has also lead to a better directionality of the SN than in a real case.

In conclusion, the losses in the number of detected events because of the small generated volume seems to be higher than the gains from simulating the clean part of the South Pole ice, which results in a underestimation of the results. This might explain some discrepancies in the results obtained in this work. While in chapter 5 it was obtained that the effective volume per module would be about 2.6 times bigger when using mDOMs over current DOMs, the number of detected events per mDOM obtained in this chapter

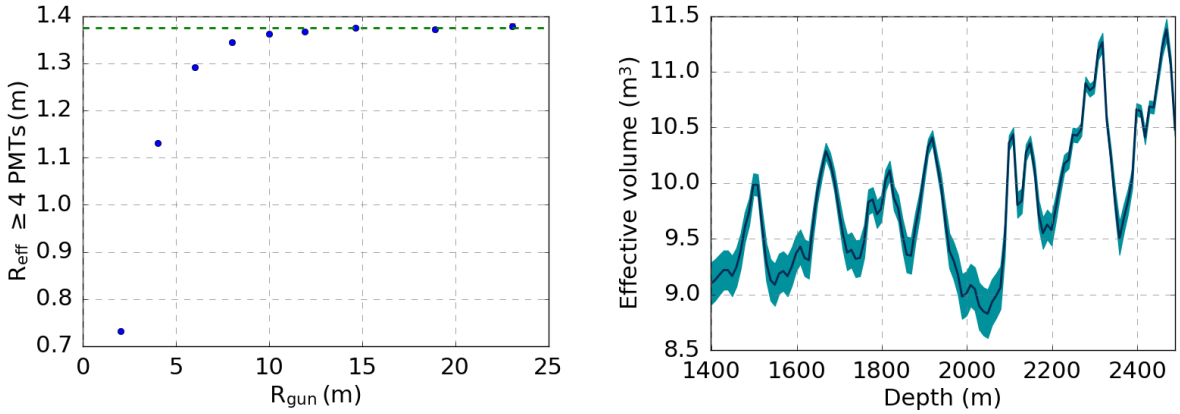

Figure 7.13: Left: Value of the radius for the effective volume of 4 or more hit PMTs at 2278.2 meters depth. **Right:** Result for the effective volume of 4 or more hit PMTs as a function of the depth. Shaded region stands for the uncertainty region. Both pictures have been calculated from charged particles of 25 MeV.

was only about 2.0 bigger than the expected with DOMs, in comparison with the results obtained in [7] (a factor 2.1 if all interactions would have been included in this work). Nevertheless, deeper studies would be necessary to claim that this is the reason of the discrepancy in the results[1]. In order to do an accurate simulation of one single module and scale the results to a whole IceCube-Gen2, it would be necessary:

- A generation volume big enough to assure that the effective volume is constant, where no events are being lost because of the limited size of the simulation.
- To scale the results, not only with the number of modules in IceCube-Gen2, but also with the ratio between the effective volume at the depth where the simulation was made with respect to the average effective volume in IceCube-Gen2.

Nevertheless, the computational time of the simulation increases dramatically with the size of the generation volume. Also, it would have been necessary to generate many more events to get similar statistics, which would have also increased the computational time. These reasons made necessary the assumptions taken in this work.

The situation changes when considering events which meet the trigger conditions defined before. The results of best case scenario, which was 4 or more different hit PMTs, can indeed be extrapolated with its effective volume, since it reaches its constant value inside the generation volume used in this chapter, as displayed in Fig. 7.13 left. That can also be obtained from Fig. 7.12, which shows that all events detected in 4 or more PMTs are generated in the first 10 meters. The effective volume of Fig. 7.13 left was obtained using charged particles with 25 MeV, which is very close to the mean energy of the events

[1] In [7] it is not specified which SN model and oscillation hierarchy are considered to obtain the results, therefore the scenario used here may differ from [7], which might also explain the differences between the results.

that meet the trigger condition, which was obtained to be $25.5 \pm 0.2\,\mathrm{MeV}$. This allows to determine the effective volume for these triggered events at different absorption lengths and compute its value for different depths, which is shown in Fig. 7.13 right. The effective volume for the trigger condition of $n_{\mathrm{coin}} = 4$ is $V_{\mathrm{eff}} = 10.86 \pm 0.06\,\mathrm{m}^3$ at the depth where the simulation has been done, while the average one for this condition is $\overline{V}_{\mathrm{eff}} = 9.81 \pm 0.02\,\mathrm{m}^3$. Therefore, it can be estimated that the detected events which meet this triggered condition would have been about $(90.2 \pm 0.6)\%$ of the presented in table 7.1 if a simulation of each mDOM with its corresponding ice properties would have been done, which results in 4.75 ± 0.05 detected events in 4 or more PMTs.

In table 7.7, the number of events which meet the best trigger condition from section 7.2 has been estimated to the expected value for different scenarios, and the estimations have been used to calculate the detection probability and SN detection rate. Each calculation has been done for the heavy and light SNe fluxes. The number of events in each case have been obtained by assuming the same energy distribution, and using the ratio of detected events to scale the result for each scenario, according with the value obtained in tables 7.1 and 7.2. This is a very rough estimate, since the energy spectra not only affect the detected events but also the probability that the events meet the trigger condition. Nevertheless, the results of table 7.7 provide an overview of the losses or gains due to the assumptions that have been done in this chapter. Simulations with the correct fluxes and energy spectra for each considered scenario need to be performed in order to get reliable values.

Table 7.7: Results for the best trigger condition of detecting $N_\nu = 3$ events within $\Delta t = 10\,\mathrm{s}$ where each of them has produced signal in at least $n_{\mathrm{coin}} = 4$ PMTs within $\Delta t_{\mathrm{coin}} = 10\,\mathrm{ns}$, from the simulation and estimated to different scenarios. The first number stands for the estimation using the results of the heavy SN (table 7.1), while the number in parenthesis stands for the estimation using the results of the light SN (table 7.2). The first column shows the number of triggered events of each scenario of a SN at 10 kpc. Second column shows the distance at which the probability of SN detection is at 50%, calculated from Eq. 7.7. Third and fourth column display the expected number of SN detection in 10 years, obtained from the cosmic formation rate (SFR) and from the observed SN rate and blue luminosity (SNR + $L^B_\odot$), depicted in Fig. 7.7. The rows display the different scenarios. The first row shows the result obtained in section 7.1.3 for the events that meet the trigger condition. Second and third row displays the expectation for two different oscillation scenarios, according to the results of [1]. Fourth row shows the expected values when adding interactions not included in the simulation (see section 2.2.3), scaled from the results of [25]. Last row shows the results scaled by the average effective volume of the trigger condition, obtained from Fig. 7.13 right.

	Triggered events ($\times 10^4$)	50% detection probability (kpc)	Detected SN (in 10 years)	
			SFR	SNR + $L^B_\odot$
Results	5.24 (2.08)	1400 (881)	1.88 (1.50)	0.94 (0.75)
Normal hierarchy	5.9 (2.3)	1490 (940)	1.9 (1.6)	1.0 (0.8)
Inversed hierarchy	7.3 (2.9)	1660 (1040)	2.0 (1.7)	1.0 (0.8)
All interactions	5.6 (2.2)	1450 (910)	1.9 (1.5)	1.0 (0.8)
Scaled to $\overline{V}_{\mathrm{eff}}$	4.75 (1.88)	1334 (839)	1.84 (1.45)	0.92 (0.72)

8 Summary and outlook

In this work, the sensitivity of multi-PMT digital optical modules deployed in South Pole ice for SN neutrinos has been studied, motivated by the potential of mDOMs to detect MeV neutrinos. The study of SN neutrinos can reveal a detailed picture of the events that accompany the collapse of the core, and shed some light on the not-yet well understood development of a core-collapse supernova. The study of SN neutrinos could also help to clarify some properties of these particles, as e.g. the neutrino mass hierarchy. Different models of a 10 kpc core-collapse SN were described and used in this work, where only the inverse beta decay and the electron neutrino - electron elastic scattering, most important SN neutrino interactions in ice, have been included in the simulations.

The mDOM is one of the proposals of new optical modules that is being development for the next generation of IceCube neutrino observatory, IceCube-Gen2. The use of several photomultipliers per module can enable local coincidences and information on the arrival direction of detected photons. In order to study the sensitivity of the mDOM for the detection of SN burst neutrinos, a simulation written in Geant4 was used. The simulation includes the physical properties of the mDOM and of the South Pole ice, and generates the events according to the chosen core-collapse SN burst model. Directly from the simulation the total energy spectra of a burst of SN neutrinos and antineutrinos were obtained, which show that antineutrinos have higher energies than neutrinos, as well as their produced particles after their interactions, making them easier to be detected.

The effective volume of the mDOM for SN neutrino detection was obtained using the simulation. The results were scaled to a whole IceCube-Gen2 detector with mDOMs and compared to the current effective volume of IceCube. An increase of a factor $\sim$2.6 for mDOMs with respect to nominal DOMs is observed, while IceCube-Gen2 with mDOMs would have an about 7 times bigger effective volume than current IceCube for the detection of SN neutrinos. IceCube and IceCube-Gen2 together would provide about 28 Mton of effective mass of South Pole ice for the detection of SN neutrinos. It was shown that MeV events in the mDOM can produce local coincidences when they have been produced close enough to the mDOM, while global coincidences between different modules in IceCube-Gen2 are very unlikely. This allows to treat each mDOM as an individual detector to study low-energetic neutrinos from SN burst.

The reconstruction of single SN neutrino interactions is not straightforward, since the particles produced by SN neutrino interactions in ice would travel only about 10 centimeters. Another problem with the reconstruction is the absence of timing information, since photons from the same event would likely arrive on the mDOM below the time resolution of the PMTs. Two different methods of reconstruction by using one single mDOM were studied. In the first case, the most simple method based in a direct reconstruction of the hit PMTs was analysed. The results shown an indeterminacy in the direction reconstruction produced by the uncertainty in the direction of the photons emitted by Cherenkov effect. Nevertheless, this simple method can be used to get a vector which points to the position of the events with an accuracy of about 20^o. A second method of single event reconstruction based in the minimization of a likelihood function was studied, which shows

that, with the combination of the previous method, the likelihood space can be reduced from 6 to 2 dimensions, i.e. the direction of the particle. It shows that two events with different directions can produce a similar signal at the module due to scatters of the charged particle. This method can not obtain the direction of MeV neutrinos as a global minimum but a ring-like minimum due to the shape of photon emission. Other methods could be studied in order to improve the reconstruction, as it could be the use of photon propagation probability tables; which instead of running a simulation for each reconstruction, it uses these photontables calculated once to minimize a likelihood function.

Last, but not least, the detection of a core-collapse supernovae burst by an IceCube-Gen2 detector consisting of $\sim$ 15000 mDOMs was studied. About 6.4 million neutrinos coming from a SN with a progenitor mass of 27 solar masses at a distance of 10 kpc would produce a signal in the detector, where 7.5% would produce coincident hits on mDOM. A lighter SN with progenitor mass of 9.6 solar masses at 10 kpc lead to the detection of 2.8 million events. It was also shown that these numbers might be underestimated due to the limited size of the generation volume in the simulation. Therefore, to obtain more reliable results, bigger volumes should be simulated. To detect extra-galactic SN neutrinos, trigger conditions were defined in order to distinguish individual SN neutrinos from background signals. From the best trigger condition, determined by studying the probability of false detection due to uncorrelated background signals, a heavy SN at a distance of $\sim$1.4 Mpc would be detected with a probability of 50%. Neutrinos coming from this distance would have travelled about 4.4 million years on their path to us. External background sources like The Sun or the atmospheric neutrinos were not considered here. In this case IceCube-Gen2 with mDOMs would provide the detection of almost 1 or 2 SN per decade, depending on the model of SN formation rate which is considered. These values depend on the SN mass, where dark SNe were not considered, which are though to cover about 10% of the total number of SN explosion and whose neutrino spectra is more energetic, being detected at a higher efficiency. The results show that light SNe would be detected at $\sim$0.9 Mpc with a probability of 50%.

This work presents the very first study concerning the detection efficiency of mDOMs deployed in South Pole ice for the detection of MeV neutrinos coming from supernovae, therefore there is still a long and exciting way forward to study all the possibilities of the module for such low energetic neutrinos. First, the simulation must be completed with all the possible interactions of SN neutrinos in ice, since here only the most important ones were included. More complex methods for direction reconstruction of low energetic events should be studied in order to cover the possibilities of reconstruction with one single module. Also the possibilities of combining more than one single module could allow to combine local coincidences in the same module with coincidences in different ones, which would improve significantly the reconstruction possibilities. The detection of low energetic events in more than one single mDOM might be an interesting study if PINGU is eventually built. Several models and assumptions were necessary in order to get the detection yield of SN neutrinos in IceCube-Gen2 with mDOMs, hence the results exposed here should not be considered as absolute results but indeed as a starting point for a deeper exploration, where different core-collapse supernova models, oscillation scenarios and ice properties should be considered. Several modifications of the mDOM are still under study, like PMTs with bigger photocathode area or with higher QE in the short wavelength region, which would affect the sensitivity of the modules for MeV

neutrinos. Last, suppression of correlated background sources like the Sun or atmospheric neutrinos needs to be study if extra-galactic SN neutrinos are to be detected. The solar neutrinos are in the MeV range but they are slightly less energetic than SN neutrinos, which decreases their possibility to meet triggered conditions like e.g. several hit PMTs. The direction of them is well conserved in their interactions, since only neutrinos and no antineutrinos are emitted, therefore their suppression via directionality might be the best way to distinguish them from SN sources. Atmospheric neutrinos have energies much higher than SN neutrinos, but their interactions can undergo producing MeV charged particles which can also be confused with SN neutrino signals, therefore their suppression is also relevant.

IceCube-Gen2 equipped with mDOMs will not only extend its sensitivity to higher energetic neutrinos but also to lower ones, without the need of a higher density of modules, providing the world biggest detector for neutrino detection in a much wider range of energies. The results obtained in this work are a high motivation to go forward with the study of the possibilities of the mDOM for detection and identification of low energetic neutrinos.

9 Bibliography

[1] K. Abe *et al.* (Hyper-Kamiokande), (2011), arXiv:1109.3262 [hep-ex] .

[2] A. Mirizzi *et al.*, ArXiv e-prints (2016), arXiv:1508.00785 [astro-ph.HE] .

[3] K. Hirata *et al.*, Physical Review Letters **58**, 1490 (1987).

[4] D. Schramm, Physics Reports **189**, 89 (1990).

[5] J. Beringer *et al.* (Particle Data Group), Phys. Rev. **D86**, 010001 (2012).

[6] D. O. Caldwell and R. N. Mohapatra, Phys. Rev. **D48**, 3259 (1993).

[7] F. Halzen and S. R. Klein, Rev. Sci. Instrum. **81**, 081101 (2010), arXiv:1007.1247 [astro-ph.HE] .

[8] M. G. Aartsen *et al.* (IceCube), Phys. Rev. Lett. **113**, 101101 (2014), arXiv:1405.5303 [astro-ph.HE] .

[9] M. G. Aartsen *et al.* (IceCube), (2014), arXiv:1412.5106 [astro-ph.HE] .

[10] IceCube collaboration, *Neutrino astronomy with IceCube and beyond*, Internal documents (2016).

[11] A. Kappes, EPJ Web of Conferences **116**, 01001 (2016).

[12] R. Abbasi *et al.* (IceCube), Astron. Astrophys. **535**, A109 (2011), [Erratum: Astron. Astrophys.563,C1(2014)], arXiv:1108.0171 [astro-ph.HE] .

[13] M. Herant, S. A. Colgate, W. Benz, and C. Fryer, Los Alamos Sci. **25**, 164 (1997).

[14] H. A. Bethe, Reviews of Modern Physics **62**, 801 (1990).

[15] C. Chiosi, Geneva Observatory, CH-1290 Sauverny, Switzerland , p.199 (1986).

[16] M. P. Fewell, Am. J. Phys. **63**, 653 (1995).

[17] R. A. S. Emeritus and J. John W. Jewett, *Physics for Scientists and Engineers with Modern Physics*, 9th ed. (Physical Sciences: Mary Finch, 2005) Chap. 44.5.

[18] A. Heger, S. E. Woosley, C. L. Fryer, and N. Langer, in *ESO ASTROPHYSICS SYMPOSIA* (Springer Science+Business Media, 2002) pp. 3–12.

[19] J. M. Lattimer, M. Prakash, C. J. Pethick, and P. Haensel, Phys. Rev. Lett. **66**, 2701 (1991).

[20] P. G. Giannaka and T. S. Kosmas, Adv. High Energy Phys. **2015**, 398796 (2015), arXiv:1502.07225 [nucl-th] .

[21] H. Suzuki, *Physics and Astrophysics of Neutrinos* (Springer, 2014) Chap. Supernova Neutrinos.

[22] H.-T. Janka, K. Langanke, A. Marek, G. Martinez-Pinedo, and B. Mueller, Phys. Rept. **442**, 38 (2007), arXiv:astro-ph/0612072 [astro-ph] .

[23] F. Hanke, B. Mueller, A. Wongwathanarat, A. Marek, and H.-T. Janka, Astrophys. J. **770**, 66 (2013), arXiv:1303.6269 [astro-ph.SR] .

[24] P. Vogel and J. F. Beacom, Phys. Rev. **D60**, 053003 (1999), arXiv:hep-ph/9903554 [hep-ph] .

[25] S. Böser, M. Kowalski, L. Schulte, N. L. Strotjohann, and M. Voge, Astropart. Phys. **62**, 54 (2015), arXiv:1304.2553 [astro-ph.IM] .

[26] T. Totani, K. Sato, H. E. Dalhed, and J. R. Wilson, Astrophys. J. **496**, 216 (1998), arXiv:astro-ph/9710203 [astro-ph] .

[27] M. Buchkremer, *Electroweak Interactions: Neutral currents in neutrino-lepton elastic scattering experiments* (Université Catholique de Louvain / CP^3, 2011).

[28] C. Giunti and C. W. Kim, *Fundamentals of Neutrino Physics and Astrophysics* (Oxford University Press, 2007).

[29] T. Sukhbold, T. Ertl, S. E. Woosley, J. M. Brown, and H. T. Janka, Astrophys. J. **821**, 38 (2016), arXiv:1510.04643 [astro-ph.HE] .

[30] J. M. Lattimer and F. D. Swesty, Nucl. Phys. **A535**, 331 (1991).

[31] A. W. Steiner, M. Hempel, and T. Fischer, The Astrophysical Journal **774**, 17 (2013).

[32] R. E. Brandt and S. G. Warren, Journal of Glaciology **43**, 339 (1997).

[33] M. J. Rubin, *Studies in Antarctic Meteorology (Antarctic Research Series)* (American Geophysical Union, 1991).

[34] I. Tamborra, B. Muller, L. Hudepohl, H.-T. Janka, and G. Raffelt, Phys. Rev. **D86**, 125031 (2012), arXiv:1211.3920 [astro-ph.SR] .

[35] M. T. Keil, G. G. Raffelt, and H.-T. Janka, Astrophys. J. **590**, 971 (2003), arXiv:astro-ph/0208035 [astro-ph] .

[36] A. A. Watson, *100 years of cosmic ray physics: From pioneering experiments to physics in space. Proceedings, International Seminar, CRIS 2010, Catania, Italy, September 13-17, 2010*, Nucl. Phys. Proc. Suppl. **212-213**, 13 (2011), arXiv:1101.4535 [physics.hist-ph] .

[37] J. Jelley, *Cerenkov Radiation And Its Applications* (London: Pergamon Press, 1958).

[38] L. Classen, *Prototyping a multi-PMT optical module for the IceCube-Gen2 neutrino telescope*, PhD thesis (in preparation).

[39] J. Ahrens *et al.*, "IceCube Preliminaty Design Document," (2001), `https://icecube.wisc.edu/icecube/static/reports/IceCubeDesignDoc.pdf`; visited on December 28th 2015.

[40] E. Andres *et al.*, Astropart. Phys. **13**, 1 (2000), arXiv:astro-ph/9906203 [astro-ph] .

[41] J. Ahrens *et al.* (IceCube), *Neutrino physics and astrophysics. Proceedings, 20th International Conference, Neutrino 2002, Munich, Germany, May 25-30, 2002*, Nucl. Phys. Proc. Suppl. **118**, 388 (2003), arXiv:astro-ph/0209556 [astro-ph] .

[42] R. Abbasi *et al.* (IceCube), Nucl. Instrum. Meth. **A601**, 294 (2009), arXiv:0810.4930 [physics.ins-det] .

[43] IceCube collaboration, `https://gallery.icecube.wisc.edu/internal/` (2016), accessed: 27-11-2016.

[44] R. Abbasi *et al.*, Astroparticle Physics **35**, 615 (2012).

[45] M. G. Aartsen *et al.* (IceCube PINGU), (2014), arXiv:1401.2046 [physics.ins-det] .

[46] M. G. Aartsen *et al.* (IceCube), (2016), arXiv:1607.02671 [hep-ex] .

[47] S. Adrian-Martinez *et al.* (KM3Net), J. Phys. **G43**, 084001 (2016), arXiv:1601.07459 [astro-ph.IM] .

[48] S. Agostinelli *et al.* (GEANT4), Nucl. Instrum. Meth. **A506**, 250 (2003).

[49] Geant4 website, `https://geant4.web.cern.ch/geant4/` (2016), accessed: 13-10-2016.

[50] Björn Herold, PhD thesis (in preparation).

[51] GEANT 4 physics reference manual, `http://geant4.web.cern.ch/geant4/UserDocumentation/UsersGuides/ForApplicationDeveloper/fo/BookForAppliDev.pdf` (2016), accessed: 13-10-2016.

[52] M. Ackermann *et al.*, J. Geophys. Res. Atmos. **111**, D13203 (2006).

[53] G. Mie, Ann. Phys. **330**, 377 (1908).

[54] M. G. Aartsen *et al.* (IceCube), Nucl. Instrum. Meth. **A711**, 73 (2013), arXiv:1301.5361 [astro-ph.IM] .

[55] K. Woschnagg and P. B. Price, Appl. Opt. **40**, 2496 (2001).

[56] L. C. Henyey and J. L. Greenstein, The Astrophysical Journal **93**, 70 (1941).

[57] F. Halzen, J. E. Jacobsen, and E. Zas, Phys. Rev. **D53**, 7359 (1996), arXiv:astro-ph/9512080 [astro-ph] .

[58] F. Halzen and G. G. Raffelt, Phys. Rev. **D80**, 087301 (2009), arXiv:0908.2317 [astro-ph.HE] .

[59] R. Davis, D. S. Harmer, and K. C. Hoffman, Phys. Rev. Lett. **20**, 1205 (1968).

[60] J. N. Bahcall, E. Lisi, D. E. Alburger, L. De Braeckeleer, S. J. Freedman, and J. Napolitano, Phys. Rev. **C54**, 411 (1996), arXiv:nucl-th/9601044 [nucl-th] .

[61] R. J. Barlow, *Statistics: A Guide to the Use of Statistical Methods in the Physical Sciences (Manchester Physics Series)* (Wiley, 1989).

[62] F. James and M. Roos, Comput. Phys. Commun. **10**, 343 (1975).

[63] F. James and M. Winkler, Comput. Phys. Commun. **10** (2004).

[64] J. A. Nelder and R. Mead, The Computer Journal **7**, 308 (1965).

[65] S. Ando, J. F. Beacom, and H. Yuksel, Phys. Rev. Lett. **95**, 171101 (2005), arXiv:astro-ph/0503321 [astro-ph] .

[66] M. D. Kistler, H. Yuksel, S. Ando, J. F. Beacom, and Y. Suzuki, Phys. Rev. **D83**, 123008 (2011), arXiv:0810.1959 [astro-ph] .

[67] F. Matteucci, *The Chemical Evolution of the Galaxy (Astrophysics and Space Science Library)* (Springer, 2001).

[68] E. Cappellaro, R. Evans, and M. Turatto, Astron. Astrophys. **351**, 459 (1999), arXiv:astro-ph/9904225 [astro-ph] .

[69] S. Horiuchi, J. F. Beacom, C. S. Kochanek, J. L. Prieto, K. Z. Stanek, and T. A. Thompson, Astrophys. J. **738**, 154 (2011), arXiv:1102.1977 [astro-ph.CO] .

[70] M. Unland, master thesis (in preparation).

[71] C. Kopper, (2016), private communication.

[72] K. Helbing *et al.*, Light emission in Amanda pressure spheres, Amanda Internal Report (2003).

List of Figures

List of Tables

Acknowledgments

First and foremost, I would like to thank to my main supervisor in this thesis, Prof. Dr. Alexander Kappes, for his valuable guidance and advice, and whose passion for physics has greatly inspired me while working in my project. His patient and help have contributed tremendously to my learning, and I will always feel grateful to have been accepted in his group. I would also like to thank to my second supervisor, Prof. Dr. José Manuel Quesada Molina, who has kindly offered me his support and advices throughout these months, with the added difficulty of the distance. Special thanks to Lew Classen, who has taught me how to work, bringing me his help, guidance and support on my way of this thesis. I feel very grateful for the awesome atmosphere in this working group, where each member has made me feel home since the very first moment I arrived.

I am also immensely grateful to Daniel Guderian, Alejando Jurado, Florian Trittmaack and Martin Unland for their useful comments on earlier versions of the manuscript, although any errors are my own and should not tarnish the reputations of these esteemed persons.

I do not forget the persons who work to make possible this double master program, which brings the opportunity to me and other students to live this valuable and full of learning experience. Special mentions to Prof. Dr. Juan Antonio Caballero Carretero, Prof. Dr. Helmut Kohl and Prof. Dr. José Miguel Arias Carrasco, who have used their precious time to help me in myriad occasions with the administration complications I have found on the way.

Last but not least, I would like to thank to my loved ones for their understandings and supports throughout my entire studies. I will be grateful forever for your love.

Declaration of Academic Integrity

I hereby confirm that this thesis on "Studies on the sensitivity of multi-PMT optical modules to supernova neutrinos in the South Pole ice" is solely my own work and that I have used no sources or aids other than the ones stated. All passages in my thesis for which other sources, including electronic media, have been used, be it direct quotes or content references, have been acknowledged as such and the sources cited.

Cristian Jesús Lozano Mariscal

Münster, January 2017

I agree to have my thesis checked in order to rule out potential similarities with other works and to have my thesis stored in a database for this purpose.

Cristian Jesús Lozano Mariscal

Münster, January 2017